PIONEERING MRI-GUIDED FOCUSED ULTRASOUND PLATFORMS FOR THE TREATMENT OF CEREBRAL CAVERNOUS MALFORMATION

A

Dissertation

Presented to

the faculty of the School of Engineering and Applied Science

University of Virginia

---

in partial fulfillment

of the requirements for the degree

Doctor of Philosophy

by

Delaney G. Fisher

May 2024

APPROVAL SHEET

This

Dissertation

is submitted in partial fulfillment of the requirements
for the degree of

Doctor of Philosophy

Author: Delaney G. Fisher

This Dissertation has been read and approved by the examing committee:

Advisor: Richard Price

Advisor:

Committee Member: Brian Helmke

Committee Member: Petr Tvrdik

Committee Member: G. Wilson Miller

Committee Member: Tajie Harris

Committee Member:

Committee Member:

Accepted for the School of Engineering and Applied Science:

Jennifer L. West, School of Engineering and Applied Science

May 2024

Acknowledgements

Embarking on this academic journey has been a transformative experience, and I am immensely grateful to all those whose support and guidance have played a pivotal role in shaping this dissertation. I must first thank my advisor, Dr. Richard Price. My graduate experience would truly have not been the same without your continued encouragement, mentorship, and advocacy. Your commitment to putting your students first and empowering us to strive beyond our scientific and professional comfort zones has been the greatest gift. I must next thank Dr. Ji Song, our invaluable lab manager. You have immensely eased the life of every Price Lab student, more than we could ever know, and I am very grateful for this ignorance. To you both, I cannot thank you enough for always ensuring that I have had the resources to pursue my scientific endeavors and for always chatting with me about lab and life updates.

I am grateful to my committee members and collaborators for their continued guidance and feedback. Thank you to Dr. Brian Helmke for serving as my chair, sharing critical scientific insights, and providing a wonderful TA experience for Biotransport. I would like to thank Drs. Petr Tvrdik and Wilson Miller not only for their roles as mentors but also their roles as collaborators. Without their crucial CCM and MRI contributions, this dissertation would not have been possible. I'm incredibly grateful to Dr. Tajie Harris for sharing her extensive neuroimmunology knowledge both during committee meetings and in one of my favorite classes at UVA. I must also share my gratitude to Dr. Khadijeh Sharifi. Her dedicated efforts enabled the experiments in this dissertation.

Next, I must express my appreciation for my colleagues/friends in the Price Lab. So many of my graduate experiments would have not been possible without your moral and physical support. To Katie Gorick, you are synonymous with Price Lab to me (to which I know you will say "I am very old"), but I truly cannot picture what my graduate journey would have been without you in it. Thank you for always injecting humor into my day, sharing your scientific wisdom, asking if bugs feel pain, and supplanting Jeremy Gatesman as the top tail vein sniper. To Andrew Thim, I must thank you for always being willing to explain FUS physics, write a MATLAB script, or help decontaminate an incubator, and in every scenario, knowing what's garbage. To Alex Mathew, thank you for "threatening" the lab culture with me and appreciating the complexity of my Higher Grounds coffee decision for each day. To Tor Breza, thank you for making so many of our scientific illustrations, being willing to kind of learn MRI physics with me, not acting on your intrusive thoughts, and always being down for a cafeteria run. To shark boy and lava girl, that is

Mark Schwartz and Anna Debski, thank you for entertaining the lab with your sibling-like banter. Mark, thank you for showcasing fashionable outfits, healthy communication, and scarily impressive abilities to find people on the internet. Anna, thank you for taking on the nanoparticle project, carrying it farther than Katie or I ever did, for consistently contributing to keeping the lab clean, and for always sharing your conniptions with us. To Kathy Nowak, Lydia Petricca Kitelinger, and Josh Samuels, thank you for sharing your BIMS insights in a sea of BME perspectives. You have greatly deepened our immunology and neuroscience proficiency, especially for flow and IF staining. To big and little Matt (Dewitt and Hoch, respectively), thanks for making Snyder days more tolerable, collaborating in science and soccer, and, to little Matt specifically, may you never stop aiming to “change the face of medicine” or drink infinite amounts of bubbly water. To Nareen Anwar and Tanya Cruz, thank you for teaching me the language of the youth, filling the JV office with laughter, and, to Tanya specifically, carrying forward our lab’s work on CCM. I am so grateful for the positive, collaborative environment that every Price Lab student has helped to cultivate and maintain.

I also want to thank the undergraduate students that I have worked with. To Annie Ford, Zoe Garman, Rebecca Della Croce, Daniel Carrier, Alex Rashid, and Ishaan Shah, I appreciate the opportunity that you all gave me to serve as your scientific and career mentors. It has been a pleasure to see your efforts and growth in advancing our understanding of related research questions, and I wish you all the best in your various medical and scientific pursuits.

Finally, I must extend my gratitude to my friends and family. To those in my graduate cohort, thank you for providing an initial friendship and support group that only grew stronger throughout our journey together. To my many friends across the BME graduate department, especially Taylor Marohl, Mackenzie Grubb, Ridhi Sahani, and Mukti Chowkwale, thank you for all your support through various graduate, professional, and life milestones. Thank you to my parents and brother for trying to understand what I do and why for most of this time I did not know when I would graduate. Thank you to my biggest supporter and fiancé, Justin, for keeping me fed, sane, and happy throughout this PhD experience. I am incredibly fortunate to be surrounded by such an encouraging and compassionate group of people. Thanks to you all for making this journey possible.

TABLE OF CONTENTS

CHAPTER 1: PREFACE

1.1 ABSTRACT

Cerebral cavernous malformations (CCMs) are hemorrhagic vascular lesions that arise in the central nervous system and affect approximately 0.5% of the general population. CCMs form as a result of endothelial cell bi-allelic mutation in one of 3 genes—*KRIT1*, *CCM2*, or *PDCD10*—that encode components of the "CCM complex"[1]. Disruption of this protein complex alters signaling in several pathways leading to endothelial junctional permeability and increased proliferation which contribute to the dilated, multi-cavern morphology of these lesions. Patients with CCMs often experience neurological symptoms (i.e. severe headaches, vision impairments, and seizures) that progressively worsen over time due to recurrent hemorrhage. As the most common treatment option for CCM is surgical removal—which presents high risk to the patient—new approaches are urgently needed.

This lack of treatment options for CCM motivates the goal of this dissertation: to develop non-invasive therapeutic platforms for the treatment of CCM using magnetic resonance (MR)-guided focused ultrasound (FUS). MR-guided FUS is a non-invasive treatment method that leverages pressure waves to oscillate simultaneously-administered, gas-filled microbubbles within brain capillaries[2]. This FUS technique temporarily opens the BBB, allowing ordinarily impenetrable agents across the vessel walls and can stimulate secondary neuroprotective effects[3]. Under MR image guidance, FUS BBB opening (BBBO) enables targeting—localizing these effects to precise diseased brain regions.

In the first aim of this dissertation, we use the information that is known about the clinical CCM pathology and how CCM is monitored in patients to inform the development and assessment of pre-clinical models of the disease. Specifically, we optimize several clinically-adapted MR sequences and employ these sequences longitudinally to understand the lesion progression in a

chronic mouse model of CCM. Further, using immunofluorescent imaging, we correlate cellular level responses to the MR signatures of CCM instability. Leveraging our optimized MR sequences, we found that CCMs increase in cumulative volume and permeability with age, while individual lesion trajectory varied in our chronic CCM model. Additionally, we demonstrated that CCM permeability was not correlated with CCM volume. However, cell density around CCMs was inversely correlated with CCM permeability. Further, examination of lesion burden in our mouse model revealed that optimal treatment intervention would occur between 2 and 3 months of age to ensure sufficient but not overly encumbered lesion load. Finally, we demonstrated that our MR sequences could detect lesion growth and bleeding associated with CCM exacerbation in our mouse model.

In the second aim of this dissertation, we use this MRI platform to enable the design and evaluation of FUS BBBO for CCM. MR sequences from aim 1 were leveraged to screen, target, and monitor CCMs before, during, and after FUS BBBO of CCMs in our chronic CCM mouse model. In this aim, we evaluate the efficacy, safety, and therapeutic effect of FUS BBBO for CCMs. Further, we explore the effect of single and repeat treatments of FUS BBBO as well as the effect of fixed peak-negative pressures and passive cavitation feedback-controlled peak-negative pressures. We found that FUS can open the BBB and enhance MR contrast agent accumulation within the CCM microenvironment. Importantly, we established that FUS BBBO did not induce growth or bleeding of sonicated CCMs. Astonishingly, our study revealed that FUS BBBO of all tested regimens arrested the growth of sonicated CCMs. Further, we found that repeat BBBO with fixed peak-negative pressures even reduced the formation of new CCMs. This study highlights FUS BBBO as a safe, non-invasive, and independently beneficial treatment for CCM, which may yet be further enhanced by its seamless integration with therapeutic delivery.

In the third aim of this dissertation, we leverage our MRI platform to evaluate the ability of FUS BBBO to augment delivery of MR contrast agents of differing sizes to the CCM

microenvironment. We find that FUS BBBO elevates the delivery rate and the total delivery of a small molecule model drug. FUS BBBO doubled the delivery of this 1 kDa contrast agent in the lesion core and tripled it in the perilesional space. The benefit of FUS BBBO was even more apparent for a small biologic model drug. For this 17 kDa contrast agent, FUS BBBO boosted delivery 22-fold in the lesion core and 3.8 fold in the perilesional space. Finally, we note that FUS BBBO differential enhances the delivery of the contrast agents, increasing small molecule delivery in the perilesional space and a greater enhancement of small biologic delivery in the intralesional space. Combined with our prior demonstration of its independent efficacy in halting CCM growth and formation, these findings highlight the unprecedented potential of FUS BBBO to generate transformative treatment paradigms for CCM.

1.2 Preview of Dissertation

In Chapter 2 of this dissertation, we will introduce relevant background material for CCM and FUS BBBO as well as the potential for clinical translation of FUS therapies for CCM at UVA. In Chapter 3, we present the development of an MR imaging platform for longitudinal monitoring of CCM progression in a chronic mouse model of the disease. In Chapter 4, we conduct the first investigation of FUS BBBO for CCM and evaluate its ability to open the BBB in the CCM microenvironment, the acute and long-term safety of this approach, and the therapeutic effects of several treatment regimens of FUS BBBO for CCM. In Chapter 5, we inspect the ability of FUS BBBO to enhance delivery of various-sized molecules within the CCM microenvironment. Finally, Chapter 6 considers future research questions generated by the research conducted in this dissertation.

CHAPTER 2: INTRODUCTION

2.1 Cerebral Cavernous Malformation (CCM)

2.1.1 CCM Lesion Formation and Growth

CCMs are hemorrhage-prone lesions of the cerebrovasculature arising from the bi-allelic loss of one of three CCM-related genes: *CCM1/KRIT1*, *CCM2*, or *CCM3/PDCD10*. These mutations can occur sporadically (~80% of cases) or be genetically inherited (i.e. familial case; ~20% of cases). Familial cases, marked by a germ-line CCM mutation, exhibit earlier disease onset and a greater lesion burden than sporadic cases[2]. Still it has been noted that only a small number of mutated endothelial cells are necessary to develop CCMs[3]. This observation led to the discovery that cavernomas appear to develop in a similar manner as some tumors. A mutated cell can undergo endothelial-to-mesenchymal transition allowing it to initially rapidly proliferate. Then the mutated cell is able to recruit wild-type endothelial cells to further expand the lesion[3,4]. On a molecular level, these mutations disrupt a protein complex known as the CCM complex. This disruption alters signaling of many pathways resulting in increased proliferation and instability of endothelial cellular junctions which can contribute to lesion formation and growth as well as increased lesion permeability and iron deposition, respectively[1]. While pre-clinical trials have explored modifying downstream targets in the impaired CCM complex signaling pathway, their limited success underscores the need for improved therapeutic delivery into cavernomas or identification of more effective therapeutic targets for CCM.

2.1.2 Clinical Need for Non-invasive CCM Therapies

Individuals with cerebral cavernous malformations (CCM) contend with debilitating symptoms, including weakness, numbness, severe headaches, vision changes, and communication difficulties. More severe manifestations can include stroke, seizures, and even paralysis. Symptoms typically arise due to cavernomas that have hemorrhaged. Once a

cavernoma has hemorrhaged, it has an up to 10-fold increase in annual risk for bleeding—leading to worsening symptoms for the patient[5]. The prevailing recourse for treating symptomatic CCMs is open brain surgical removal. However, resection is not feasible for all patients or CCMs, and neurosurgery inherently carries risk due to its invasive nature in vital brain tissue. Indeed, even for very experienced surgical teams, there is still a 5%-18% postoperative morbidity rate associated with resection[2]. Similar to tumor resection, if a cavernoma is not removed with clean margins, CCMs have been seen to regrow in the same location[4,6].

Given the associated risks of traditional surgery, minimally-invasive procedures have been highly coveted for CCM. Presently, only two minimally-invasive therapies have been employed for patients: stereotactic laser ablation and stereotactic radiosurgery[7]. Stereotactic laser ablation uses a laser to heat and coagulate the cavernous tissue, but this procedure is still invasive, requiring craniotomy for laser insertion[8]. Stereotactic radiosurgery delivers focused radiation to damage the DNA of cells within cavernous tissue and does not require opening of the skull. However, this procedure has been greatly controversial in the field. Controversies of radiosurgery include the risk of increased symptoms due to edema following treatment, unclear evidence towards reduction of hemorrhage following treatment, and risk of new lesion formation in patients with familial CCM[7]. Altogether, the severity of CCM symptoms and the limited treatment options underscore the pressing need for intervention strategies with minimal patient risk, emphasizing the imperative development of non-invasive therapies.

2.1.3 Magnetic Resonance (MR) Assessments of CCM

MRI is commonly used to diagnosis and monitor CCM in patients[9,10]. Despite its uniformity in the clinic, MR imaging has been neglected in pre-clinical studies, resulting in a dearth of data on MRI-based CCM lesion progression in mouse models of the disease. MR imaging in clinically-

relevant models of CCM is pivotal for understanding the natural course of the disease in the absence of therapeutic interventions. Further, this data facilitates the estimation of optimal timing for therapeutic interventions. Beyond standard MR scans that detect the presence of cavernomas, specialized MR sequences capable of evaluating lesion permeability and detecting iron deposition from hemosiderin have been developed in patients[11–14]. These sequences aim to predict cavernoma stability in terms of growth and hemorrhage. Adapting these MR sequences for mouse models of CCM would enable the assessment of therapeutic intervention risk (i.e. acute hemorrhage due to therapy). Further, these sequences would permit longitudinal monitoring of therapeutic efficacy in stabilizing the volume and bleeding of treated cavernomas. Given that MRI is integral to CCM diagnosis and patient monitoring, its inclusion in pre-clinical studies is equally imperative for interpreting mechanistic investigations of CCMs within the context of human disease and for designing improved therapeutic interventions.

2.2 Focused Ultrasound (FUS)

2.2.1 FUS-Mediated Blood-Brain Barrier (BBB) Opening

The brain is protected by the BBB which precludes most systemically-administered agents from entering its parenchymal space. This exclusion of therapeutic agents restricts treatment options and has greatly hindered successful therapeutic developments for central nervous system (CNS) diseases. In addition to challenges associated with surpassing the BBB, the treatment of many CNS diseases also requires spatially targeted delivery of therapeutics to avoid deleterious off-target effects. FUS has emerged as a promising treatment method that leverages acoustic energy to oscillate simultaneously-administered microbubbles. This FUS-mediated technique transiently disrupts the BBB, allowing ordinarily impenetrable agents to diffuse and/or convect into

the CNS. Under magnetic resonance image guidance, FUS and microbubbles enable regional targeting—minimizing the large, and potentially toxic, dosage that is often characteristic of systemically-administered therapies. Ongoing clinical trials have shown promising preliminary results, validating the efficacy of this technique in safely opening the BBB[15–18]. FUS also has the benefit of being minimally invasive in comparison to alternative technologies used to treat CNS disorders. Indeed, both convection-enhanced delivery and deep brain stimulation require invasive interventions. While intranasal administration can noninvasively bypass the BBB, it does not have the capacity to selectively target brain regions, is limited by the dosage volume that can be administered, and is difficult to obtain proper alignment in the nasal cavity for effective delivery [19,20]. Chemical agents (e.g. Cereport and Regadenoson) that modulate tight junctions between endothelial cells have also been proposed. However, these drugs do not provide selective BBB opening and have not yet proven to be highly effective in clinical trials [21–23].

2.2.2 FUS BBB Opening Secondary Bioeffects

In addition to facilitating therapeutic delivery to the brain, FUS BBB opening is now known to also provide secondary bioeffects to the sonicated brain tissue. Within 24 hours after FUS BBB opening, glia and inflammatory pathways are activated in the sonicated tissue[24,25]. On the order of weeks following FUS BBB opening, stimulation of angiogenesis and neurogenesis in the sonicated tissue have been reported[24,25]. These secondary bioeffects have been predominantly investigated in preclinical applications of FUS BBBO for Alzheimer's disease. In animal models of Alzheimer's disease, researchers have demonstrated that FUS BBB opening can promote hippocampal neurogenesis[26,27], reduce amyloid-β plaques and phosphorylated tau[28,29], and improve memory and cognitive function[27,30]. These secondary effects should be considered when evaluating therapeutic effects of FUS BBB opening. Further, these effects have the potential to

combine additively or synergistically with therapeutics delivered concurrently with this FUS BBB opening approach.

2.3 Clinical Translation of FUS Therapies for CCM at UVA

Recently, numerous clinical trials employing MR-guided FUS for the treatment of brain pathologies have been initiated, with patients undergoing over 12,000 FUS-mediated brain treatments as of 2022[31]. The University of Virginia (UVA) is at the forefront of this clinical translation, hosting multiple clinical MR-guided FUS systems, including Insightec Exablate Neuro and NaviFUS, which are equipped with transducers for BBB opening, sonodynamic therapy, and thermal applications. In collaboration with Insightec, UVA is a participating site for clinical trial NCT03551249, investigating the delivery of multiple cycles of Temodar to glioblastoma using the FUS system. Concurrently, in collaboration with NaviFUS, UVA is leading the clinical trial NCT06039709, evaluating sonodynamic therapy in patients with recurrent glioblastoma. Further, UVA has earned distinction as the first FUS Center of Excellence and was recently recognized as a CCM Center of Excellence, one of only twelve in the nation. Notably, UVA is the sole institution recognized as a Center of Excellence for both CCM and FUS. Thus, UVA is an exceptional environment for advancing the clinical translation of FUS technologies in the treatment of CCM.

CHAPTER 3: MAGNETIC RESONANCE IMAGING OF MOUSE CEREBRAL CAVERNOMAS REVEAL DIFFERENTIAL LESION PROGRESSION AND VARIABLE PERMEABILITY TO GADOLINIUM

Delaney G. Fisher[#], Khadijeh A. Sharifi[#], E. Zeynep Ulutas, Jeyan S. Kumar, M. Yashar S. Kalani, G. Wilson Miller, Richard J. Price, and Petr Tvrdik. *Arteriosclerosis, Thrombosis, and Vascular Biology,* 2023, 43:958-970. DOI: 10.1161/ATVBAHA.122.318938

[#]authors contributed equally

3.1 ABSTRACT

Background: Cerebral cavernous malformations, also known as cavernous angiomas, are blood vessel abnormalities comprised of clusters of grossly enlarged and hemorrhage-prone capillaries. The prevalence in the general population, including asymptomatic cases, is estimated to be 0.5%. Some patients develop severe symptoms, including seizures and focal neurological deficits, whereas others remain asymptomatic. The causes of this remarkable presentation heterogeneity within a primarily monogenic disease remain poorly understood.

Methods: We established a chronic mouse model of cerebral cavernous malformations, induced by postnatal ablation of *Krit1* with *Pdgfb-CreERT2*, and examined lesion progression in these mice with T2-weighted 7T magnetic resonance imaging (MRI). We also established a modified protocol for dynamic contrast-enhanced MRI and produced quantitative maps of gadolinium tracer gadobenate dimeglumine. After terminal imaging, brain slices were stained with antibodies against microglia, astrocytes, and endothelial cells.

Results: These mice develop cerebral cavernous malformations lesions gradually over 4 to 5 months of age throughout the brain. Precise volumetric analysis of individual lesions revealed nonmonotonous behavior, with some lesions temporarily growing smaller. However, the cumulative lesion volume invariably increased over time and after about 2 months followed a power trend. Using dynamic contrast-enhanced MRI, we produced quantitative maps of gadolinium in the lesions, indicating a high degree of heterogeneity in lesion permeability. MRI properties of the lesions were correlated with cellular markers for endothelial cells, astrocytes, and microglia. Multivariate comparisons of MRI properties of the lesions with cellular markers for endothelial and glial cells revealed that increased cell density surrounding lesions correlates with

stability, whereas denser vasculature within and surrounding the lesions may correlate with high permeability.

Conclusions: Our results lay a foundation for better understanding individual lesion properties and provide a comprehensive preclinical platform for testing new drug and gene therapies for controlling cerebral cavernous malformations.

3.2 INTRODUCTION

Cerebral cavernous malformations (CCM), also referred to as cavernomas, are hemorrhage-prone, slow flow venous lesions that arise in the central nervous system and affect approximately 0.5% of the general population[32–34]. CCM form as a result of bi-allelic mutations in one of the three main causative genes—*KRIT1*, *CCM2*, or *PDCD10*[1]. Homozygous germline mutations are embryonic lethal in mice and, presumably, humans[35–37]. Heterozygous germline loss-of-function mutations show variable frequency in different human populations[38,39]. While usually asymptomatic outwardly, CCM have been associated with increased vascular permeability[14,40]. Further, the increased incidence of a second somatic mutation can drive the familial form of the disease, which presents with earlier disease onset and a higher lesion burden, compared to sporadic cases caused solely by biallelic somatic mutations[41,42].

One outstanding mystery regarding CCM is the diversity of patient symptom presentation and the degree of symptom severity[43–45]. Some patients with CCM can experience disabling symptoms that commonly include weakness, numbness, severe headaches, vision changes, and difficulty with language. More severe symptoms can include stroke, seizures, and even paralysis. Meanwhile, other patients remain asymptomatic. Symptoms typically arise due to cavernomas that have hemorrhaged. However, the trajectory of clinical outcomes of lesions remains unpredictable. Many investigations have been conducted to better understand the heterogeneity of disease severity at the genetic level. For instance, it has recently been discovered that *PIK3CA* gain of function mutations can co-exist with CCM mutations within lesions and may be associated with more severe disease presentation[42,46,47]. Studies have been conducted to utilize MR scans of patients to correlate lesion stability (i.e. growth and hemorrhage risk) with MR-assessed features of permeability and susceptibility (iron deposition)[11,13,48,49]. While these studies show correlations of instability with lesion permeability and susceptibility, they fail to elucidate the molecular or cellular basis within and surrounding lesions that correspond with these MR features.

Despite the extensive effort to develop predictive models[50,51], the variability in patient presentation remains to be wholly explained. Recommendation of clinical treatment cannot be fully informed without understanding of lesion trajectory.

Animal models of CCM that reflect the human pathology and patient heterogeneity are necessary for uncovering the heterogeneity seen in patients. Traditionally, acute animal models have been used for rapid screenings of pharmaceutical agents, but they lack many key features of the human pathology. Recently, strides have been made in developing chronic models of the disease that better encompass the human pathology. Cre-inducible models have proven useful for emulating loss of CCM gene heterozygosity in humans. Indeed, chronic models of *Pdcd10* and *Ccm2* mutations have recently been generated and characterized[52,53]. *Krit1* mutations are the most prevalent causation of the disease. However, chronic models of *Krit1* have had limited characterization and have been largely confined to postnatal tamoxifen induction at P1, restricting lesions to the cerebellum and retina[54,55].

Despite progress with these new models, most have yet to be robustly characterized with clinically relevant procedures. As MRI is a staple of CCM diagnosis and monitoring in patients, it is equally needed in pre-clinical studies for interpreting mechanistic investigations of CCMs in the context of human disease and for designing improved therapeutic interventions[56]. Prior to therapeutic intervention, it is imperative to understand the baseline progression of the disease without therapeutic intervention and to determine optimal timing of therapeutic intervention. Furthermore, MR sequences that can evaluate lesion permeability and hemosiderin deposition have been developed in patients with the goal of predicting stability of cavernomas in terms of their growth and hemorrhage[11–14]. Developing these MR sequences for mouse models of CCM would enable improved assessment of therapeutic intervention risk (i.e., acute hemorrhage due to therapy) and allow for longitudinal monitoring of therapeutic efficacy towards stabilizing the volume and bleeding of treated cavernomas. To this end, we have generated a chronic, tamoxifen

inducible *Krit1* model with reduced tamoxifen dose and delayed induction that recapitulates the human CCM pathology. We then developed MRI protocols to enable longitudinal characterization of individual lesion progression throughout the whole brain in terms of lesion volume and permeability. We ensured that our MRI protocols align with immunohistochemical staining of lesions. Further, we identified relationships between our MRI-assessed features of lesions and cellular responses within and surrounding individual lesions. Together, this study lays the foundation for better prognostication of CCM lesion behavior.

3.3 RESULTS

3.3.1 DELAYED POSTNATAL DELETION OF KRIT1 IN THE PDGFB DOMAIN GENERATES A CHRONIC CCM MODEL WITH MULTIPLE LESIONS DISTRIBUTED THROUGHOUT THE BRAIN

To study CCM lesion properties in the adult mouse brain, we developed a genetic strategy that gradually generates cavernomas throughout the entire brain over the young adult life span. Traditionally, tamoxifen-induced deletion of conditional CCM alleles was initiated soon after birth (postnatal days P1-P3). However, this early timing severely affects the rapidly developing murine cerebellum, leading to the formation of multiple hemorrhage-prone lesions and a high mortality around one month of age. Delaying the timing of tamoxifen injection to later stages of angiogenic development (P6-P8) was previously found to reduce the lesion burden in the *Pdcd10* model of CCM[53]. We have therefore delayed CCM gene ablation to postnatal day 5-7 (P5-P7). In our approach, we crossed the males of the *Pdgfb* $^{iCreERT2\text{-}IRES\text{-}EGFP}$ strain[57] (hereafter *Pdgfb-CreERT*) with females harboring the floxed *Krit1* allele[55]. The *Pdgfb-CreERT* studs also carried the null (germline-excised) *Krit1* allele (*Krit1* $^{fl/null}$), emulating familial inheritance pattern of the disease. Only heterozygous progeny of the *Pdgfb-CreERT*; *Krit1* $^{fl/null}$ genotype were used. A single injection of dilute tamoxifen in the dorsal subcutaneous region reliably induced lesion formation beginning at 1 month of age and extending through young adult life (4-6 months; **Figure 3.1A**). Lesions form throughout the whole brain; frequently in the periventricular striatum and along the hippocampal folds, but are also regularly found in the cerebellum, olfactory bulb, thalamus, cerebral cortex and brainstem (**Figure 3.1B, Figure 3.S1).** Most mice of this model appear grossly similar to their littermate controls; however, some mutants developed anal prolapse or hydrocephalus. We used a T2-weighted MRI sequence, described below, to detect lesions in live

animals. We confirmed that hypo-intensities detected with T2 MRI *in vivo* can be unequivocally matched with vascular lesions identified in brain cryosections from these animals with isolectin IB4 (**Figure 3.1C**), establishing a robust correlation between MRI and histology. Thus, delayed ablation of *Krit1* generates CCM lesions over time throughout the brain and these lesions can be readily identified with MR imaging, and cross-examined with histology and immunohistochemistry.

3.3.2 Longitudinal MRI Demonstrates Dramatic Increases in Individual Lesion Size and Total Lesion Burden With Age

We systematically measured lesion burden in the CCM mice using a three-dimensional T2-weighted isotropic fast spin-echo MRI sequence (T2-SPACE), which enables 3D image acquisition with a high resolution and relatively short scan times[58,59]. Traditional sequences for CCM detection, such as T2*-weighted gradient echo and susceptibility weighted imaging (SWI), have an increased sensitivity to lesions but come at the cost of an enlarged distortion of cavernoma size due to volume averaging and poor spatial resolution. We therefore employed the T2-SPACE sequence at 7T magnetic strength, as previously optimized for the ClinScan MRI Animal Scanner (Bruker Corporation) used in this study. In line with published literature, T2-SPACE robustly delineated the lesion dimensions as well as internal architecture[60,61].

We used longitudinal T2-SPACE on 9 mice from 5 distinct litters at 5 time points: At 1 month of age (n=3 from 2 litters), 2 months (n=7 from 4 litters), 3 months (n=3 from 2 litters), 4 months (n=5 from 4 litters), and 5 months (n=1; **Figure 3.2**). This imaging revealed that CCM formation began in low numbers at 1 month of age, and CCM formation progressed with age throughout the entire brain. By tracking the total lesion number and combined lesion volume for a given mouse at each imaging timepoint (**Supplemental Video 3.1**)**,** we found that cumulative lesion burden increases with age and accelerates after 3 months of age (**Figure 3.2A-B**). The

median total lesion volume in the brain for a mouse was 0.041mm^3 at 1 month of age, 0.044mm^3 at 2 months, 0.714mm^3 at 3 months, 18.486 mm^3 at 4 months, and 46.721 mm^3 at 5 months. T2-SPACE images of each mouse were then analyzed to track individual lesions across imaging timepoints. This individual lesion analysis revealed that lesions in every mouse displayed variable growth rates, including negative rates (i.e. shrinkage of lesion size; **Figure 3.2C**). However, the majority of individual lesions increased in size with age (**Figure 3.S2**). Altogether, our chronic *Krit1* CCM mouse model displays progressive lesion formation and increasing cumulative lesion burden with age, which is seen in patients with familial CCM[43,62,63]. These results indicate that our model is well-suited for studying individual and variable lesion dynamics with context relevant to the human pathology. Of note, susceptibility-weighted imaging (SWI) MRI sequences are also used due to their increased sensitivity to inhomogeneities in magnetic field strength surrounding iron-rich lesions. This sequence often produces what is called a "blooming" artifact[2,10]. We tested a SWI sequence optimized for the 7T ClinScan MRI scanner and imaged CCM animals immediately prior and after acute LPS-mediated inflammation. This approach demonstrated a greater sensitivity to post-infection lesion increases due to presumed bleeding (**Figure 3.S3**). However, this increased sensitivity to susceptibility effects also enlarges lesions in the produced image by distorting their perceived size as previously described[64,65], disqualifying this approach from accurate volumetric assessment of CCM lesions.

3.3.3 T1 Contrast Maps of MultiHance deposition reveal individual lesion permeability

We next sought to characterize the lesion "leakiness", or internal permeability, with MultiHance (gadobenate dimeglumine), a ~1 kDa MRI gadolinium-based contrast agent. We used a modified version of dynamic contrast enhanced (DCE) MRI[66] that we have termed T1 contrast

mapping, as described in the Methods and **Figure 3.S4**. Briefly, T1 maps were constructed from MR images acquired from CCM mice prior to and following a MultiHance bolus injection. The T1 changes due to contrast accumulation were used to determine local concentrations of the contrast agent. In practice, the total deposition of gadolinium serves as a measurement of lesion leakiness, which lends insight into the potential hemorrhage risk of a lesion and its clinical instability. Compared to traditional DCE methods, which provide temporal information about gadolinium accumulation but are typically confined to a few MR slices of the brain[67], our T1 contrast mapping approach enables whole brain analysis of lesion permeability.

We employed longitudinal T1 contrast mapping on 6 of the 9 mice that received volumetric image analysis. A dataset was acquired for ages of 1 month (n=1), 2 months (n=4 from 3 litters), 3 months (n=2 from 1 litter), 4 months (n=3 from 3 litters), and 5 months (n=1; **Figure 3.3**). T1 mapping generated gadolinium concentration maps that were registered with T2-SPACE sequences, enabling us to quantify gadolinium deposition in T2-SPACE-defined lesions (**Figure 3.3A; Supplemental Video 3.2 and 3.3**). By tracking the combined lesion gadolinium deposition for a given mouse at each imaging timepoint, we found that cumulative lesion leakiness increases with age and appears to accelerate after 4 months of age (**Figure 3.3B**). Median total gadolinium deposition was 0.476 mg at 1 month of age, 0.504 mg at 2 months, 3.08 mg at 3 months, 5.48 mg at 4 months, and 12.5 mg at 5 months. The gadolinium concentration maps of each mouse were then analyzed to track individual lesions across imaging timepoints. This individual lesion analysis revealed that all T1-mapped lesions displayed variations in gadolinium deposition over time, with some lesions even displaying decreased gadolinium deposition at later time points (**Figure 3.3C**). However, the majority of individually tracked lesions increased in gadolinium deposition with age. Taken together, our data shows that the chronic *Krit1* CCM mouse model is characterized by progressive lesion burden with cumulative increases in lesion number, volume,

and leakiness with age. Individual lesions can demonstrate variable changes in size and leakiness, which has also been in seen in human patients[12,14,68–70].

3.3.4 CCM LESION PERMEABILITY IS HIGHLY VARIABLE AND CORRELATES POORLY WITH LESION VOLUME

We asked if any correlation existed between lesion volume and lesion leakiness. The total gadolinium deposition in individual lesions was scaled by lesion volume to produce specific gadolinium concentration. Gadolinium concentrations in individual lesions were then plotted against the lesion volume for each imaging point. Concentration versus volume plots were generated for 1 month of age (n=1), 2 months (n=4 from 3 litters), 3 months (n=2 from 1 litter), 4 months (n=3 from 3 litters), and 5 months (n=1; **Figure 3.4**). A linear regression fitted to these plots revealed no correlation between lesion volume and gadolinium concentration in our measurements. The coefficient of determination (R^2) values were considerably low (show range of values) for all imaging points, suggesting a poor linear relationship. In other words, our analysis reveals a high degree of heterogeneity of lesion permeability between individual animals, and over their lifespan. This heterogeneity was also observed in lesions within individual mice harboring a sufficient number of datapoints (**Figure 3.S5 and 3.S6)**. It is noteworthy that heterogeneity of individual lesion permeability was also observed in human patients using similar MR techniques[12,14]. Thus, our mouse model of CCM appears to recapitulate the heterogenous lesion permeability properties seen in human CCM patients.

3.3.5 INCREASED GADOLINIUM DEPOSITION IN THE LESIONS CORRELATES WITH DECREASED CELL DENSITY IN THE SURROUNDING PARENCHYMA

Lastly, we asked if the MRI features identified in CCM lesions, namely the lesion volume and lesion permeability, correlated with histological features in close proximity of the lesions. For this analysis, we entirely sectioned the L9-M3 brain and stained with antibodies directed against Iba1 (for microglia), GFAP (for astrocytes) and CD31 (aka PECAM-1, for endothelial cells). The nuclear stain DAPI was included in the mounting media. In total, we identified 17 lesions in confocal montages of the coronal sections that were unequivocally matched with the T2-SPACE MRI sequence recorded immediately prior to brain extraction. High resolution images of the lesions were then used to measure fluorescence signal mean intensity of these three cell populations within the lesion, within the 50-μm perimeter of the lesion, as well as within the 100-μm perimeter of the lesion (**Figure 3.5, Figure 3.S7, Table 3.S1**). The specific cell type intensities were then correlated to lesion volume and gadolinium concentration using the non-parametric Spearman's rank correlation test. Correlation analysis revealed that both the 50 μm and 100 μm perimeters for each cell population showed the same correlation direction, and thus, the two perimeters are sometimes jointly referred to as 'outside of the lesion'. Specifically, this analysis revealed that cell density outside the lesions, determined as DNA content by DAPI fluorescence within the immediate 50-μm perimeter of the lesion, was inversely correlated with gadolinium concentration inside the lesion ($r = - 0.61$; $p < 0.01$). The 100-μm ring was also inversely correlated, although at a lower significance level ($r = - 0.51$; $p < 0.05$) (**Figure 3.S8 and 3.S9**). Principal component analysis (PCA) corroborated inverse correlation between gadolinium and DAPI, along with weaker trends towards inverse correlations of gadolinium with microglial and astrocytic densities outside the leaky lesions (**Figure 3.S10**). Conversely, the glial density inside the lesion correlated positively, albeit weakly, with gadolinium concentration. The endothelial cell density both inside and outside the lesion showed weak positive correlations with gadolinium concentration. On the other hand, lesion volume did not correlate with gadolinium deposition ($r = - 0.14$, $p = 0.58$), in line with previous measurements. Of other noticeable trends, microglia and astrocytes both inside and outside the lesions appear to be inversely correlated with lesion

volume, whereas endothelial cells both inside and outside of lesions trended positively with lesion volume (**Figure 3.S9 and 3.S10**).

Our data points to a relationship between high lesion permeability and glial cell density. This data may suggest that dense vascularization, both inside and outside of the lesions, may have negative effects on lesion stability. Conversely, this data could also suggest that lesion instability drives the production of vasculature inside and outside the lesion.

3.4 DISCUSSION

Despite years of investigation, it is still poorly understood why CCM patients have heterogenous presentation in symptoms and lesion phenotypes. Due to the difficulties associated with human studies and limited access to human tissue samples, generation of animal models that reliably capture the human pathology are necessary for studying and furthering treatment of this disease. In this manuscript, we describe a chronic *Krit1* CCM model with delayed tamoxifen induction that replicates human features of lesion development throughout the whole brain and resembles lesion dynamics found in human patients. We also characterize, for the first time, individual CCM lesion progression through the combination of multiple clinical MRI sequences performed longitudinally and immunohistochemical staining of cell populations. This unique merging of a clinically relevant mouse model with advanced MR imaging tools represents a powerful new platform for testing mechanisms of CCM disease, as well as for identifying and pre-clinically testing promising new therapies.

Following generation of our model, we employed clinically relevant MRI sequences longitudinally to characterize lesion progression and dynamics. MRI is commonly used to diagnose and monitor CCM in patients. Despite its ubiquity in the clinic, MR imaging has been largely neglected in many pre-clinical studies, with little data existing on MRI-based characterization of CCM models to robustly assess lesion progression longitudinally. Using T2-SPACE to accurately assess lesion volume and T1 contrast mapping to assess lesion "leakiness," we find that lesion volume and permeability cumulatively increase with age, while rates of growth and leakiness are variable across individual lesions and time points. Notably, this variability in lesion growth rate and permeability has also been shown in patients[12,14,68–70]. Our results differ from that in Mikati et al. where patients with familial CCM were shown to not have a correlation between permeability and age[12]. However, due to the restriction of their DCEQP protocol (which is confined to 4-6 MRI slices) only a limited number of lesions could be tracked in individuals,

whereas our T1 contrast mapping protocol allows for whole brain assessment of lesion leakiness. Thus, we believe that lesion permeability is likely correlated with age for the familial disease if all lesions were examined[12]. The development and translation of these clinical MRI protocols for mouse models of CCM has enabled the establishment of the baseline progression of the disease without therapeutic interventions and for assessment of optimal intervention timing in our chronic model. This understanding of how CCMs progress in mice is needed for testing therapeutic approaches. Additionally, progression of CCMs is clinically relevant as unstable lesions (i.e. lesions that increase in size and hemorrhage) lead to disabling symptoms for patients.

In the clinic, lesion permeability is correlated with increased risk to the patient[12], but relationships that influence lesion permeability remain unknown[14]. We sought to first identify if lesion volume correlated with gadolinium concentration within lesions in our model. We observed that lesion volume and lesion gadolinium concentration have a poor linear correlation. This finding indicates that there is a high degree of heterogeneity of leakiness in individual lesions throughout individual mice and across mice in our model that is not explained by the lesion's volume. Similarly, poor correlation between lesion volume and permeability in patients has also been reported[12,14].

To further understand lesion heterogeneity in our model, we sought to associate our MR features of lesion volume and lesion leakiness with cellular responses within and around lesions. A limited number of lesions have been correlated from MRI and H&E staining previously[71], but this is the first association of MRI and specific cell population markers to our knowledge. Spearman non-parametric correlation of our MR features and cell population markers suggested that more permeable lesions contain greater endothelial cell populations within and around cavernomas than less permeable lesions. Meanwhile, less permeable lesions trend toward higher astrocyte and microglial populations surrounding cavernomas than more permeable lesions.

The findings of this study have to be seen in light of some limitations. First of all, the development of a chronic CCM model with Krit1 mutations was done in the absence of preexisting information on the lifespan of these mutants. Consequently, some of the observations in this work were affected by lack of statistical power due to diminishing size of the cohorts. Specifically, only one animal was imaged with MRI at 5 months after birth, and the comprehensive analysis correlating MRI and histological profiles was successfully completed in a single animal. In future experiments, the high mortality rate can be mitigated by reducing the Krit1 gene ablation with a lower dose of tamoxifen, or by using a brain endothelial cell-selective Cre driver Slco1c1-CreERT. In fact, a significant cause of health decline in our aging Krit1 colony were gastrointestinal comorbidities such as rectal prolapse.

Next, our work takes the first step towards correlative analysis of MRI measurements of lesion permeability with molecular profiles in the mouse models of CCM. While performed in one representative animal, the extensive and evenly distributed lesion load in this specimen allowed appropriate statistical analysis. We found that the density of nuclear stain DAPI immediately outside the lesions correlated significantly and inversely with gadolinium deposition in the lesions, possibly combining the decreases in GFAP- and Iba1-staining that also trended similarly. Our findings that GFAP-positive astrocytes are less abundant around highly permeable lesions is different from the observations of Lopez-Ramirez at al., who recently postulated that astrocyte drive neurovascular dysfunction in the disease[72]. These differences could be ascribed to changing dynamics at different stages of this cellular interaction. Further, it should be noted that cell and vascular density varies greatly in various brain locations, which could have also affected the assessments of cell density surrounding lesions. More multifaceted research is warranted to better elucidate the molecular underpinnings of CCM formation and stability.

Finally, while we have advanced MRI approaches to the mouse CCM model, more work is needed to strengthen pre-clinical MRI applications for cavernoma dynamics. It will be important

to characterize if high gadolinium content inside the lesion correlates positively with gadolinium leakage in the surrounding brain parenchyma, which is clinically more relevant. It is also highly desirable to develop new sensitive MRI sequences for quantitative susceptibility measurements (QSM) suitable for high magnetic fields, which will enable more sensitive drug testing in the animals, especially in combination with more high-throughput approaches using automated segmentation algorithms. A robust dynamic contrast enhanced MRI method also remains a challenge in the mouse model, which would enable measurements of permeability rates within cavernomas. The development of these MRI techniques will be a continual focus for our group moving forward, enhancing pre-clinical CCM research to better inform clinical practice.

3.5 CONCLUSION

As chronic models of CCM are designed to test mechanistic and therapeutic avenues that inform clinical practice, it is imperative that these models' representation of the clinical pathogenesis is validated. To enable clinically analogous validation of our model, we optimized and employed clinical MR protocols. We show that several characteristics of the human pathology is recapitulated in our chronic model of CCM, including: progressive lesion formation throughout the whole brain that increases with age, changes in size and leakiness of individual lesions over time, and heterogenous permeability of individual lesions. We next used the lesion features assessed from MRI (i.e. lesion volume and leakiness) to lend insight to the cellular populations within and surrounding lesions as determined from IHC. We find that increased cell density surrounding the lesion is correlated with lesion stability, while increases in endothelial cells within and surrounding lesions may correlate with lesion instability. This study is the first to establish the baseline conditions of individual lesions in a chronic *Krit1* CCM murine model, providing insight that is essential to advancing treatment strategies for this debilitating disease.

3.6 Materials and Methods

3.6.1 Animals and Treatments

All animal experiments were approved by the Animal Care and Use Committee at the University of Virginia. The animals were housed under standard laboratory conditions (22°C and 12h/12h light/dark cycle). The *Pdgfb* $^{iCreERT2\text{-}IRES\text{-}EGFP}$ (*Pdgfb-CreERT*) line was described previously[57]. To generate experimental animals, male *Pdgfb-CreERT* mice were crossed to the floxed and null *Krit1* alleles (*Krit1*$^{fl/null}$)[55] to produce the desired genotype *Pdgfb-CreERT*; *Krit1* $^{fl/null}$ males or females. Genotyping was performed by Transnetyx (Cordova, TN) using real-time PCR assays specific for *Krit1* wt, floxed and null alleles, as well as the codon-improved Cre recombinase in *Pdgfb-CreERT. Krit1* gene ablation was induced with a single subcutaneous injection of 50uL of tamoxifen dissolved in corn oil at a concentration of 2mg/mL between postnatal day 5 and 7. To induce inflammatory responses, 0.1 mg/mL solution of lipo-polysaccharides in PBS (LPS, Sigma-Aldrich L4391) was injected in 50 µL i.p., corresponding to 0.25 mg/kg dose, 12 h prior to imaging.

3.6.2 MR Imaging

A 7T small animal MRI scanner (Bruker/Siemens ClinScan) was used to acquire T2-SPACE and T1 contrast images. Mice were imaged monthly, starting as early as one month of age and as late as 5 months of age. To be included in this study, each animal had to have at least two imaging time points conducted. Three-dimensional T2-SPACE MRIs were acquired for all mice in this study using a repetition time of 3000 ms, echo time of 80 ms, pixel size of 125 µm x 125 µm x 100 µm, and 2 averages. Scan time for the T2-SPACE sequence was ~20 min. T1

contrast mapping was executed by performing 3D spoiled gradient echo sequences at various flip angles before, and 5 minutes after, gadolinium contrast injection, including the following flip angles: 1, 2, 4, 8, 12, 20, and 30°. All sequences in this series had a repetition time of 10 ms, echo time of 2.6 ms, pixel size of 187.5 μm x 187.5 μm x 200 μm, and 1 average. The scan time for the total image series (pre and post contrast injection combined) was ~20 minutes. To initially determine the optimal time to acquire the post-gadolinium image series such that gadolinium accumulation is maximized and time is minimized, the post-series was repeated every 4 minutes following gadolinium injection up to 20 minutes. Gadolinium contrast (MultiHance) was injected as a bolus intravenously with a dose of 0.01 mmol diluted in saline at a molarity of 0.2mmol/mL.

3.6.3 Generation of Gadolinium Concentration Maps

Separate pre-contrast and post-contrast T1 maps were calculated from each series of multiple-flip-angle 3D images using standard methods[73]. Briefly, the MR signal magnitude as a function of flip angle θ_n was fit to the function

$$S_n = \frac{M_0 \sin\theta_n \left(1 - e^{-TR/T1}\right)}{1 - e^{-TR/T1}\cos\theta_n}$$

at each pixel containing nonzero signal, using the known value of the repetition time (TR = 10 ms) and sequence of flip angles $\theta_n = 1, 2, 4, 8, 12, 20, 30°$. Deposited gadolinium concentration was then calculated at each brain pixel from the measured pre/post T1 change, using the known relaxivity of MultiHance (R=6.3 L/mmol/s) in the expression:

$$C = \frac{1}{R\left(\frac{1}{T_{1,post}} - \frac{1}{T_{1,pre}}\right)}$$

Physically impossible concentration values (those that were larger than the initial gadolinium concentration in the blood or significantly less than zero, usually occurring in image regions with low SNR) were excluded from further analysis.

3.6.4 Segmentation of Lesions from MR Images

T2-SPACE images and gadolinium concentration maps were processed and analyzed in Horos DICOM viewer. T2-SPACE and gadolinium concentration maps were co-registered with the built-in feature within Horos or manually with custom MATLAB script. Manual segmentation of lesions was made with the freehand tool by outlining lesions in every coronal slice for each mouse and imaging timepoint within the study. Lesion volumes were calculated with the Horos "Compute Volume" feature and recorded. ROIs from T2-SPACE images were transposed onto co-registered gadolinium concentration maps. Total grayscale value within ROIs were recorded and summed across all slices for a given lesion (equivalent to gadolinium mass). Gadolinium concentration was calculated by dividing total gadolinium mass by computed lesion volume. Individual lesions were manually tracked across imaging time points using T2-SPACE images. The same anatomical location of a tracked lesion was validated in each imaging plane (coronal, axial, sagittal) across imaging timepoints. In some instances, distinct lesions from earlier time points had merged into one lesion at later time points. In other cases, lesions from earlier time points were no longer visible on images from later time points. *De novo* lesion formation was found in all animals in our study. If a lesion was obscured due to an imaging-related artifact, the lesion was excluded from analysis at the corresponding timepoint.

3.6.5 Histology

After completion of the final imaging timepoint, mice were transcardially perfused with phosphate-buffered saline (PBS) and 4% PBS-buffered formaldehyde (EMS 15714). Brains were dissected, post-fixed, sequentially equilibrated in 10% and 30% sucrose and embedded in OCT (Andwin Scientific). Frozen brains were cryosectioned at 50- to 80-µm thickness for histology staining, or 25-µm thickness for immunohistochemistry (IHC). To perform histological staining of neurons and blood vessels in 50-µm thick sections, free floating sections were permeabilized overnight in PBS-buffered 0.5% Triton X-100 (Sigma-Aldrich 93443) at 4ºC. Next, the sections were washed 3 times for 5 min with PBS, 1 mM $CaCl_2$, and incubated in the red fluorescent Nissl stain (Neurotrace, Invitrogen N21482, diluted 1:100 in PBS, 1mM $CaCl_2$) for 2 h at room temperature (RT). Following three washes with PBS, 1mM $CaCl_2$, the sections were stained with Alexa Fluor 488-conjugated Isolectin GS-IB4 (Invitrogen 121411, diluted 1:100 in PBS, 1mM $CaCl_2$) overnight at 4ºC. After one final wash with PBS, 1mM $CaCl_2$, the sections were mounted on microscopy slides with DAPI Fluoromount-G (SouthernBiotech, 0100-20) using Secure Seal Spacers (EMS 70327-20S).

3.6.6 IMMUNOHISTOCHEMISTRY

Thawed 25-µm sections were rehydrated with PBS, permeabilized in 0.5% Triton X-100 (Sigma-Aldrich 93443) in PBS for 1h at RT, and blocked with 1% bovine serum albumin (BSA, Jackson ImmunoResearch Labs, 001-000-161), 5% normal donkey serum (NDS, Jackson ImmunoResearch Labs, 017-000-121), and 0.5% Triton X-100 in PBS for 2 h at RT. The primary antibodies, including chicken anti-GFAP (1:200, Aves, GFAP5727980), rabbit anti-Iba1 (1:500, Wako Chemicals USA, 011-27991), goat anti-CD31 (1:20, R&D Systems, AF3628), were diluted in the blocking solution and incubated with mounted brain sections overnight at 4°C. After three 5-min washes with PBS, 0.5% Triton X-100, the sections were incubated with secondary

antibodies, including donkey anti-chicken Alexa 488 (1:500, Jackson ImmunoResearch Labs, 703-546-155), donkey anti-rabbit Alexa 568 (1:500, Invitrogen A10042), donkey anti-goat Alexa 647 (1:500, Invitrogen A21447), diluted in the blocking solution at 1:500 for 2 h at RT. Following final washes, slides were mounted with ProLong Gold antifade reagent with DAPI (Invitrogen, P36935) and cover slipped with Fisherbrand Microscope Cover Glass (12-544-E) for confocal imaging.

3.6.7 Confocal Microscopy

Stained sections were imaged with a Zeiss LSM 880 confocal microscope (Zeiss, Germany) using sequential scanning mode for DAPI, Alexa 488, 568 and 647 dyes. Montages of image stacks (1024 x 1024 pixels, 2 um z-step), tiled in the x-y plane, were processed with Imaris 9.9 (Oxford Instruments) and analyzed with Fiji/ImageJ. Final images were adjusted with Adobe Photoshop and assembled in PowerPoint (Microsoft), or Adobe Illustrator (Adobe Creative Cloud).

3.6.8 Segmentation of Lesions from IHC Images

Fluorescent images were analyzed in ImageJ for grayscale intensities in each channel: Iba1, GFAP, CD31, and DAPI. ROIs of lesion boundaries were manually drawn around the central hypointense void space of each identified lesion (enlarged vessels near the lesion were not included for this ROI). To measure cell populations surrounding the lesions, this lesion boundary was expanded by either 50um or 100um, and the inside ROI was subtracted. Mean grayscale intensity of each of the three ROIs (inside lesion, 50um border, and 100um border) was averaged for all slices within the image stack in a given channel. Mean grayscale intensity for three reference ROIs drawn in nearby non-lesioned locations of the brain tissue in each image were

also averaged across the image stack in a given channel. Lesion associated mean grayscale intensities were normalized to the average reference mean grayscale intensity in the same image to account for variations of cell population expression in differing brain regions. These normalized mean grayscale intensities for Iba1, GFAP, CD31, and DAPI for each lesion were correlated with the same lesion's volume and gadolinium concentration from the last imaging timepoint. Spearman's correlation analysis was then performed with OriginPro's Correlation Plot on the data matrix for 17 lesions and 14 measurements (3 lesion boundaries x 4 channels + lesion volume + lesion gadolinium concentration).

3.6.9 Statistical Analysis

The results were expressed as mean ± standard error of the mean (SEM). In all experiments, the statistical significance was set at $P < 0.05$. Calculations were performed using GraphPad Prism 8 statistical package software (San Diego, USA).

3.6 CHAPTER 3 FIGURES

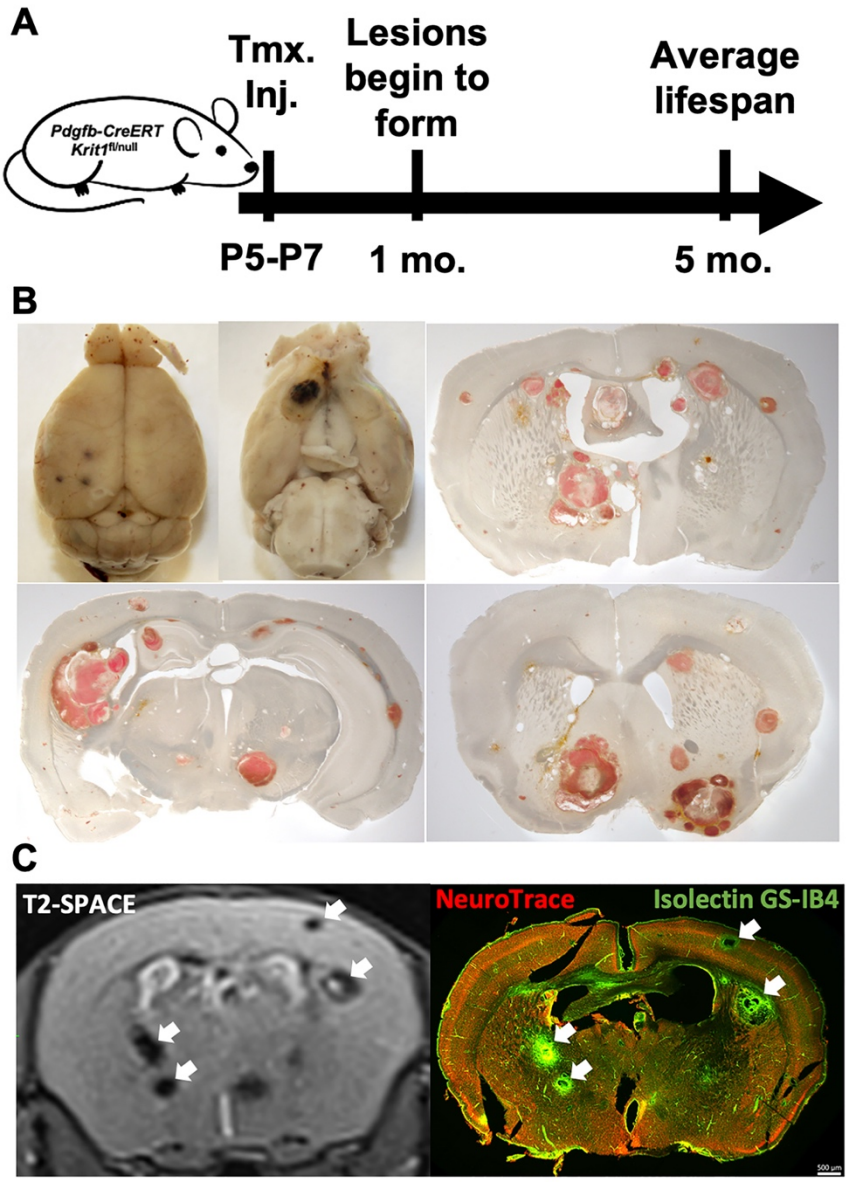

Figure 3.1. Induction of Krit1 ablation at postnatal day 5 or 7 generates chronic CCM murine model with gradual lesion development brain-wide. (**A**) Timeline of chronic CCM model generation and disease phenotype. (**B**) Macroscopic and brightfield images of lesion burden demonstrate lesions form throughout the entire brain. (**C**) Comparison of MRI (left) and IF image (right) of the same CCM mouse brain section demonstrates alignment of lesions between the two imaging modalities. In IF image, lesions are stained with isolectin GS-IB4 (green) and neurons with NeuroTrace (red). Scale bar, 500 μm. White arrows denote lesions.

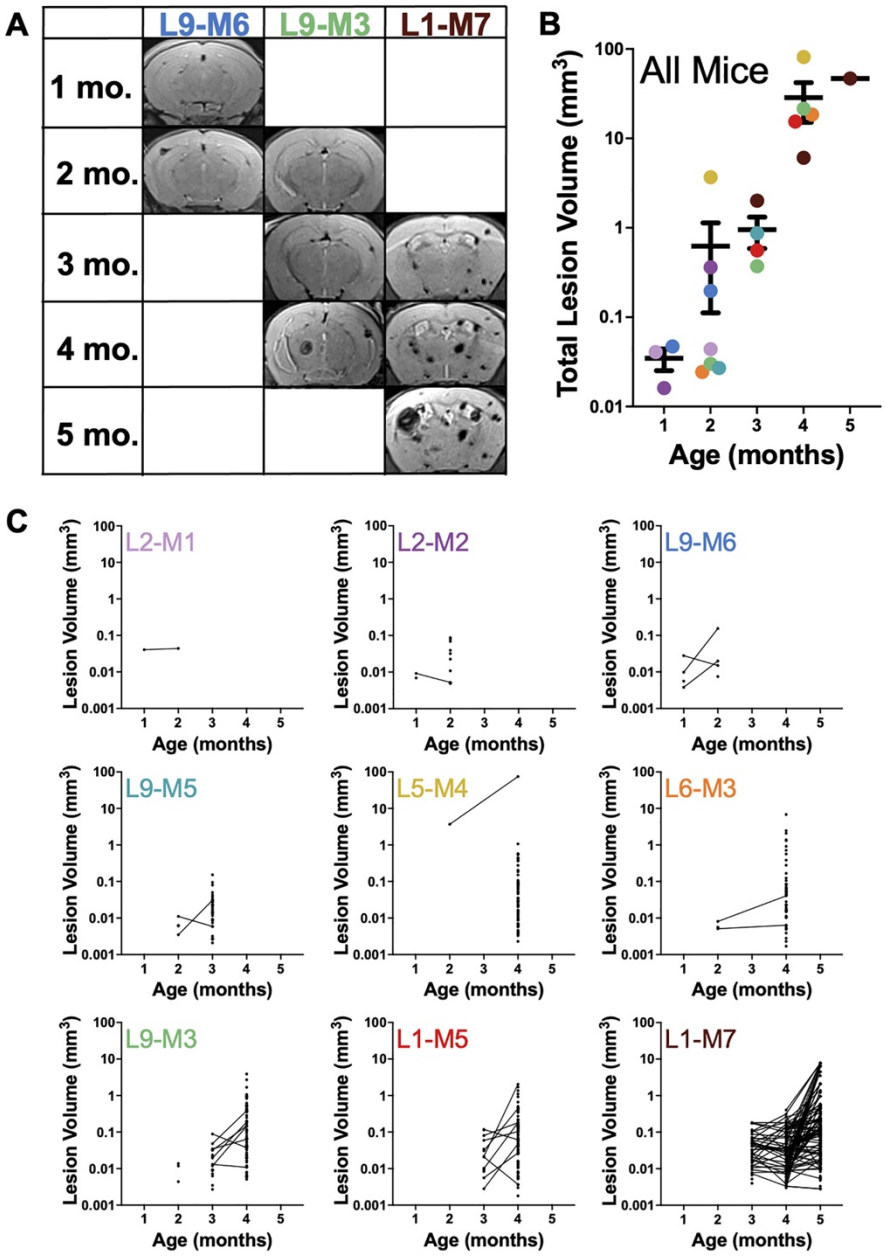

Figure 3.2. Volumetric analysis of lesions from longitudinal T2-SPACE MR images reveals dramatic increases in lesion burden with age and dynamic changes in size of individual lesions. (**A**) Representative T2-SPACE MR images from 3 mice in our cohort, illustrating formation of new lesions and dynamic changes in lesion size across time points. (**B**) Graph of combined lesion volume within individual mouse brains as a function of age for all mice in our cohort. Individual mice represented as a single-colored dot, which corresponds with graph title color in panel C. (**C**) Graphs of lesion volume as a function of age for each mouse in our cohort. Lines indicate lesions identified as the same lesion across imaging time points. Dots without lines indicate de novo lesion formation or lesions that were only identified at a single time point. Graph titles indicate

unique mouse ID where L# denotes litter number and M# denotes arbitrary mouse number within litter. Animated MRI sequences of L1-M7 are shown in the Supplemental Videos 1-3.

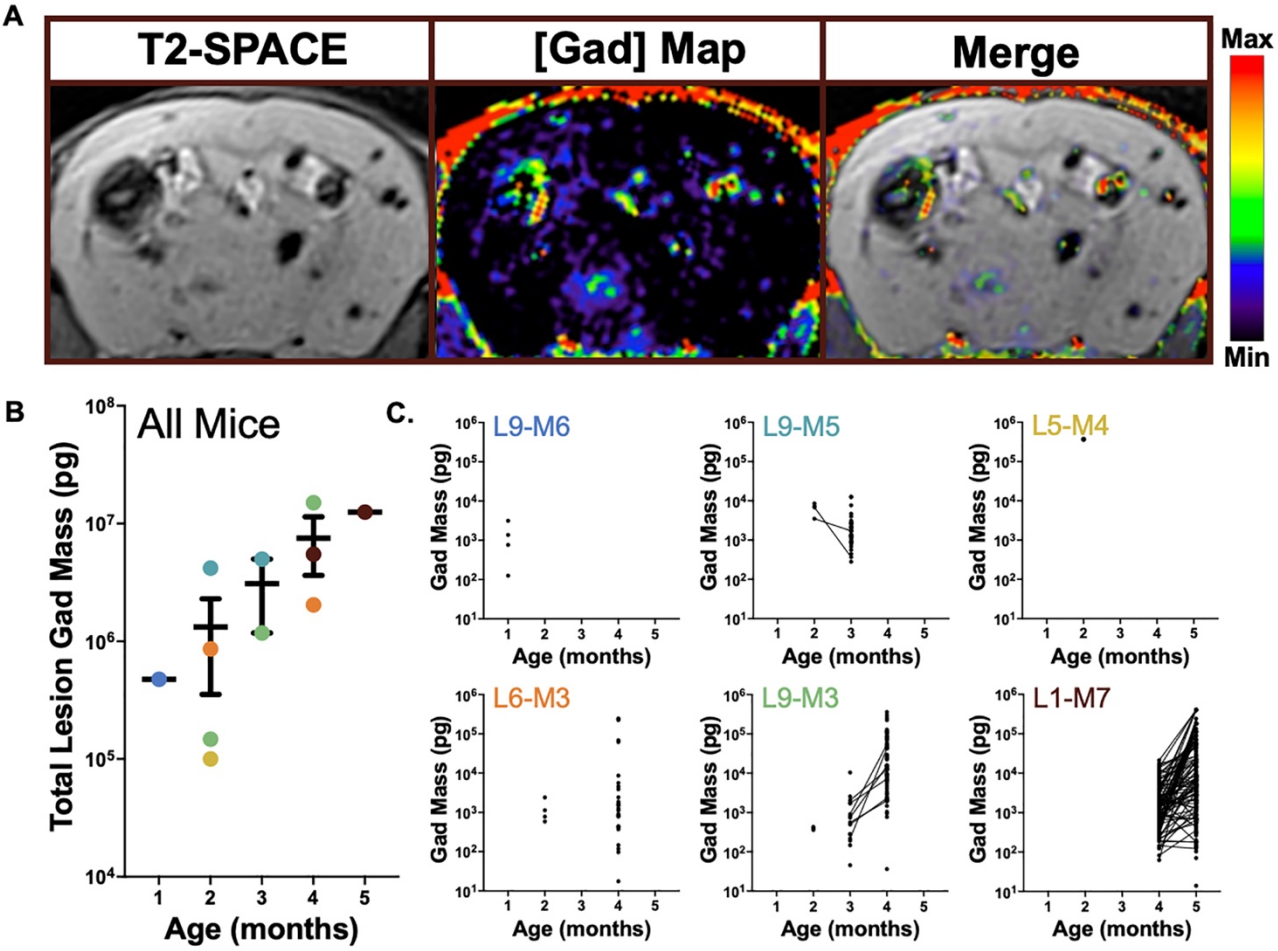

Figure 3.3. Permeability analysis of lesions from longitudinal T1 contrast mapping reveals cumulative increase in lesion permeability with age while individual lesion permeability varies over time. (**A**) Representative MR images of T2-SPACE, gadolinium concentration map (generated from T1 contrast mapping), and merged image of the same brain section, illustrating leakiness of individual lesions in terms of gadolinium deposition. In the gadolinium concentration map, hyperintense areas indicate regions with higher gadolinium deposition. (**B**) Graph of combined lesion gadolinium deposition in mass within individual mouse brains as a function of age for all mice in our cohort. Individual mice represented as a single-colored dot, which corresponds with color of graph title in panel C. (**C**) Graphs of gadolinium deposition in individual lesions as a function of age for individual mice in our cohort. Lines indicate lesions identified as the same lesion across imaging time points. Dots without lines indicate de novo lesion formation or lesions that were only identified at a single time point. Graph titles indicate unique mouse ID where L# denotes litter number and M# denotes arbitrary mouse number within litter. Animated MRI sequences of L1-M7 are shown in the Supplemental Videos 1-3.

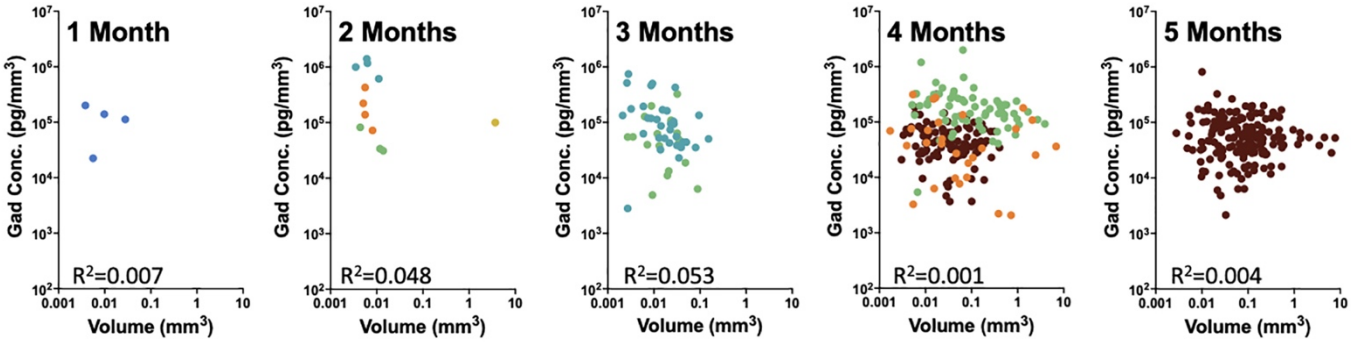

Figure 3.4. Lesion permeability displays a high degree of heterogeneity. Graphs of gadolinium concentration as a function of lesion volume for individual lesions at each imaging timepoint. Individual mice represented as a single-colored dot, which corresponds with color-coding in Figures 2 and 3. Coefficient of determination values indicates poor correlation between gadolinium concentration and volume for each time point, suggesting highly heterogenous permeability of lesions across age in our chronic CCM model.

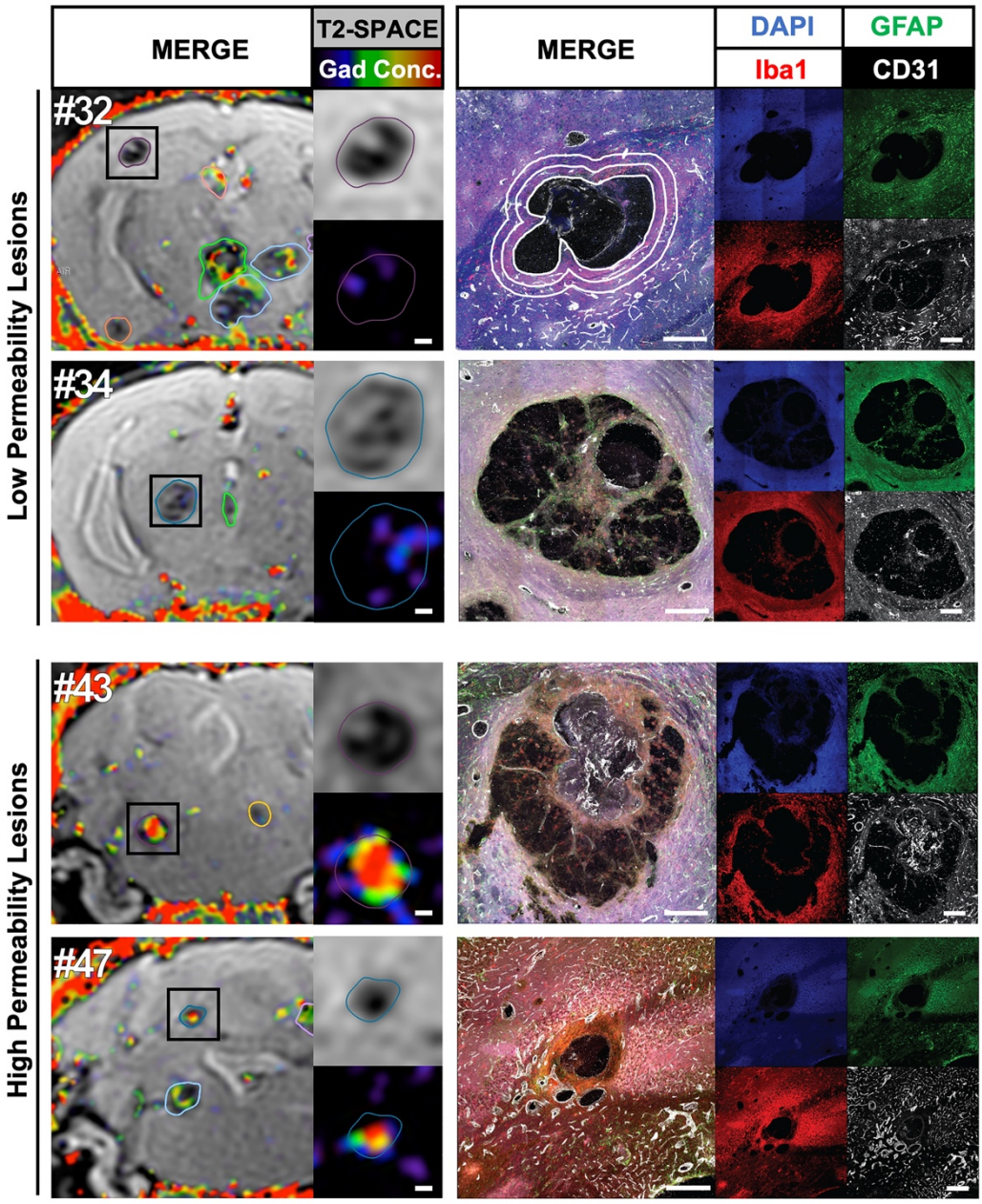

Figure 3.5. The MRI and histochemical signatures of CCM lesions with low and high permeability. Two lesions with the lowest permeability (#32 in the subcortical corpus callosum, MultiHance concentration 41 ng/mm^3; and #34 in the thalamus, MultiHance concentration 58.9 ng/mm^3; see Table S1) are shown on top. Two lesions with the highest permeability (#43 in the brainstem, MultiHance concentration 185.8 ng/mm^3; and #47 in the cerebellum, MultiHance concentration 250.5 ng/mm^3; see Table S1 for an overview of measurements) are shown at the bottom. MRI insets show T2-SPACE images and gadolinium concentration maps of each lesion in detail. Matching IHC images of each DAPI, GFAP, Iba1 and CD31 channels are shown on the right, next to the 4-channel overlay. Large, highly permeable lesions typically contain numerous CD31-positive endothelial cells. All scale bars are 200 μm. White lines drawn on merged IHC image for

lesion #32 exemplify the inside, 50 μm, and 100 μm perimeters used for correlation analysis. See Figure S7 for additional information.

3.7 Chapter 3 Supplemental Figures

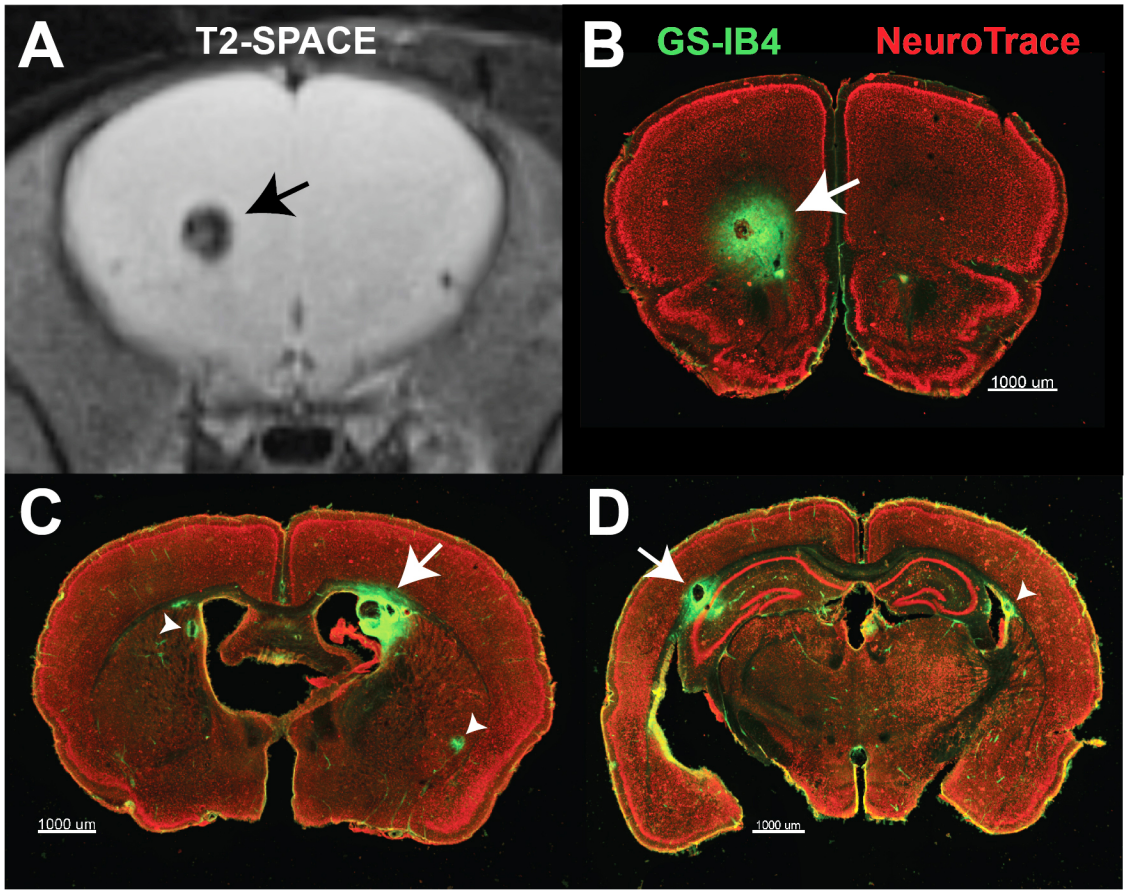

Figure 3.S1. The anatomical distribution of vascular lesions in the *Krit1* CCM model. (**A, B**) Alignment of a T2-SPACE MRI image plane with the corresponding brain section labeled with fluorescent isolectin GS-IB4 (green) and Neuro-Trace Nissl stain (red). (**C**) In this mouse model, cavernous lesions frequently occur in dorsal striatum near lateral ventricles (white arrow). (**D**) CCM lesions are also commonly found in the subcortical white matter of the corpus callosum, often adjacent to the dorsal hippocampus. (White arrow, arrow head).

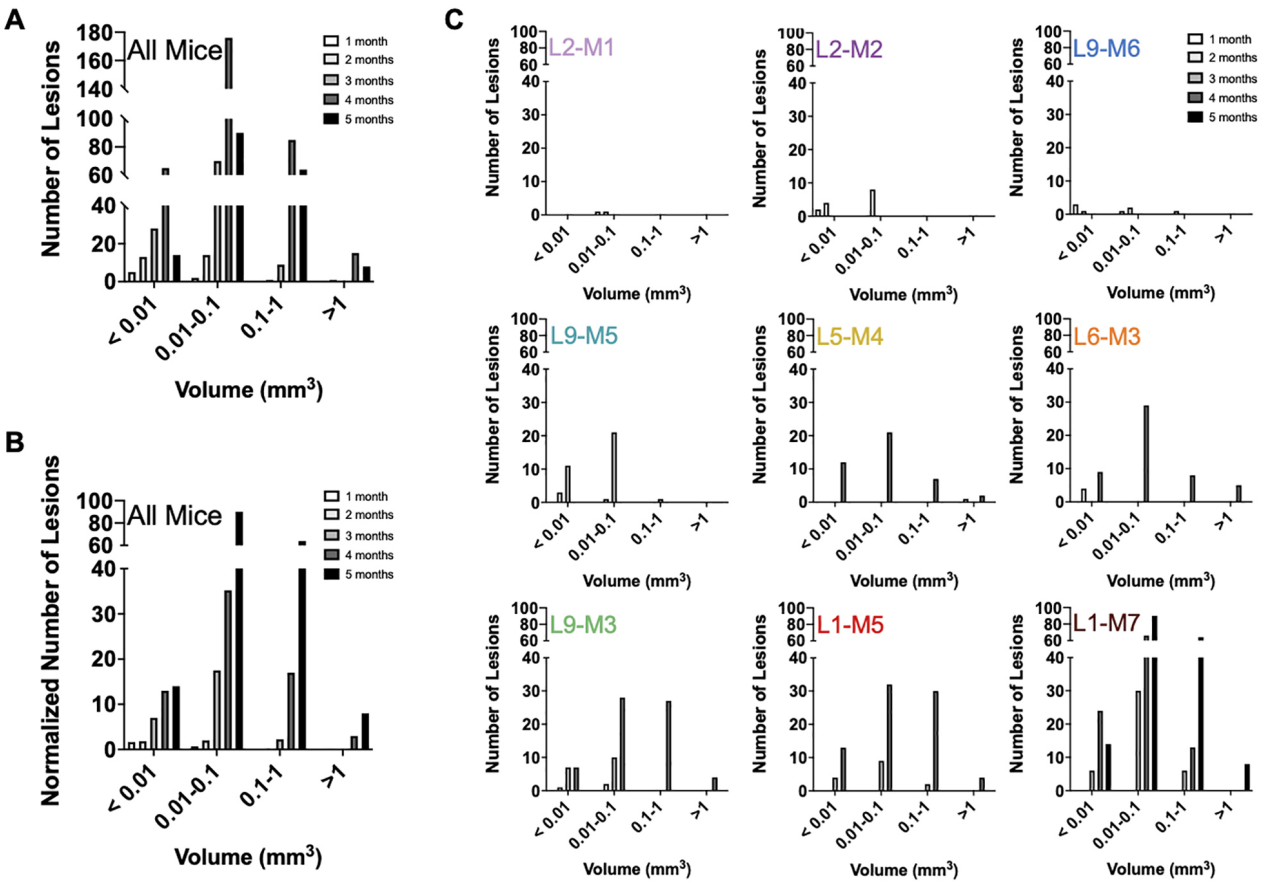

Figure 3.S2. Size distribution of lesions over time in our *Krit1* chronic model. (**A**) Total number of lesions divided across four size categorizations for all mice in our cohort and each imaging time point. (**B**) Data from panel A normalized by the number of mice at each imaging time point. (**C**) Total number of lesions divided across four size categorizations for individual mice in our cohort and each imaging time point. Graph titles indicate unique mouse ID where L# denotes litter number and M# denotes arbitrary mouse number within litter.

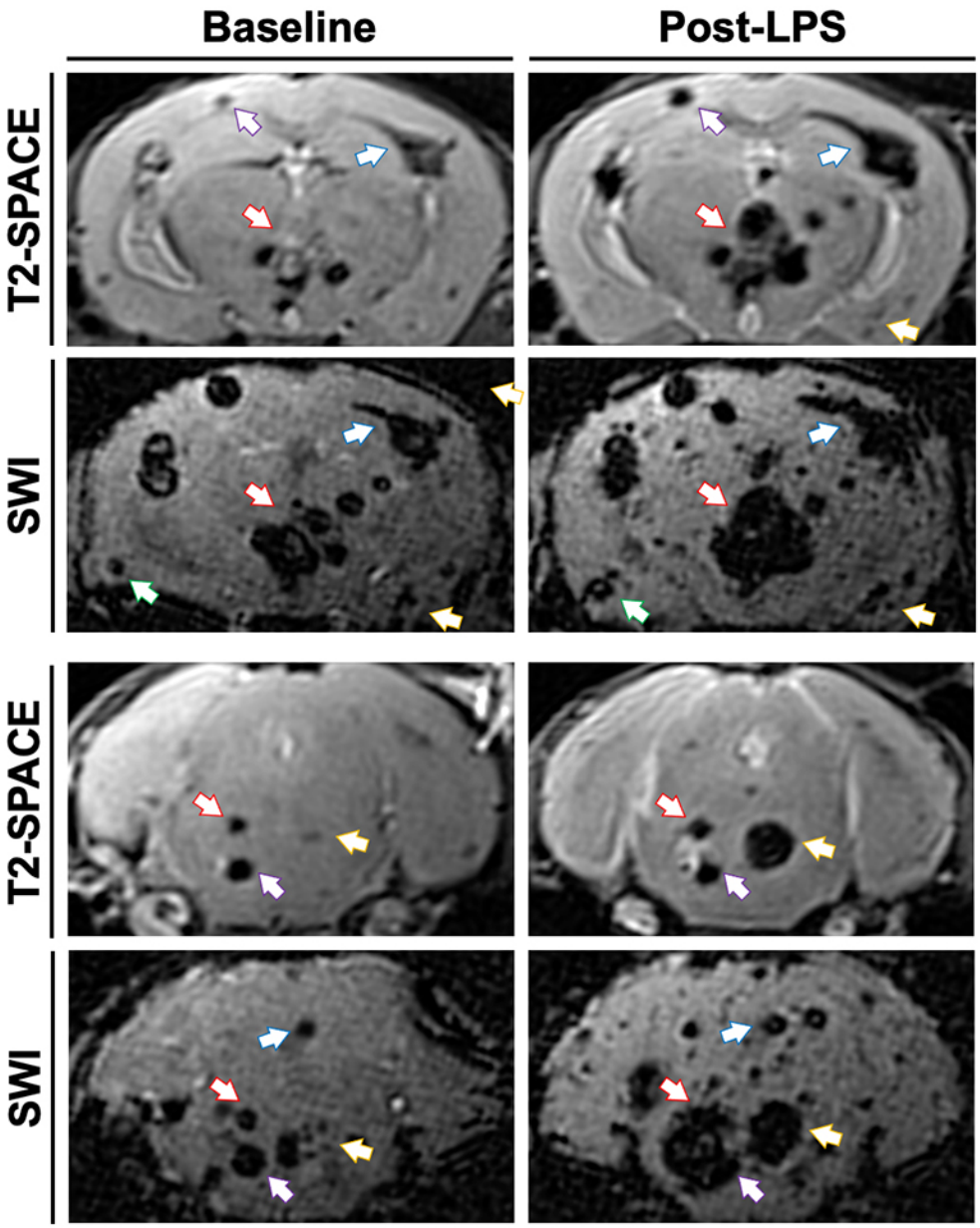

Figure 3.S3. Comparison of T2-SPACE and SWI sequence sensitivity before and after a sudden hemorrhagic episode. The *Pdgfb-CreERT*; *Krit1* $^{fl/null}$ mouse was imaged at Baseline and 12 h after acute mild neuroinflammation induced with LPS (0.25 mg/kg i.p.). Matching coronal planes of T2-SPACE and SWI are shown, demonstrating increased SWI sensitivity to CCM lesions. However, the exaggerated distortion of the lesion size is also apparent. Note the substantial increase in lesion volumes following neuroinflammation, accelerated due to fatal bleeding. Arrows identify the corresponding lesions between MRI sequences and inflammatory states.

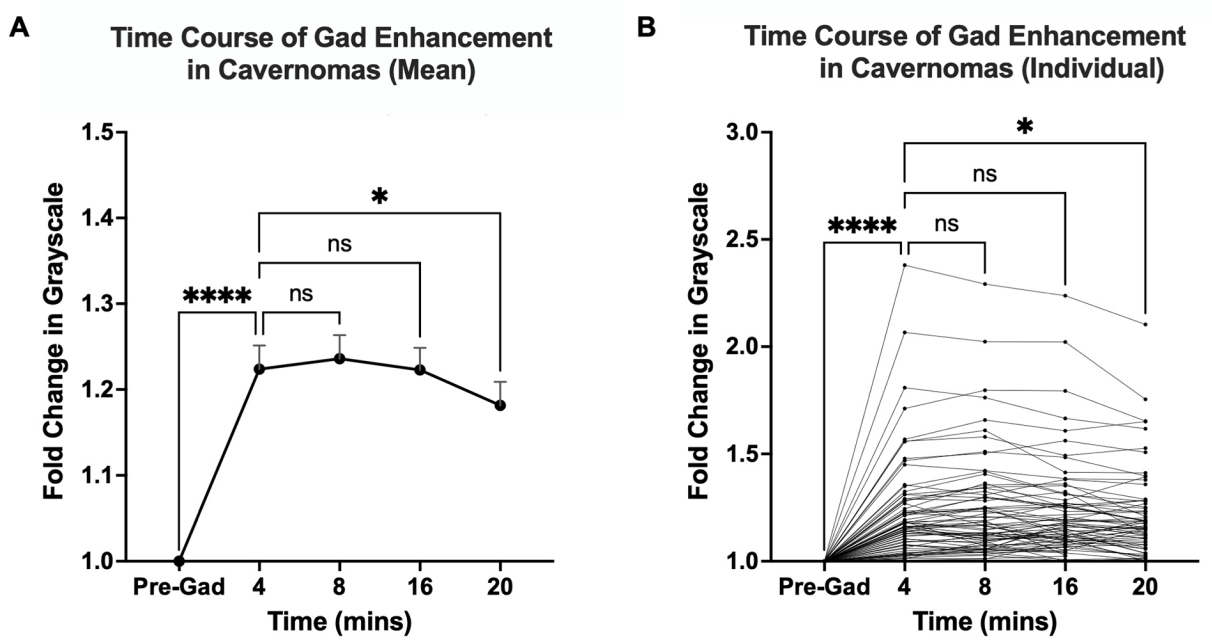

Figure 3.S4. Time course of T1 gadolinium-contrast enhancement within cavernomas in the L1-M7 animal. (A-B) Line graphs displaying fold change in grayscale intensity of 74 cavernomas at various times following gadolinium intravenous injection over pre-gadolinium T1-weighted image. (A) Average fold change in grayscale intensity value for the 74 cavernomas. (B) Individual fold change in grayscale intensity values for the 74 cavernomas. T1 contrast enhancement significantly increases from the pre-gadolinium image to 4 minutes post injection and significantly decreases at 20 minutes post injection. The measurements obtained at 8 min and 16 min were not statistically different from 4 min post injection. One-way ANOVA with Dunnett's multiple comparisons test.

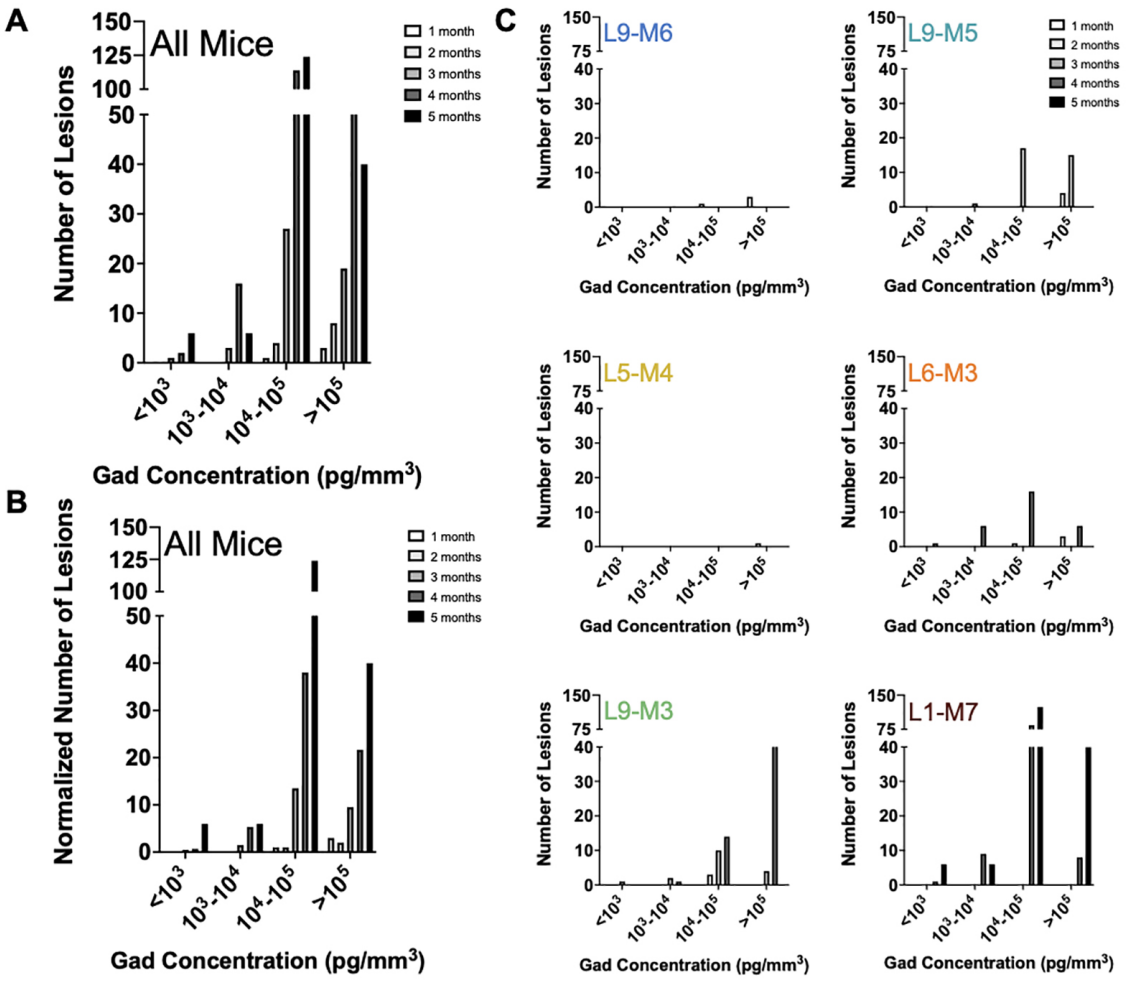

Figure 3.S5. Permeability distribution of lesions over time in our Krit1 chronic model. (A) Total number of lesions divided across four gadolinium concentration categorizations for all mice in our cohort and each imaging time point. (B) Data from panel A normalized by the number of mice at each imaging time point. (C) Total number of lesions divided across four gadolinium concentration categorizations for individual mice in our cohort and each imaging time point. Graph titles indicate unique mouse ID where L# denotes litter number and M# denotes arbitrary mouse number within litter.

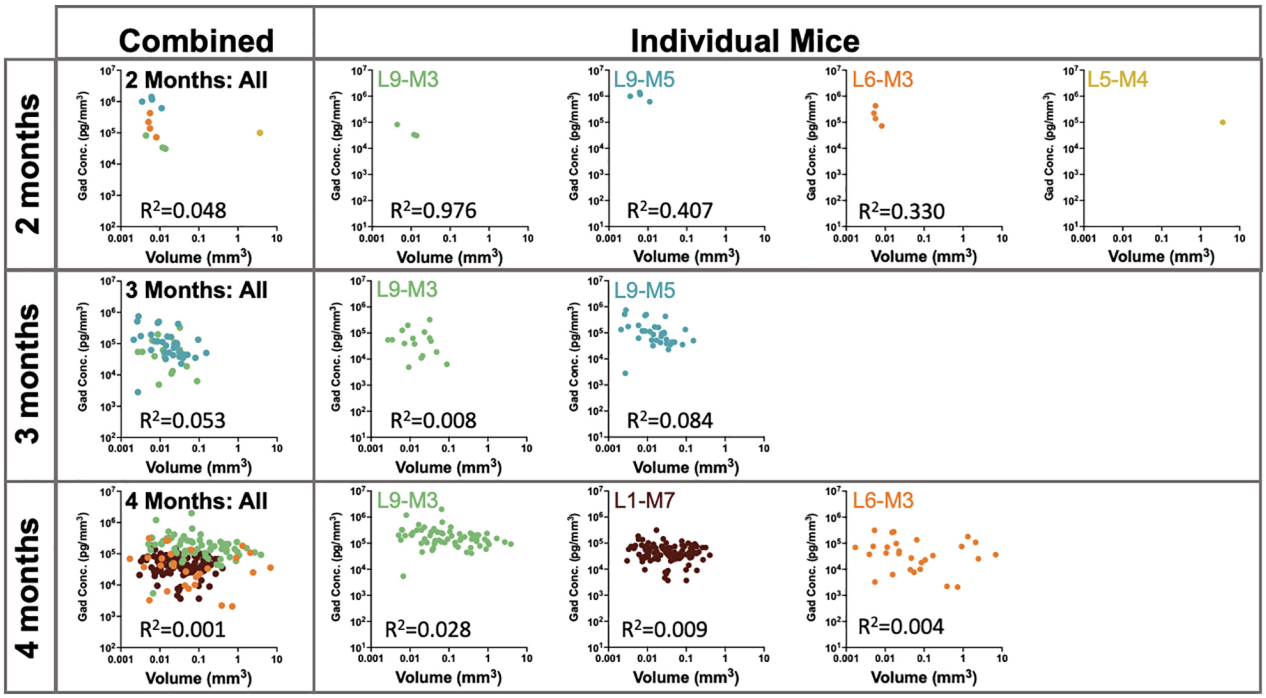

Figure 3.S6. Lesion permeability is poorly correlated with lesion volume. Graphs of gadolinium concentration as a function of lesion volume for individual lesions at each imaging timepoint. Data for all mice at 2 months, 3 months, and 4 months is shown on the left. Data for individual mice and corresponding coefficient of determination values are disaggregated on the right. Coefficient of determination values indicates poor correlation between gadolinium concentration and volume for each time point, suggesting highly heterogenous permeability of lesions across age in our chronic CCM model.

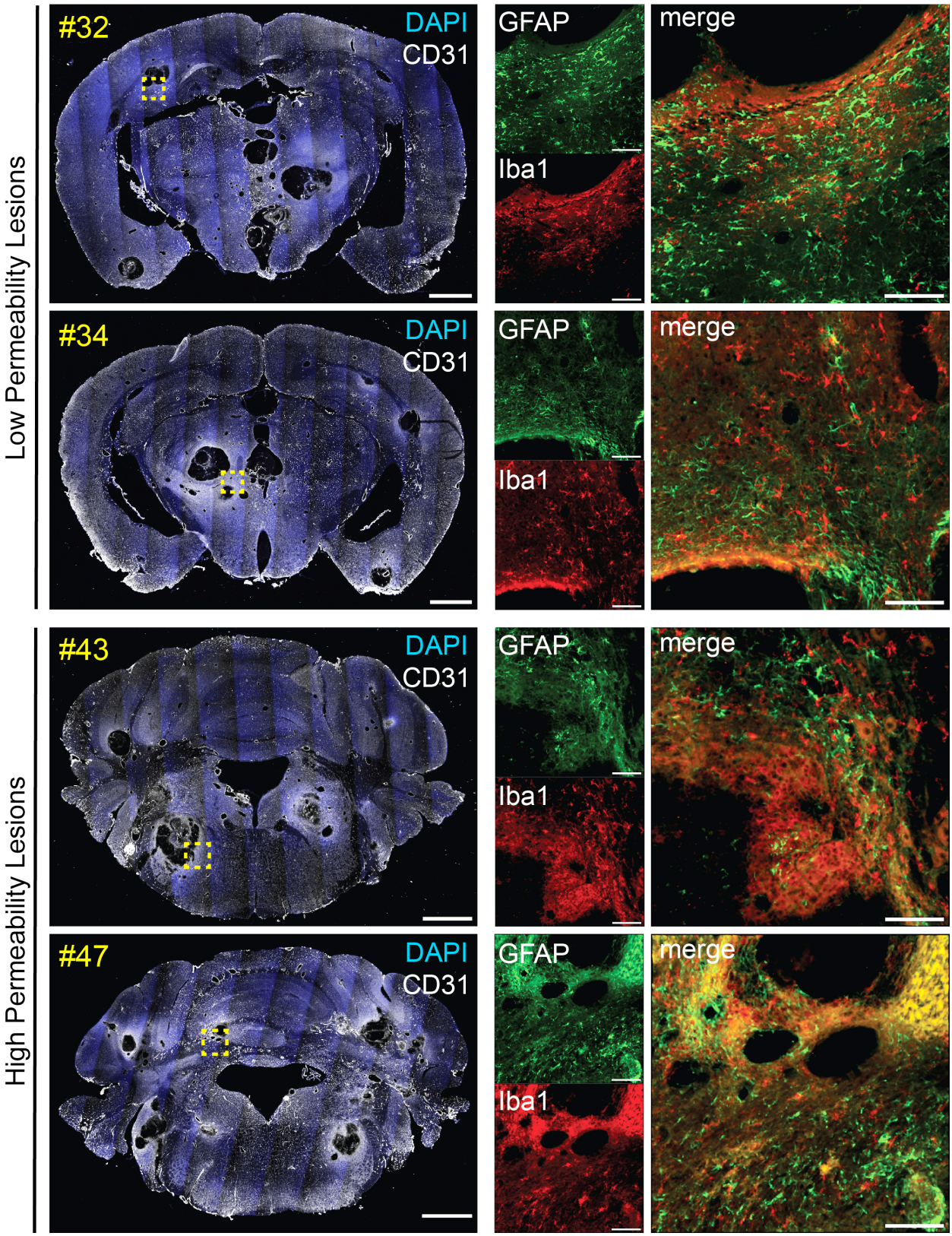
Low Permeability Lesions
High Permeability Lesions
#32
DAPI
CD31
GFAP
Iba1
merge
#34
DAPI
CD31
GFAP
Iba1
merge
#43
DAPI
CD31
GFAP
Iba1
merge
#47
DAPI
CD31
GFAP
Iba1
merge

Figure 3.S7. Anatomical and cellular context of CCM lesions with low and high permeability. On the left: Tiled confocal images of brain coronal sections harboring the lesions with the lowest permeability (#32 in the subcortical corpus callosum and #34 in the thalamus, see Table S1 for an overview of measurements) are shown on top. Two lesions with the highest permeability (#43 in the brainstem and #47 in the cerebellum, see Table S1 for detail) are shown at the bottom. The tiled coronal sections, scanned at a low resolution, show the overlay of nuclear stain DAPI (blue) and CD31 endothelial cell marker (white). The area marked with the yellow dashed box in each coronal section was imaged at a higher resolution, and the corresponding images of GFAP-positive astrocytes (green) and Iba1-positive microglia/macrophages (red), as well as the merged overlay, are shown on the right. The lesions with a high gadolinium content appear to have fewer glial cells in the immediate vicinity of the borders. Scale bars: tiled coronal section images, 1 mm; high-resolution IHC panels, 100 μm.

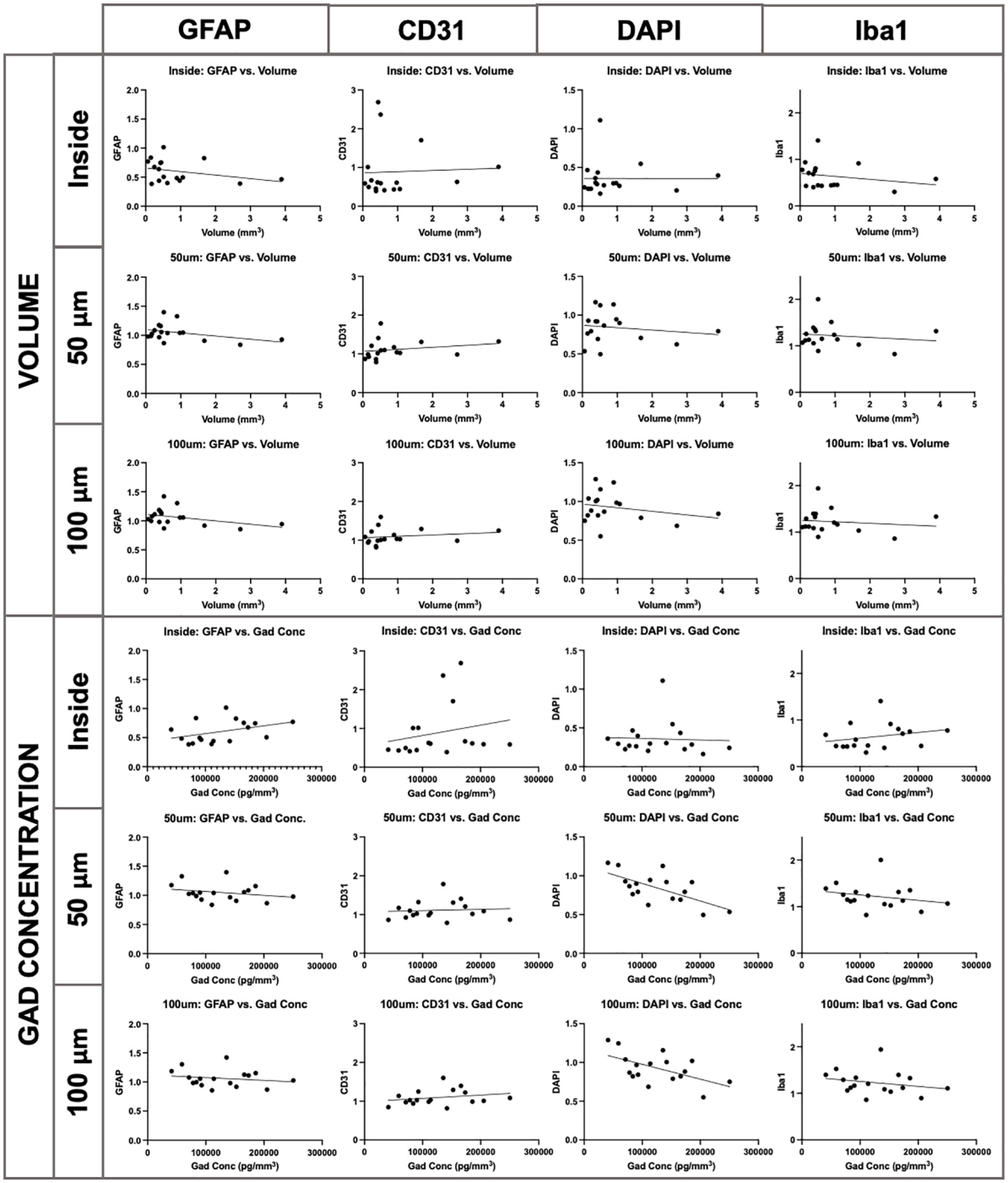
GFAP
CD31
DAPI
Iba1
VOLUME
GAD CONCENTRATION
Inside
50 µm
100 µm
Inside: GFAP vs. Volume
Inside: CD31 vs. Volume
Inside: DAPI vs. Volume
Inside: Iba1 vs. Volume
50um: GFAP vs. Volume
50um: CD31 vs. Volume
50um: DAPI vs. Volume
50um: Iba1 vs. Volume
100um: GFAP vs. Volume
100um: CD31 vs. Volume
100um: DAPI vs. Volume
100um: Iba1 vs. Volume
Inside: GFAP vs. Gad Conc
Inside: CD31 vs. Gad Conc
Inside: DAPI vs. Gad Conc
Inside: Iba1 vs. Gad Conc
50um: GFAP vs. Gad Conc.
50um: CD31 vs. Gad Conc
50um: DAPI vs. Gad Conc
50um: Iba1 vs. Gad Conc
100um: GFAP vs. Gad Conc
100um: CD31 vs. Gad Conc
100um: DAPI vs. Gad Conc
100um: Iba1 vs. Gad Conc
Volume (mm³)
Gad Conc (pg/mm³)

Figure 3.S8. Correlations between MR signatures and IHC signatures. Correlation plots for individual cell populations (astrocytes-GFAP, endothelial cells-CD31, cell nuclei-DAPI, and microglia-Iba1) and MR features (lesion volume and lesion permeability) at different locations around the lesion (inside lesion, 50μm border outside lesion, and 100μm border outside lesion). Dots indicate individual lesions (n=17). Linear regression fitted to each dataset.

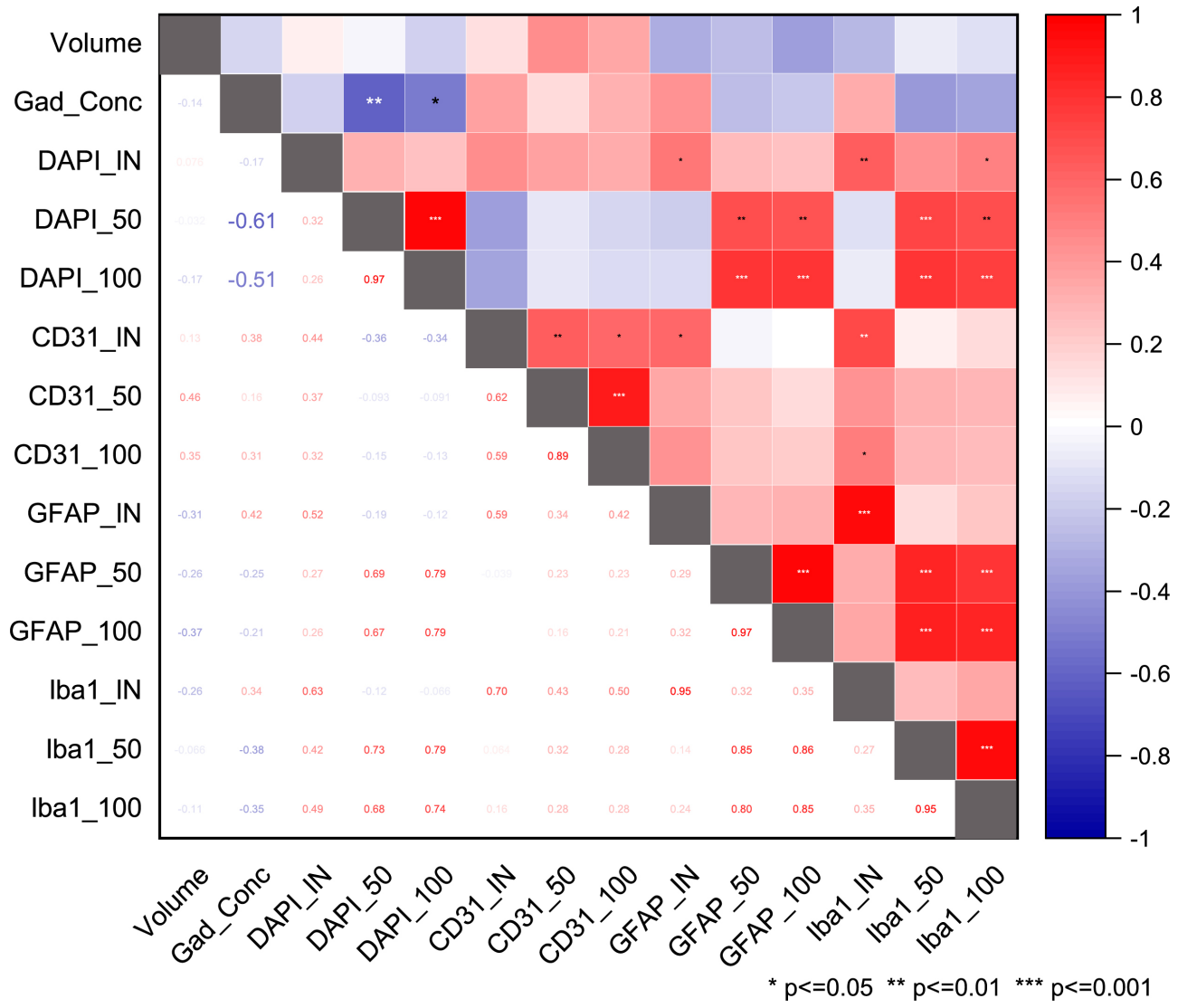

Figure 3.S9. Correlation Matrix Heatplot of 14 variables in 17 different CCM lesions in the L9-M3 animal. Two variables, Volume and Gad Concentration, were measured with MRI, the values of the remaining 12 variables were obtained with confocal image analysis of brain sections stained with IHC inside the lesions, as well as in 50- and 100-μm perimeters outside the lesions. Significant inverse correlations between MRI and IHC were found for gadolinium concentration and DAPI intensity for both 50-μm and 100-μm border perimeters (r = - 0.61, p = 0.009; and r = - 0.51, p = 0.036; respectively). The plot was generated with OriginPro 2020.

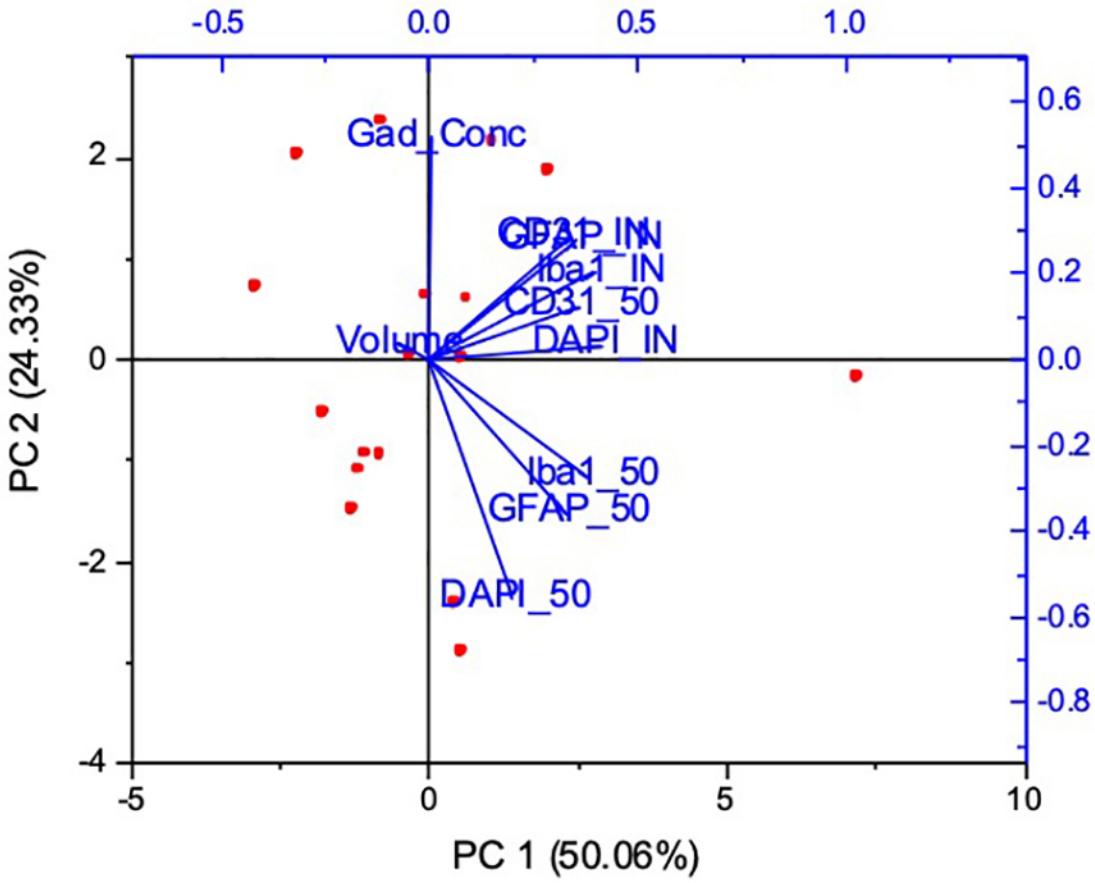

Figure 3.S10. Principal component analysis (PCA) of 10 variables in 17 different CCM lesions in the L9-M3 animal. (Including volume and gad. concentration, as well as the IHC values inside the lesions. Only the 50-µm perimeters were included in this analysis for the sake of clarity). PCA analysis corroborates the inverse correlation of gadolinium concentration and DAPI intensity outside the lesions, and reveals trends towards inverse correlation between gadolinium concentration and Iba1 and GFAP fluorescence intensity outside the lesions. The plot was generated with OriginPro 2020.

3.8 CHAPTER 3 SUPPLEMENTAL TABLES

Table 3.S1. MRI and IHC data on 17 lesions obtained from animal L9-M3.

			Inside Mean (Reps Avg)				100um Mean (Reps Avg)				50um Mean (Reps Avg)			
Lesion	Gad Conc (pg/mm^3)	Volume (mm^3)	GFAP_inside	CD31_inside	DAPI_inside	Iba1_inside	GFAP_100un	CD31_100un	DAPI_100um	Iba1_100um	GFAP_50um	CD31_50um	DAPI_50um	Iba1_50um
12	92714.5788	3.8942	0.46431863	1.01534338	0.39739129	0.58003318	0.94344428	1.24834218	0.84130118	1.33337894	0.92819999	1.32170925	0.79301331	1.31549563
16	113740.0996	0.9725	0.44099493	0.60750498	0.29784429	0.45337761	1.05657798	1.03322419	0.98448816	1.2047426	1.04330989	1.04137755	0.94552601	1.2354617
17	110661.7079	2.7031	0.38937866	0.62818661	0.2048617	0.30379374	0.8551767	0.98707081	0.68545834	0.86080886	0.83671356	0.98295539	0.62263874	0.82109026
18	152649.9725	1.6776	0.82669582	1.70259179	0.54788267	0.91609303	0.91692457	1.29233802	0.78997916	1.03453302	0.90555817	1.30880106	0.70567011	1.02616352
19	135598.183	0.5125	1.01641016	2.36726778	1.10923653	1.40645212	1.4206322	1.60233765	1.15720102	1.93994806	1.39806536	1.78651591	1.12710486	2.00208622
20	90145.63991	1.0659	0.49600156	0.44496801	0.26312907	0.45317014	1.05704584	1.02678042	0.96732064	1.16566499	1.04721102	1.0239466	0.89858737	1.13835663
30	78085.07867	0.6213	0.39885241	0.41496721	0.27075706	0.43231426	0.98397994	1.02685786	0.86826289	1.06163354	1.03980435	1.09825813	0.86581851	1.1515327
31	71134.76341	0.1706	0.38462935	0.49633306	0.22619912	0.43015429	1.07708834	0.9729577	1.03793697	1.29016273	1.02532204	0.92479411	0.92802168	1.25638964
32	41019.87042	0.3754	0.6389012	0.45388075	0.36212609	0.68347586	1.18503577	0.84585389	1.28792896	1.39640469	1.17517655	0.86468505	1.16644144	1.3908819
33	141878.8492	0.3832	0.43839389	0.39165771	0.30476375	0.40286051	0.98028225	0.81571769	1.00408845	1.08561283	0.96757882	0.78639576	0.91928778	1.05418382
34	58894.88952	0.894	0.48341992	0.43373104	0.29580202	0.44306105	1.30477273	1.1364358	1.24621049	1.52406022	1.32721962	1.1706922	1.13792745	1.51234684
43	185812.8089	0.424	0.74515852	0.61632318	0.2855843	0.75269869	1.15277551	0.98880473	1.01938653	1.32610403	1.15967395	1.01563284	0.91807499	1.3538739
44	166056.7799	0.442	0.75415504	2.68520111	0.43552906	0.80703634	1.12553339	1.39724704	0.82082223	1.39513438	1.05623473	1.40830901	0.69221363	1.31614934
45	83752.36809	0.1478	0.83629065	1.01151024	0.46652356	0.93781281	0.99701947	0.93919582	0.82031542	1.12239723	0.98945611	0.98743172	0.76259297	1.11489603
46	205300.9457	0.5158	0.50572214	0.5932727	0.16259457	0.44456393	0.86956832	1.00766763	0.55031929	0.89620943	0.86603	1.08794183	0.49567473	0.88856042
47	250453.6696	0.0632	0.77136785	0.58877769	0.24307874	0.77660994	1.02736035	1.08461039	0.75109719	1.10625199	0.97977754	0.86874446	0.53468568	1.06765946
50	173442.2976	0.2495	0.67587646	0.6675078	0.22576538	0.70773858	1.11266199	1.22339701	0.88156548	1.11725933	1.08566037	1.20825458	0.79274544	1.12942283

CHAPTER 4: FOCUSED ULTRASOUND BLOOD-BRAIN BARRIER OPENING ARRESTS THE GROWTH AND FORMATION OF CEREBRAL CAVERNOUS MALFORMATIONS

Delaney G. Fisher, Khadijeh A. Sharifi, Ishaan M. Shah, Catherine M. Gorick, Victoria R. Breza, Anna C. Debski, Matthew R. Hoch, Tanya Cruz, Joshua D. Samuels, John R. Lukens, G. Wilson Miller, Petr Tvrdik, Richard J. Price

4.1 ABSTRACT

BACKGROUND: Cerebral cavernous malformations (CCM) are vascular lesions within the central nervous system, consisting of dilated and hemorrhage-prone capillaries. CCMs can cause debilitating neurological symptoms, yet invasive surgical excision is the only current treatment option. Meanwhile, transient blood-brain barrier opening (BBBO) with focused ultrasound (FUS) and microbubbles (MBs) is now understood to exert potentially beneficial bioeffects, such as stimulation of neurogenesis and clearance of amyloid-β. Here, we tested whether FUS BBBO could be deployed therapeutically to control CCM formation and progression in a clinically-relevant murine model.

METHODS: CCMs were induced in mice by postnatal, endothelial-specific *Krit1* ablation. FUS was applied for BBBO with fixed peak-negative pressures (PNPs; 0.2-0.6 MPa) or passive cavitation detection-modulated PNPs. Magnetic resonance imaging (MRI) was used to target FUS treatments, evaluate safety, and measure longitudinal changes in CCM growth after BBBO.

RESULTS: FUS BBBO elicited gadolinium accumulation primarily at the perilesional boundaries of CCMs, rather than lesion cores. Passive cavitation detection and gadolinium contrast enhancement were comparable in CCM and wild-type mice, indicating that *Krit1* ablation does not confer differential sensitivity to FUS BBBO. Acutely, CCMs exposed to FUS BBBO remained structurally stable, with no signs of hemorrhage induction. Longitudinal MRI revealed that FUS BBBO halted the growth of 94% of CCMs treated in the study. At 1 month, FUS BBBO-treated lesions were, on average, 91% of their pre-sonication volume. In contrast, non-sonicated control lesions grew to 670% of their initial volume. Strikingly, in mice receiving multiple BBBO treatments with fixed PNPs, *de novo* CCM formation was significantly reduced by 81%.

CONCLUSIONS: Our results establish FUS BBBO as a novel, non-invasive modality that can safely arrest CCM growth and prevent their *de novo* formation. As an incisionless, MR image-guided therapy with the ability to target eloquent brain locations, FUS BBBO offers an unparalleled potential to revolutionize the therapeutic experience and enhance the accessibility of treatments for CCM patients.

4.2 INTRODUCTION

Cerebral cavernous malformations (CCM) are vascular lesions originating in the capillary-venous vessels of the central nervous system[1]. These slow flow vascular malformations are hemorrhage prone, grossly enlarged, and lack many of the supporting cells of the neurovascular unit[4,74]. CCMs generally arise due to the biallelic mutation in one of the three CCM-related genes: *Krit1/CCM1*, *MGC4607/CCM2*, and *PDCD10/CCM3*[1,75]. CCM patients can experience debilitating and life-altering symptoms such as motor and visual deficits, seizures, and stroke[76]. These symptoms generally arise from the rapid growth and hemorrhage of a CCM[2]. The current standard of care for CCM is invasive surgical resection. However, surgery is associated with a high risk of post-operative morbidities and limited to surgically accessible CCMs[2]. Due to their eloquent location, CCMs located in the brainstem are associated with even greater risks of early morbidity and recurrent growth following incomplete resection[2,6]. The pathological trajectory of CCMs remains largely uncertain to clinicians[10,12,77]. CCM patients, and parents of children with CCM, are thus put in the position of choosing between risky and invasive neurosurgery or inaction.

As an incisionless therapy with the ability to target eloquent brain locations, focused ultrasound (FUS) may represent an ideal alternative for CCM treatment. With targeting provided by magnetic resonance imaging (MRI), FUS delivers acoustic energy deep within the body to non-invasively produce mechanical or thermal therapeutic effects[78]. When FUS is combined with an intravenous (i.v) injection of gas-filled microbubbles, the oscillating pressure waves induce an alternating expansion and contraction of the gas within microbubbles, which in turn causes the microbubbles to push and pull on the walls of blood vessels. If performed in the brain, this procedure can induce a temporary opening of the blood-brain barrier (BBB). FUS-mediated BBB opening (BBBO) has been developed primarily to enable enhanced delivery of drugs and other therapeutic agents into the brain for various neurological conditions[25,79,80]. However, FUS BBBO

has also been shown to be beneficial in the absence of drug delivery for the treatment of Alzheimer's disease[24,28,30,81–84]. While the exact mechanism(s) behind the beneficial effect of FUS BBBO in Alzheimer's disease are not completely understood, ample preclinical evidence of this effect has led to several clinical trials that are testing this approach in patients with Alzheimer's disease (NCT04118764, NCT04526262, NCT02986932, NCT03739905, NCT04250376).

In this study, we examined the effectiveness and safety profile of FUS BBBO applied to CCMs and its potential to, in the absence of drug delivery, therapeutically control the growth and *de novo* formation of CCMs.

4.3 RESULTS

4.3.1 FUS EFFECTIVELY OPENS THE BBB WITHIN THE CCM MICROENVIRONMENT

Given the altered biomechanical properties[55,85,86] and increased caliber of the vasculature of CCMs and the surrounding, perilesional vasculature (**Figure 4.1A**), we first questioned whether FUS in combination with i.v. microbubble injection could effectively elicit BBBO in CCM mice. We acquired baseline, high resolution T2-weighted spin echo MR images of CCM mice to select CCMs for sonication. On the day of FUS treatment, gadolinium contrast agent (gadobenate dimeglumine; 1.058 kDa) was injected intravenously, and a pre-sonication T1-weighted spin echo MR image was obtained. We next performed FUS BBBO on selected CCMs at peak-negative pressures (PNP) of 0.2 MPa - 0.6 MPa at 0.1 MPa intervals using standard BBBO parameters. Analysis of the T1 contrast enhancement of the post-sonication images compared to the pre-sonication images revealed that FUS BBBO enhanced gadolinium accumulation to the CCM (**Figure 4.1B-C)**. Gadolinium accumulation around CCMs was significantly increased by FUS BBBO over the baseline leakiness of gadolinium for PNPs of 0.3 MPa to 0.6 MPa (**Figure 4.1C**). Examining the pattern of T1 contrast enhancement, we found that gadolinium accumulation was primarily localized to the perilesional boundaries of the sonicated CCM rather than the lesion core (**Figure 4.1B)**. These results indicate that FUS can effectively open the BBB within the CCM microenvironment, despite the enlarged and irregular microvasculature associated with the lesion.

4.3.2 FUS BBBO DOES NOT INCREASE VOLUME OR BLEEDING OF HEMORRHAGE-PRONE CCMS ACUTELY

Due to the propensity of CCMs to hemorrhage and, more broadly, the dysregulated state of the microvasculature in CCM[1], we next sought to evaluate the safety of FUS BBBO in this disease model. To determine if growth or bleeding was acutely induced by FUS BBBO at PNPs

of 0.2 MPa – 0.6 MPa, MR images of the brains of CCM mice were taken 48 h before and 24 h after FUS BBBO. A 3-dimensional, T2-weighted spin echo sequence was employed to accurately capture changes in CCM volume (**Figure 4.2A**), while 3-dimensional, susceptibility-weighted images (SWI) were acquired to capture changes in iron content and fluid flow (i.e. bleeding or hemorrhage; **Figure 4.2C**) with high sensitivity. Measurement of the hypointense lesion margins between pre- and post-sonication images revealed no evidence of acute growth or hemorrhage induced by FUS BBBO (**Figure 4.2B, D**), indicating that FUS BBBO causes neither growth nor bleeding of CCMs at acute time points.

4.3.3 Comparison of FUS BBBO contrast enhancement and acoustic emission signatures between wild-type and CCM mice

To test whether CCM mice differentially respond to BBBO with microbubbles and FUS at PNPs of 0.4 MPa – 0.6 MPa, we compared T1 contrast enhancement and passive cavitation detection (PCD) measurements from wild-type mice to CCM mice. Our analysis revealed no significant differences in T1 contrast enhancement between wild-type and CCM mice at any of the tested PNPs (**Figure 4.3A-B**). Spectrograms were generated of the frequency response for each burst during the FUS application for both wild-type and CCM mice at PNPs of 0.4 MPa – 0.6 MPa (**Figure 4.3C**), and cavitation levels were quantified for the subharmonic, ultraharmonic, broadband, and harmonic spectrums (**Figure 4.3D-E**). Spectral domains associated with a transition towards inertial cavitation of microbubbles (i.e. subharmonic, ultraharmonics)[87,88], or an increase in inertial cavitation of microbubbles (i.e. broadband)[88], increased with PNP and were comparable between wild-type and CCM mice (**Figure 4.3D**). Spectral domains associated with stable cavitation (i.e. harmonics)[88,89] were comparable for PNPs of 0.4 MPa and 0.5 MPa (**Figure 4.3E**). However, at a PNP of 0.6 MPa, CCM mice displayed an increase in harmonic emissions, while the harmonic emissions of wild-type mice remain similar to that observed at lower PNPs (**Figure 4.3E**). Altogether, these results suggest that FUS BBBO affects wild-type and CCM mice

similarly with regards to gadolinium contrast agent delivery and microbubble activity, particularly unstable microbubble activity. Meanwhile, at high PNPs, stable microbubble activity is enhanced in CCM mice, albeit without comparable increases in inertial cavitation.

4.3.4 CCM MICE ARE NOT DIFFERENTIALLY SENSITIVE TO ADVERSE EFFECTS GENERATED BY FUS BBBO AT HIGH PNPS

To assess the longitudinal safety of FUS BBBO in CCM mice, we collected T2-weighted spin echo sequences over a one-month period following FUS BBBO in wild-type and CCM mice (**Figure 4.4A**). FUS BBBO was either performed once (single treatment arm) or was repeated: three times for PNPs of 0.4 MPa or two times for PNPs of 0.5 MPa and 0.6 MPa, with a three-day spacing between sonications (repeat treatment arm). Edema, visible as hyperintensity on T2-weighted MRI, was apparent in lesion-free brain tissue in a fraction of both wild-type and CCM mice one day post FUS BBBO for PNPs of 0.5 MPa and 0.6 MPa (**Figure 4.4A-B**). Hemosiderin deposits, visible as hypointensity on T2-weighted MRI, was also apparent in lesion-free brain tissue in wild-type and CCM mice at time points beyond one day post-FUS BBBO and persisted for at least one month following FUS BBBO for PNPs of 0.5 MPa and 0.6 MPa (**Figure 4.4A, C**). Edema, evident as an increase in the ipsilateral-to-contralateral grayscale ratio, primarily occurred after BBBO with PNPs of 0.5 MPa (**Figure 4.4B**), and hemosiderin deposition, evident as a decrease in the ipsilateral-to-contralateral grayscale ratio, increased as a function on PNP (**Figure 4.4C**). Generally, acute edema was associated with chronic hemosiderin deposition for both models and both treatment arms (**Figure 4.4D**). When comparing the prevalence of edema and hemosiderin deposition between wild-type and CCM mice for each treatment regimen and PNP, no significant differences were seen (**Figure 4.4E**). However, when treatment regimens were aggregated, wild-type mice actually exhibited a greater propensity for edema than CCM mice

(**Figure 4.4B**), yet wild-type and CCM mice shared an equivalent correlation for hemosiderin deposition (**Figure 4.4C**). These results suggest that, while BBBO with PNPs greater than 0.4 MPa are safe for CCMs, FUS BBBO at increased PNPs can induce damage to the surrounding brain tissue, consistent with that seen in wild-type mice.

4.3.5 Real-time PCD-modulation of PNP ensures the safety of sonicated brain tissue without compromising gadolinium delivery

To ensure safety of our FUS BBBO application and examine the effect of more clinically-representative FUS BBBO regimens in CCM mice, we performed FUS BBBO using a real-time PCD feedback control system to modulate the applied PNP during sonication[90–92]. Using this PCD-modulated PNP approach, the maximum applied PNP peaked during the first 15 seconds of sonication, and the PNP generally decreased gradually over the sonication period (**Figure 4.5A**). This approach resulted in a time-averaged PNP ranging from 0.23 MPa – 0.30 MPa and a maximum PNP ranging from 0.25 MPa – 0.38 MP. PCD-modulated PNPs successfully increased T1 contrast in the CCM microenvironment (**Figure 4.5B-C**). Comparing PCD-modulation of PNP to the fixed PNP approach revealed that PCD-modulated PNP resulted in higher T1 contrast enhancement than fixed PNPs of similar amplitudes (**Figure 4.5D**). Acoustic emissions measurements revealed that PCD-modulated PNP elicits comparable subharmonic, broadband, and harmonic spectra when compared to fixed PNPs of 0.4 MPa and 0.5 MPa (**Figure 4.5E-F**). Longitudinal T2-weighted MRI also demonstrated that PCD-modulated PNP obviates edema and hemosiderin deposition following FUS BBBO (**Figure 4.5G-H**). For BBBO in CCM mice, edema was comparable across PNPs and a reduction of hemosiderin deposition was seen with PNPs averaging less than or equal to 0.4 MPa (**Figure 4.5I**). Altogether, these data indicate that PCD-modulation of PNP ensures the safety of FUS BBBO in CCM brain tissue and elicits enhanced gadolinium delivery compared to fixed PNPs.

4.3.6 FUS BBBO ARRESTS CCM GROWTH

We then asked if FUS BBBO stimulates therapeutically beneficial CCM responses. CCM mice were placed in (i) a single FUS BBBO regimen with fixed PNP (i.e. one FUS BBBO treatment at either 0.4 MPa or 0.5 MPa), (ii) a repeat FUS BBBO regimen with fixed PNP (i.e. three FUS BBBO treatments at 0.4 MPa or two FUS BBBO treatments at 0.5 MPa or 0.6 MPa, all staged three days apart), or (iii) a repeat FUS BBBO regimen with PCD-modulated PNP (i.e. two FUS BBBO treatments staged three days apart). Mice were treated between 2 and 3 months of age during a period of optimal lesion burden in our mouse model as assessed previously by our group[93]. Male and female mice across 9 litters were used in this study as detailed in **Table S1**. MR images were acquired following each sonication and up to one month following sonication (**Figure 4.6A, C, E**). Sonicated CCM volumes were measured in MR images taken prior to FUS, as well as in MR images taken 1 day, 1 week, and 1 month following FUS. These volumes were compared to non-sonicated CCMs of similar baseline size and anatomical location within the same cohort of mice at the same imaging timepoints. The average sonicated and non-sonicated (contralateral control) CCM volume prior to FUS application was 0.039 mm^3 for both conditions. Remarkably, CCMs exposed to FUS BBBO in all treatment regimens exhibited nearly a complete cessation of growth (**Figure 4.6B, D, F**). Only 3 of 47 CCMs exposed to FUS BBBO grew more than 0.02 mm^3 in 1 month, while to 26 of 41 CCMs not exposed to FUS BBBO grew this amount in the same period. Significant differences in lesion volume between the sonicated and non-sonicated CCMs were seen at the 30 day time point for all treatment arms (**Figure 4.6B, D,** linear mixed effects model: **Table 4.S2).** At 7 days, sonicated CCMs were significantly smaller than non-sonicated CCMs in the repeat FUS and fixed PNP arm (**Figure 4.6D**). At 1 month post-FUS, sonicated CCMs in all treatment arms demonstrated a markedly reduced mean lesion volume, reaching just 28%, 10%, and 26% of the mean volume of the non-sonicated CCM volume in the

single, fixed PNP; repeat, fixed PNP; and repeat, PCD-modulated PNP arms, respectively. Increases in PNP and number of FUS BBBO treatments were both inversely correlated with increased lesion volume (**Figure 4.S1A-B, E**). The effect of sex on CCM volume and FUS BBBO was also evaluated (**Figure 4.S2A-B**). At 1 month, CCMs in male mice were larger than those in female mice, regardless of FUS BBBO treatment (**Figure 4.S2A, Table 4.S2**). Sex did not significantly alter the ability of FUS BBBO to control CCM growth (**Figure 4.S2A, Table 4.S2**).

4.3.7 FUS BBBO WITH FIXED PNP AND REPEAT SONICATIONS CAN PREVENT DE NOVO LESION FORMATION

To then ascertain if FUS BBBO impacts the formation of new lesions, we counted the number of lesions contained within the focal zone (i.e. T1-contrast-enhanced brain region) in MR images taken prior to FUS BBBO, as well as one month following FUS BBBO. The same analysis was performed in the contralateral hemisphere of each mouse using the same volume and mirrored anatomical location (**Figure 4.7A, C, E**). The change in the number of lesions from the pre-image to the one-month post-FUS BBBO image was compared for the sonicated and contralateral brain areas within each mouse. This analysis revealed that the repeat FUS regimen with fixed PNP significantly reduced the formation of new CCMs by 81% compared to the contralateral brain region (**Figure 4.7D**). Meanwhile, the single FUS with fixed PNP regimen and repeat FUS with PCD-modulated PNP regimen displayed trends toward reduced *de novo* CCM formation (**Figure 4.7B, F**). Importantly, in all treatment arms, FUS BBBO did *not* induce an increase in lesion formation. In fact, both the single and repeat FUS with fixed PNP cohorts contained one mouse that displayed a fewer number of lesions in the sonicated brain region one month following FUS BBBO compared to the pre-image, suggesting that some CCMs may be cleared with FUS BBBO. Increases in PNP were found to be significantly, inversely correlated

with *de novo* lesion formation, while the number of sonication treatments followed this trend, albeit not significantly (**Figure 4.S1C-E**). The effect of sex on *de novo* CCMs and FUS BBBO was also evaluated (**Figure 4.S2C-D**). Sex did not significantly alter the ability of FUS BBBO to control CCM formation (**Figure 4.S2C, Table 4.S2**).

4.4 DISCUSSION

Patients with CCM can sustain incapacitating and even life-threatening neurological symptoms. The only treatment option for these patients currently is resection of symptomatic CCMs via invasive neurosurgery, which is associated with a high risk of postoperative morbidities and limited to CCMs that are surgically accessible[2,94,95]. Concurrently, FUS BBBO is a non-invasive approach that can exert potentially favorable bioeffects, such as enhanced clearance of pathology-enabling molecular species and delivery of beneficial plasma-circulating factors[24,25]. Here, we demonstrate that FUS BBBO can exert powerful therapeutic effects in a clinically-representative murine model of CCM. Notably, FUS BBBO arrested the growth of 94% of CCMs treated in the study over a 1 month period. Meanwhile, untreated CCMs increased by ~7-fold of their initial volume on average across the 3 treatment arms in this same timeframe. Further, mice that received multiple FUS BBBO treatments with fixed PNPs had a significant reduction in the formation of *de-novo* CCMs by 81%. As an incisionless therapy with the ability to target eloquent brain locations, FUS BBBO is a disruptive technology that could radically transform how CCMs are treated.

4.4.1 CHARACTERISTICS OF FUS BBBO IN CCM MICE

One key consideration in these studies was whether FUS BBBO signatures in *Krit1* mutant mice differ from those in wild-type mice. Since the vasculature associated with CCMs is known to be irregular and dilated[74,96], the effectiveness of FUS BBBO had the potential to be reduced or otherwise altered. Increased vessel diameters could reduce the interaction between the oscillating microbubbles and vessel walls[97,98]. Moreover, the slow flow rate in the lesion core could reduce the number of microbubbles accumulating within the CCM[96]. Our studies indicate that the pattern of T1 contrast enhancement is localized to the perilesional boundaries of the CCM (**Figure 4.1B**), which may indicate that the lesion core is not substantially interacting with microbubbles, perhaps due to its grossly enlarged diameter or its slow flow rate. Meanwhile, the perilesional

microvasculature displayed marked gadolinium accumulation regardless of moderate vessel diameter dilation compared to normal brain capillaries (**Figure 4.1D**). Further, our findings suggest that T1 contrast enhancement as well as subharmonic, ultraharmonic, and broadband acoustic signatures of microbubble activity are not significantly different between CCM mice and wild-type mice (**Figure 4.3**). While the harmonic signatures for PNPs of 0.4 MPa and 0.5 MPa were not significantly different between CCM and wild-type mice, increases in harmonic signatures were seen in CCM mice at 0.6 MPa (**Figure 4.3E**). This is the only indication that the altered properties of the CCM vasculature, such as vessel diameter, stiffness, and contractility[55,85,86], can impact microbubble activity when high enough PNPs are applied. Additionally, since CCMs have a baseline leakiness, it was possible that FUS BBBO would not increase the accumulation of small molecules within the lesion microenvironment. Nevertheless, T1 contrast enhancement from the post-FUS image over the pre-FUS image is indeed apparent for PNPs ranging from 0.3 MPa – 0.6 MPa (**Figure 1D**), indicating that gadolinium accumulation is increased over baseline levels via FUS BBBO. Ultimately, while the pattern of T1 contrast enhancement may be altered in CCM mice, FUS still effectively opens the BBB in the perilesional vasculature of the lesion, and the MRI and acoustic signatures are largely comparable to wild-type mice.

4.4.2 Acute stability of CCMs exposed to FUS BBBO

The capricious state of these hemorrhage-prone CCMs raised an important concern: would BBBO increase the propensity of CCMs to bleed? The addition of mechanical stress and disruption of already loose endothelial cell tight junctions from oscillating microbubbles had the potential to weaken the stability of CCMs. However, our findings clearly show that FUS BBBO is safe for CCMs. Even susceptibility-weighted images, which have an increased sensitivity to hemorrhage and blood products, demonstrated no acute changes in bleeding between the pre- and post-sonication images (**Figure 4.2D, E**). T2-weighted spin echo sequences, which can

accurately represent lesion volume and internal architecture, displayed no acute changes in lesion volume between the pre- and post-sonication images (**Figure 4.2B,C**)[93]. These results also continued for post-sonication images at later timepoints of up to one month, indicating that FUS BBBO is safe for CCMs both acutely and chronically. Meanwhile, our results did indicate that edema and hemosiderin deposits can be seen in lesion-free brain tissue in *both* wild-type and CCM mice when using PNPs greater than 0.4 MPa (**Figure 4.4**). This finding further supports the use of PCD-modulated PNP feedback systems that have been widely adopted in the field and is used in clinical trials to ensure the safety of FUS BBBO treatments (**Figure 4.5**)[87,89–92,99].

4.4.3 FUS BBBO PROVIDES A THERAPEUTIC EFFECT FOR CCMS AND FAMILIAL FORMS OF THE DISEASE

After establishing that FUS BBBO was safe, we questioned whether it could be therapeutic for CCMs. From analysis of longitudinal MR images, we show that FUS BBBO is capable of both fully arresting the growth of pre-existing CCMs (**Figure 4.6**) and preventing *de novo* CCM formation (**Figure 4.7**). The ability to slow and even reverse the growth of CCMs could have far-reaching implications for CCM therapy. The pathological trajectory of many CCMs remains uncertain to clinicians[10,12,77], so patients must choose between invasive, risky neurosurgery or inaction. FUS BBBO could provide a non-invasive alternative to enable the stabilization of the lesion without the risks associated with surgery or the lack of intervention.

Further, this approach could be revolutionary for patients with the familial form of the disease. Familial CCM patients have multiple lesions, of which several can often arise in locations that are inoperable or are associated with a very high risk for post-operative morbidities[2,10]. FUS BBBO could be used to stabilize multiple CCMs within a single treatment session, including those in eloquent locations, while simultaneously protecting those sonicated areas from future CCMs.

FUS BBBO could help make an impossible choice for CCM patients or parents of CCM patients more manageable.

4.4.4 Possible mechanisms for the protective effect of FUS BBBO in CCM

The ability of FUS BBBO to exert powerful therapeutic effects for CCMs was surprising; however, this is not the first disease indication where FUS BBBO has been shown to be protective. FUS BBBO—in the absence of drug delivery—has also exhibited a therapeutic effect for Alzheimer's disease[24,28,30,81–84]. The exact mechanism of action in Alzheimer's disease remains unclear, though many studies have investigated the potential mechanisms behind its benefit[28,82–84,100]. Some of these potential mechanisms include enhanced clearance (of amyloid-β plaque), increased activation of microglia and/or macrophages, and leakage of plasma-based growth and signaling factors[24,25]. It is unknown if the mechanism(s) behind the protective role in Alzheimer's disease are the same for CCM. Clearance of blood products from the hemosiderin rim and CCM could reduce apparent lesion volume, as well as have the potential to reduce inflammation and neurotoxicity near the lesion. Activation of microglia and macrophages could increase phagocytosis and compaction of blood products, again potentially reducing the apparent lesion volume and reducing neurotoxicity. Leakage of plasma-based growth and signaling factors could have a wide range of effects for the CCM, but it is feasible that some number of plasma-based factors would be protective for the CCM. Indeed, several plasma-circulating factors are capable of modulating CCM pathology[1]. An additional mechanism that may be unique to CCM is downstream effects elicited by microbubble-induced mechanical stresses on the vasculature. In fact, shear stress and fluid flow play a role in CCM development[96]. The *Krit1* mutation of CCM has been shown to diminish endothelial cell response to shear stress[55,69], and blood flow has been shown to suppress vascular malformations in a *Krit1* zebrafish model of CCM[101]. Ultimately, several potential mechanisms may underlie the protective role of FUS BBBO for CCM.

4.4.5 The potential of FUS BBBO to synergize with pharmacological treatments

To date, no pharmacological agent has been approved for the treatment of CCM, yet a few drugs have entered clinical trials (propranolol: NCT03589014, REC-994: NCT05085561, simvastatin: NCT01764451, and atorvastatin: NCT02603328). Additionally, many drugs for CCM are being examined in the preclinical stage[1]. These drug candidates have the potential to seamlessly integrate with the FUS BBBO approach used in this study. Therapeutic agents can be injected alongside FUS BBBO and benefit from the enhanced permeability as a way to shift the systemic dose to be more localized to the CCM. This would be reflected as an increase in the therapeutic index, which could be leveraged to reduce the amount of drug needed and help mitigate potential drug side effects. Moreover, FUS BBBO could also have the potential to unlock whole new classes of drug candidates. Larger molecular weight biologics, like antibodies and gene therapies, would have a greater potential to accumulate in the CCM microenvironment with the aid of increased permeability via FUS BBBO[25,79]. Indeed, the vast majority of the drug candidates being studied for CCM currently are small molecules[1]. Ultimately, the innate protective effect of FUS BBBO for CCM and the countless drug candidates that could integrate with the enhanced delivery of this approach provides an immeasurable potential to vastly expand the therapeutic options and to transform the treatment paradigm for CCM.

4.5 Materials and Methods

4.5.1 Animals

All animal experiments were approved by the University of Virginia Animal Care and Use Committee. The animals were housed under standard laboratory conditions (22°C and 12h/12h light/dark cycle). The generation of the CCM murine models (*Pdgfb-CreERT2;Krit1*$^{fl/null}$ or *Cdh5-CreERT2;Krit1*$^{fl/null}$) that were used in these studies has been described previously[93]. Briefly, *Pdgfb-CreERT2* or *Cdh5-CreERT2* mice were crossed with *Krit1*$^{fl/null}$ male or females. On postnatal day 5, *Krit1* gene ablation was induced with an injection of tamoxifen (subcutaneous; 50uL at 2mg/mL in corn oil). Genotypes were confirmed using Transnetyx (Cordova, TN). Wild-type mice in this study were on the same background strain as the CCM model (C57BL/6; Charles River). All mice were treated between 9 weeks and 13 weeks of age. Mouse sex, litter, age, and treatment assignment are listed in detail in **Table 4.S1**.

4.5.2 MR Imaging

MR imaging was performed using either a 7T Bruker/Siemens ClinScan or a 9.4T Bruker BioSpec small animal MRI scanner. T2-weighted spin echo images were acquired at 7T with the Siemens 3D T2-SPACE sequence (repetition time of 3000 ms, echo time of 80 ms, pixel size of 125 μm x 125 μm x 100 μm, 2 averages, and 20 min acquisition time) or at 9.4T with the Bruker 3D T2-TurboRARE sequence (repetition time of 2000 ms, echo time of 55 ms, pixel size of 125 μm x 125 μm x 125 μm, 1 average, and 30 min acquisition time). Susceptibility-weighted images were acquired at 7T with the swi3d1r sequence (repetition time of 18 ms, echo time of 10 ms, pixel size of 130 μm x 130 μm x 130 μm, 2 averages, and 15 min acquisition time). T1-weighted spin echo images were acquired at 9.4T with the Bruker 2D T1-RARE sequence (repetition time of 1500 ms, echo time of 6 ms, pixel size of 156 μm x 156 μm x 350 μm, 1 average, and 3 min

acquisition time). All imaging was performed under isoflurane anesthesia, and body temperature was maintained with a heated, circulating water bed.

4.5.3 Selection of CCMs for Sonication

Following baseline MR image acquisition, images were reviewed to assess appropriate CCMs for sonication. CCMs located within the left or right caudoputamen, corpus callosum, or cerebral cortex were eligible for targeting. The average sonicated and non-sonicated (contralateral control) CCM volume prior to FUS application was 0.039 mm^3 for both conditions in the longitudinal studies. Prior to safety evaluation measurements and analysis, sonications were confined to single CCMs without neighboring CCMs located dorsally or ventrally that would be within the focal zone. Following the initial safety evaluation, multiple CCMs were eligible for sonication if they were within the same focal volume.

4.5.4 FUS BBBO

FUS BBBO was performed with the RK-300 small bore FUS device (FUS Instruments, Toronto, CA). Heads of mice were shaved and depilated prior to supine placement and coupling to the transducer with degassed ultrasound gel. BBBO was performed with a 1.13 MHz single-element transducer using a 10 ms burst length over a 2000 ms period for 60 total sonications during a 2-min sonication duration. Fixed PNP application was performed using the “Burst” mode on the FUS Instruments software. PCD-modulated PNP was performed using the “Blood-brain Barrier” mode of the FUS Instruments software. Parameters used for this feedback control system included a starting pressure of 0.2 MPa, pressure increment of 0.05 MPa, maximum pressure of 0.4 MPa, 20 sonication baselines without microbubbles, AUC bandwidth of 500 Hz, AUC threshold of 10 standard deviations, pressure drop of 0.95, and frequency selection of the subharmonic, first ultraharmonic, and second ultraharmonic. Gadolinium contrast agent (Multihance) was injected as a bolus intravenously with a dose of 0.01 mmol diluted in saline at a

molarity of 0.2 mmol/mL prior to T1-RARE image acquisition. Albumin-shelled microbubbles were made in-house as previously described[102] and intravenously injected as a bolus dose of 10^5 microbubbles per gram body weight. Distribution of microbubble diameter and concentration was acquired with a Coulter counter (Multisizer 3; Beckman Coulter, Fullerton, California) prior to sonication. High resolution T2-weighted images and T1-RARE images were used to guide FUS targeting to the pre-selected CCM. A single sonication target was used in all experiments, except in the case of PCD-modulated PNPs, in which two sonication targets were used. Mice receiving the repeat FUS BBBO regimens had all sonications staged 3 days apart with the same anatomical location targeted each time.

4.5.5 Acoustic Signatures from Passive Cavitation Detection

Acoustic emissions were detected with a fiber-optic hydrophone (Precision Acoustics, Dorset, UK) of 10 mm diameter and 15 mm aperture center-mounted within the ultrasound transducer. Emissions data was processed and spectrograms were generated with a custom MATLAB script. The area under the curve of the acoustic emissions at the subharmonic (0.5f) and ultra-harmonics (1.5f, 2.5f) were calculated after applying a 300 Hz bandwidth filter. Broadband emissions were evaluated by summing acoustic emissions following the removal of all emissions at the fundamental frequency (f), harmonics (2f, 3f, 4f), subharmonic (0.5f), and ultra-harmonics (1.5f, 2.5f, 3.5f).

4.5.6 T1 Contrast Enhancement Analysis

Gadolinium accumulation following FUS BBBO was evaluated using the enhancement of T1 contrast in T1-RARE images. In a DICOM viewer (Horos Project, Geneva, Switzerland), an ROI was drawn around the T1 enhanced contrast boundaries on the image slice containing the targeted lesion. The ROI was then copied onto the pre-sonication T1-RARE image on the same slice. For wild-type mice, ROIs were drawn around the T1 contrast boundaries in similar

ventral/dorsal slice depths as CCM mice. Mean grayscale intensity for each ROI was recorded, and fold change in grayscale intensity from the post-image to the pre-image was calculated. This process was repeated for all sonicated mice across each PNP.

4.5.7 Brain Tissue Edema and Hemosiderin Deposition Analysis

Damage to lesion-free brain tissue following FUS BBBO was evaluated in 3D Slicer using the high resolution T2-weighted spin echo MR images. MR images were initially segmented by the brain tissue boundaries to generate a mask of the brain. Bias field correction was then applied with the N4ITK MRI Bias Field Correction tool in 3D Slicer to correct for inhomogeneities in signal intensity across the brain due to mouse rotation relative to the MR surface coil. Mean grayscale intensity was then recorded within ROIs of equal volume in lesion-free brain tissue for both non-sonicated (contralateral) and sonicated (ipsilateral) hemispheres on the same dorsal slice. Healthy brain tissue would have an ipsilateral-to-contralateral grayscale ratio near 1. Edema would produce a ratio greater than 1, while hemosiderin would produce a ratio less than 1.

4.5.8 CCM Growth Analysis

CCM volume prior to, and longitudinally following, FUS BBBO was evaluated in Horos using the high resolution T2-weighted spin echo MR images. For each timepoint, an ROI was manually drawn around the sonicated CCM in each slice it was present. The Horos “Compute Volume” tool was then used to calculate the three-dimensional volume of the CCM across imaging timepoints. In the same mice, ROIs were also drawn around non-sonicated CCMs (i.e. control CCMs) that had similar volumes and anatomical locations as sonicated lesions. CCM mice with enlarged ventricles at the one-month timepoint were removed from this analysis.

4.5.9 New Lesion Formation Analysis

Formation of new CCMs was assessed by calculating the change in lesion number from the baseline pre-FUS to the one-month post-FUS high resolution T2-weighted spin echo MR

images. For both timepoints, an ROI was first drawn around the T1 contrast enhanced boundaries within the T1-RARE images taken following FUS BBBO, extending from the most dorsal to most ventral slices of the brain and focal column. These ROIs were then copied onto the T2-weighted spin echo images and adjusted to match the same anatomical positioning. These ROIs were then copied to the contralateral brain region and adjusted to mirror the same anatomical positioning. CCMs within the ROIs were then manually counted and recorded for both timepoints and for both the ipsilateral ROI and the contralateral ROI. The baseline CCM number was subtracted from the one-month CCM number for both the ipsilateral ROI volume and the contralateral ROI volume in each mouse to produce the number of new CCMs formed in each ROI volume during the one-month time period. CCM mice with enlarged ventricles at the one-month timepoint were removed from this analysis.

4.5.10 Immunohistochemistry

Mice were perfused with phosphate-buffered saline (PBS) and 4% paraformaldehyde, and after harvesting, brains were fixed overnight in 4% paraformaldehyde and dehydrated in 30% sucrose solution for 24 h. Brains were then embedded in Optimal Cutting Temperature Compound (TissueTek) for cryosectioning at 30-µm thickness. Sections were incubated in blocking solution (1% bovine serum albumin, 2% normal donkey serum, and 0.1% Triton X-100, and 0.05% Tween-20 in PBS) for 2 h at RT. Brain sections were then incubated with goat anti-CD31 (1:20, R&D Systems, AF3628) diluted in the blocking solution overnight at 4°C. After three 5-min washes in PBS with 0.5% Tween-20, the sections were incubated with donkey anti-goat Alexa 647 (1:500, Invitrogen A21447) and diluted in the blocking solution for 2 h at RT. Sections were imaged with a Leica Stellaris 5 confocal microscope (Leica Microsystems). Images were processed with Fiji/ImageJ.

4.5.11 Statistical Analysis

All results are reported as mean ± standard error of the mean (SEM). The “n” values per group are made evident either by individual data points shown or statement of “n” value in figure, figure legend, and/or manuscript text. Statistical significance was assessed at $p < 0.05$ for all experiments. Linear mixed effect models were conducted and analyzed with the lme4 package (version 1.1.34) and the emmeans package (version 1.8.9) in R Studio. All other statistical tests were performed using GraphPad Prism 9 (San Diego, USA). Statistical tests, models, and p-values are listed in detail for all manuscript figures in **Table 4.S2**.

4.6 CHAPTER 4 FIGURES

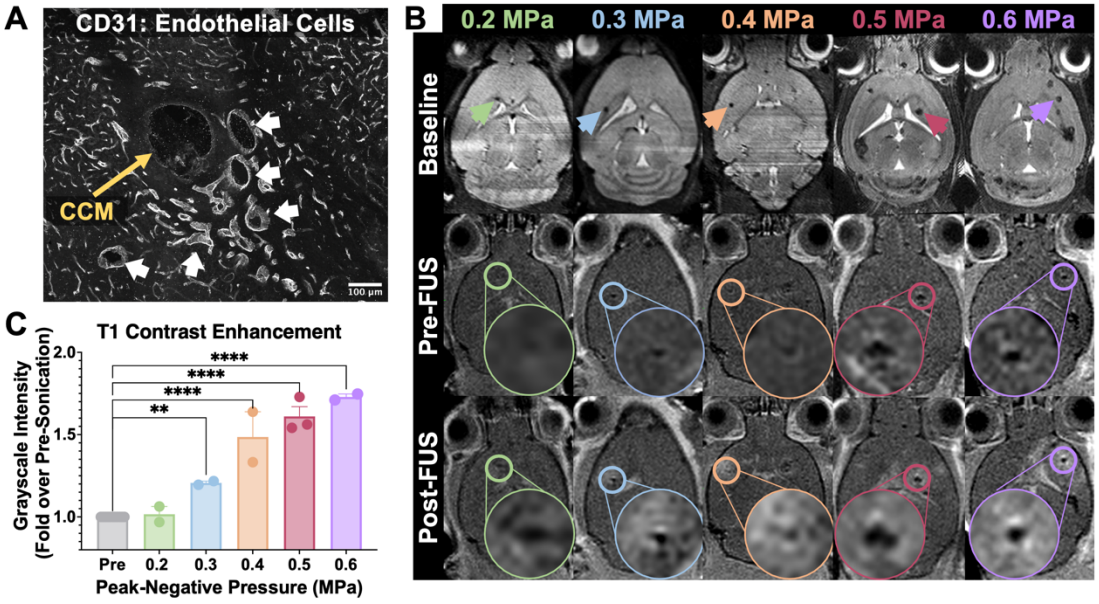

Figure 4.1. FUS effectively opens the BBB within the CCM microenvironment. (A) Confocal image of a CCM (in the absence of FUS) stained with CD31 for endothelial cells. Image depicts the grossly enlarged CCM core (yellow arrow), and moderately dilated perilesional vasculature (white arrows). Scale bar = 100 μm. (B) Top row: Baseline, high-resolution T2-weighted spin echo images used for selecting CCMs for FUS targeting. Arrowheads indicate selected CCMs. Middle row: T1-weighted spin echo images acquired following gadolinium contrast agent injection but immediately prior to FUS application. Circles indicate targeted CCMs, and insets display magnified views of the targeted CCMs. Bottom row: T1-weighted spin echo images acquired following gadolinium contrast agent injection and FUS application. Columns indicate PNPs used for sonication. T1 contrast enhancement is visible following FUS BBBO and localized to perilesional boundaries of the sonicated CCM. (C) Bar graph of T1 contrast enhancement quantified as the fold change in grayscale intensity of sonicated CCMs in the post-image over the pre-image (as seen in A). Gadolinium accumulation following FUS BBBO over the baseline CCM leakiness for PNPs of 0.3 MPa to 0.6 MPa. One-way ANOVA followed by Dunnett's multiple comparisons test, $p=0.054$ for 0.3 MPa and $p<0.0001$ for 0.4 MPa – 0.6 MPa.

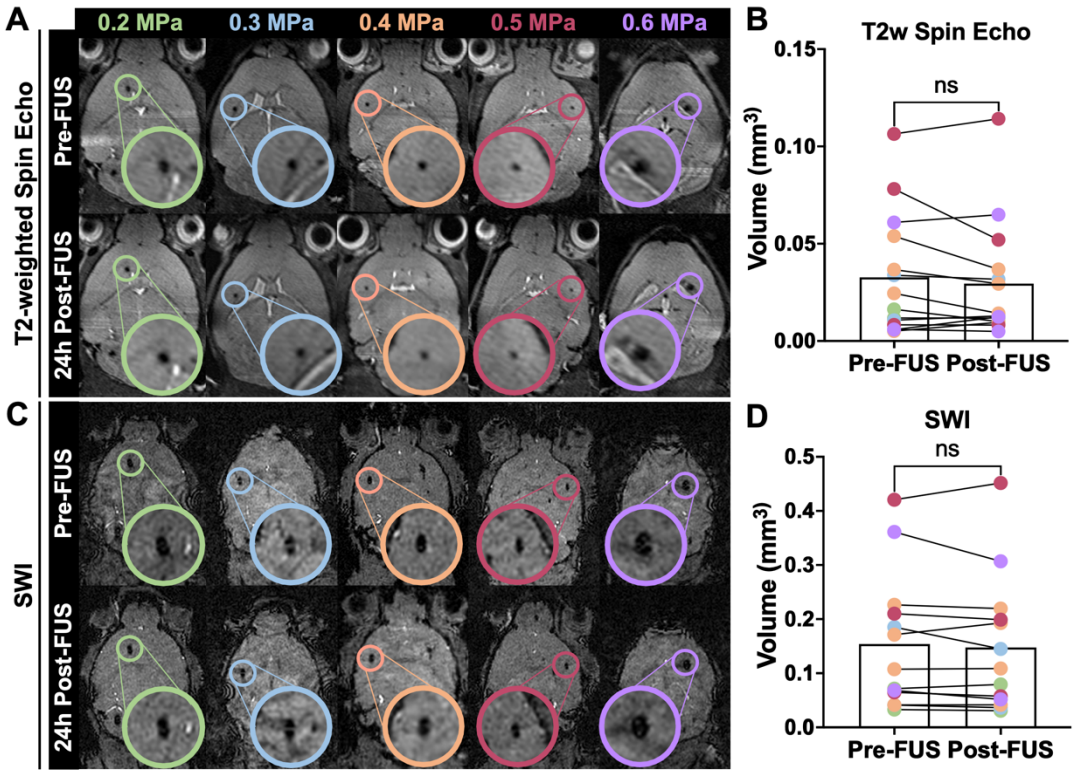

Figure 4.2. Acute stability of CCMs exposed to FUS BBBO. (A) High-resolution T2-weighted spin echo images displaying either CCMs prior to sonication (top row) or 24 h following sonication (bottom row). Circles denote targeted CCMs, and insets display magnified views of the targeted CCMs. (B) Targeted CCM volumes prior to sonication and 24 h following sonication on T2-weighted spin echo images with color indicating applied PNP. CCM volume does not significantly demonstrate changes in volume following sonication. Wilcoxon matched-pairs signed rank test, p=0.4143. (C) High-resolution susceptibility-weighted images of the same mice in A, displaying either CCMs prior to sonication (top row) or 24 h following sonication (bottom row). (D) Targeted CCM volumes prior to sonication and 24 h following sonication on susceptibility-weighted images with color indicating applied PNP. CCM volume does not significantly demonstrate changes in bleeding following sonication. Wilcoxon matched-pairs signed rank test, p=0.3396.

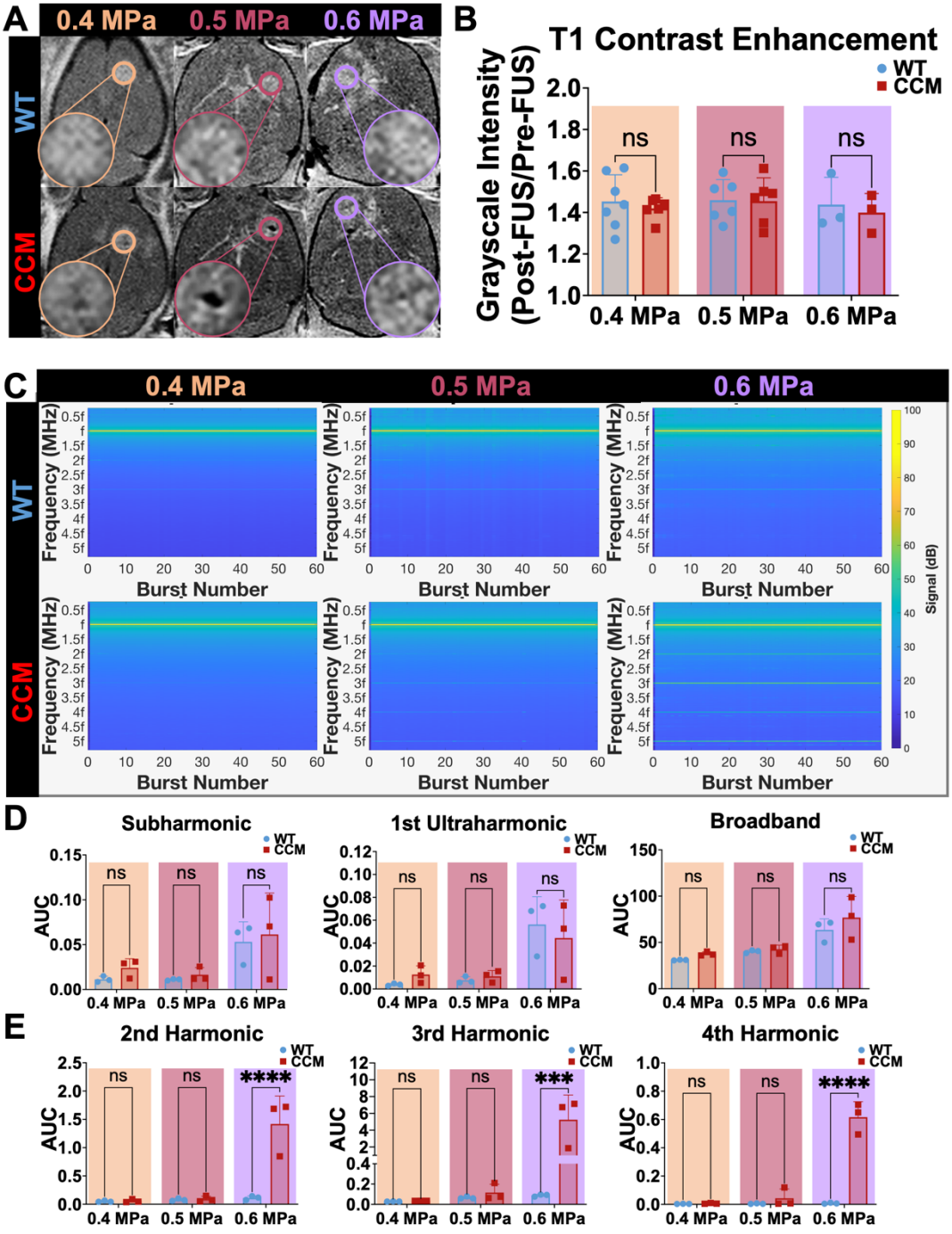
A
0.4 MPa
0.5 MPa
0.6 MPa
WT
CCM
B
T1 Contrast Enhancement
WT
CCM
Grayscale Intensity (Post-FUS/Pre-FUS)
2.0
1.8
1.6
1.4
1.2
1.0
ns
ns
ns
0.4 MPa
0.5 MPa
0.6 MPa
C
0.4 MPa
0.5 MPa
0.6 MPa
WT
CCM
Frequency (MHz)
0.5f
f
1.5f
2f
2.5f
3f
3.5f
4f
4.5f
5f
0
10
20
30
40
50
60
Burst Number
Signal (dB)
100
90
80
70
60
50
40
30
20
10
0
D
Subharmonic
1st Ultraharmonic
Broadband
WT
CCM
AUC
ns
0.4 MPa
0.5 MPa
0.6 MPa
E
2nd Harmonic
3rd Harmonic
4th Harmonic
****
***

Figure 4.3. Comparison of FUS BBBO contrast enhancement and acoustic emission signatures between wild-type and CCM mice. (A) Representative T1-weighted spin echo images acquired following gadolinium contrast agent injection and FUS application in wild-type mice or CCM mice from PNPs of 0.4 MPa – 0.6 MPa. (B) Bar graph of T1 contrast enhancement quantified as the fold change in grayscale intensity of sonicated area in the post-image over the pre-image. Enhancement is comparable in wild-type and CCM mice for PNPs of 0.4 MPa- 0.6 MPa. Two-way ANOVA with Šidák's multiple comparison test, $p=0.9238$ for 0.4 MPa, $p=0.9998$ for 0.5 MPa, and $p=0.9590$ for 0.6 MPa. (C) Spectrograms of the frequency response for each burst during the FUS application averaged over cohorts of wild-type and CCM mice at PNPs of 0.4 MPa – 0.6 MPa (n=3 mice per group and 2-3 sonication replicates per mouse). (D) Subharmonic, first ultraharmonic, and broadband emissions for wild-type and CCM mice at PNPs of 0.4 MPa – 0.6 MPa, indicating comparable inertial cavitation-associated signatures between wild-type and CCM mice. Two-way ANOVA with Šidák's multiple comparisons test, $p>0.4$ for all PNPs. (E) Second, third, and fourth harmonic emissions for wild-type and CCM mice at PNPs of 0.4 MPa – 0.6 MPa, indicating that stable cavitation-associated signatures between wild-type and CCM mice are comparable at 0.4 MPa and 0.5 MPa but not are significantly increased in CCM mice at 0.6 MPa. Two-way ANOVA with Šidák's multiple comparisons test; $p>0.7$ for 0.4 – 0.5 MPa and 2nd – 4th harmonics; $p<0.0001$, $p=0.0006$, $p<0.0001$ for 0.6 MPa and 2nd, 3rd, and 4th harmonics, respectively.

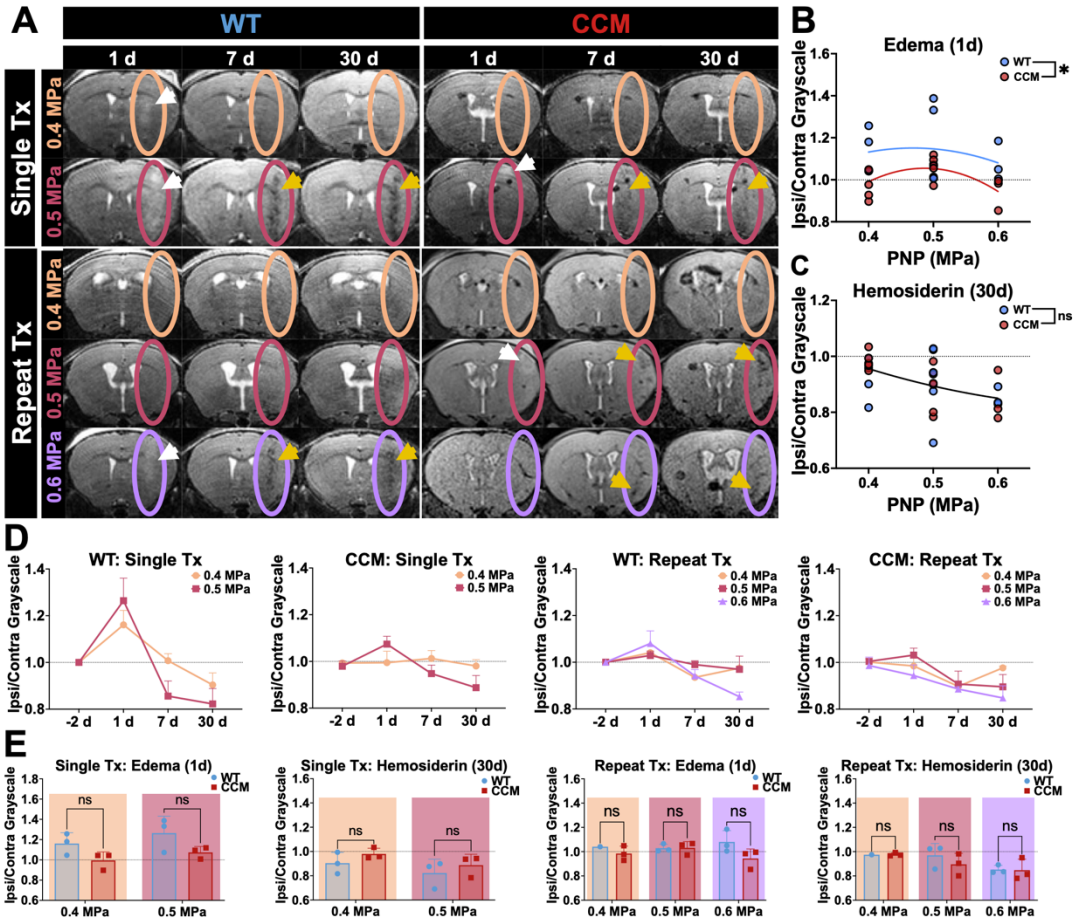

Figure 4.4. CCM mice are not differentially sensitive to adverse effects generated by FUS BBBO at high PNPs. (A) Representative high resolution, T2-weighted spin echo images of wild-type and CCM mice at 1 d, 7 d, and 30 d post sonication at PNPs of 0.4 MPa – 0.6 MPa in either a single sonication or repeat sonication treatment regimen. Ovals denote focal column. White arrows denote hyperintensities associated with edema. Yellow arrows denote hypointensities associated with hemosiderin deposition. (B) Scatterplot of ipsilateral-to-contralateral grayscale intensity on 1d post FUS (when edema is visible) of wild-type and CCM mice for PNPs of 0.4 MPa – 0.6 MPa. Comparison of fits with F-test for a 2nd order polynomial regression indicates that edema signatures in wild-type and CCM differ, p=0.0473. (C) Scatterplot of ipsilateral-to-contralateral grayscale intensity on 30d post FUS (when hemosiderin is visible) of wild-type and CCM mice for PNPs of 0.4 MPa – 0.6 MPa. Comparison of fits with F-test for a 2nd order polynomial regression indicates that hemosiderin signatures in wild-type and CCM are comparable, p=0.7734. (D) Line graphs of ipsilateral-to-contralateral grayscale intensities over the one-month imaging period for all PNPs within a mouse model and treatment arm, revealing that edema on day 1 is generally followed by hemosiderin on days 7 and 30. (E) Ipsilateral-to-contralateral grayscale intensities over the one-month imaging period for all PNPs within a mouse model and treatment arm, indicating no significant differences when comparing models at individual PNPs within a treatment arm. Two-way ANOVA with Holm-Šidák's multiple comparisons test; p=0.1368 and p=0.5386 for

both PNPs in the single treatment arm for edema and hemosiderin, respectively; $p>0.7$ for PNPs of 0.4 MPa and 0.5 MPa and $p=0.0923$ for PNP of 0.6 MPa in the repeat treatment arm for edema; $p>0.5$ for all PNPs in the repeat treatment arm for hemosiderin.

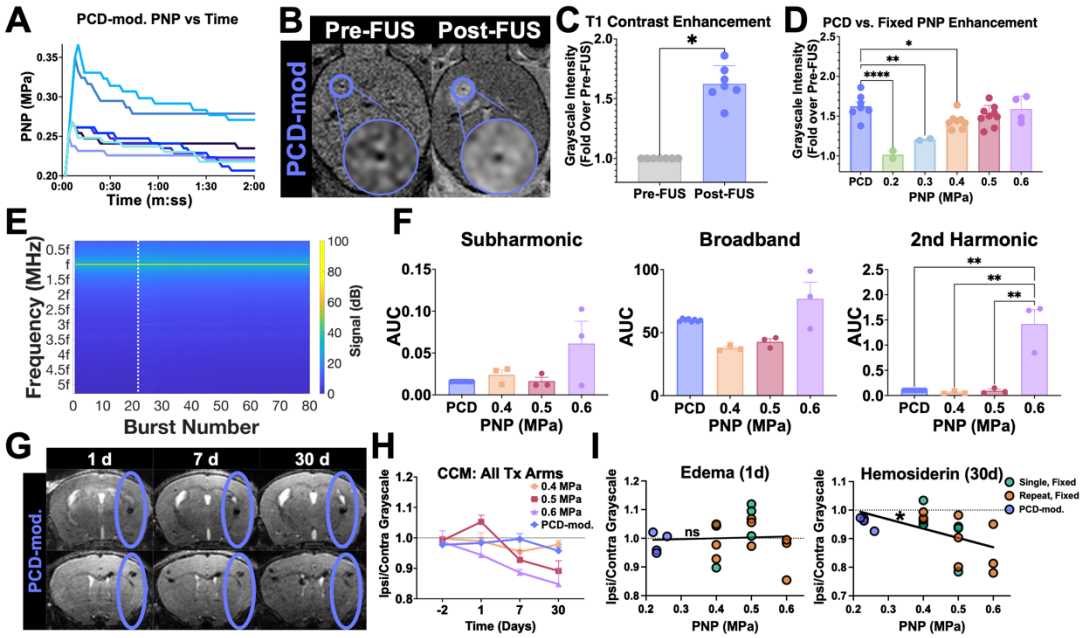

Figure 4.5. Real-time PCD-modulation of PNP ensures the safety of sonicated brain tissue without compromising gadolinium delivery. (A) Applied PNP versus time during PCD feedback-controlled approach. Each line indicates the average applied PNP across two sonication targets for the same mouse during a single FUS sonication period. (B) Representative T1-weighted contrast images before and after FUS BBBO with PCD-modulated PNPs. (C) Bar graph of T1 contrast enhancement quantified as the fold change in grayscale intensity of sonicated CCMs in the post-image over the pre-image (as seen in B), indicating successful BBBO. Wilcoxon matched-pairs signed rank test, p=0.0156. (D) Bar graph of T1 contrast enhancement quantified as the fold change in grayscale intensity of sonicated CCMs in the post-image over the pre-image for CCM mice with fixed PNP and PCD-modulated PNP cohorts. Graphs reveals that T1 contrast enhancement is greater with PCD-modulated PNP compared to fixed PNP in the same range of applied PNP of 0.2 – 0.4 MPa. One-way ANOVA with Dunnett's multiple comparison's test, p<0.0001 for PCD vs. 0.2 MPa, p=0.0018 for PCD vs. 0.3 MPa, p=0.0368 for PCD vs. 0.4 MPa, p=0.2864 for PCD vs. 0.5 MPa, and p=0.9918 for PCD vs. 0.6 MPa. (E) Spectrogram of the frequency response for each burst during the FUS application averaged over CCM mice with PCD-modulated PNP (n=4 mice and 2 sonication replicates per mouse). Dotted line denotes separation of baseline sonications without microbubbles and sonications with microbubbles. (F) Subharmonic, broadband, and second harmonic emissions for CCM mice at PCD-modulated PNP and fixed PNPs of 0.4 MPa – 0.6 MPa, indicating comparable acoustic signatures for PNPs less than 0.6 MPa. Two-way ANOVA with Šidák's multiple comparisons test, p>0.8 for the subharmonic, ultraharmonic, and 2^{nd}-3^{rd} harmonic emissions for PCD vs. 0.4 or 0.5 MPa; p>0.3 for the broadband emissions; p=0.003 for 2^{nd} harmonic emissions and 0.6 MPa vs. PCD,0.4 MPa, and 0.5 MPa. (G) Representative high resolution, T2-weighted spin echo images of wild-type and CCM mice at 1 d, 7 d, and 30 d post sonication at PNPs of 0.4 MPa – 0.6 MPa in either a single sonication or repeat sonication treatment regimen. Ovals denote focal column. (H) Line graphs of

ipsilateral-to-contralateral grayscale intensities over the one-month imaging period for CCM mice and all PNP regimens. (I) Scatterplot of ipsilateral-to-contralateral grayscale intensity versus time-averaged PNP for CCM with single treatments and fixed PNP, repeat treatments and fixed PNP, or repeat treatments and PCD-modulated PNP mice on day 1 (left) or day 30 post-FUS (right). For edema, ipsilateral-to-contralateral grayscale intensity is not significantly correlated with PNP; however, for hemosiderin, ipsilateral-to-contralateral grayscale intensity is significantly correlated with PNP. Linear regression with F test, $p=0.8382$ for edema and $p=0.0163$ for hemosiderin.

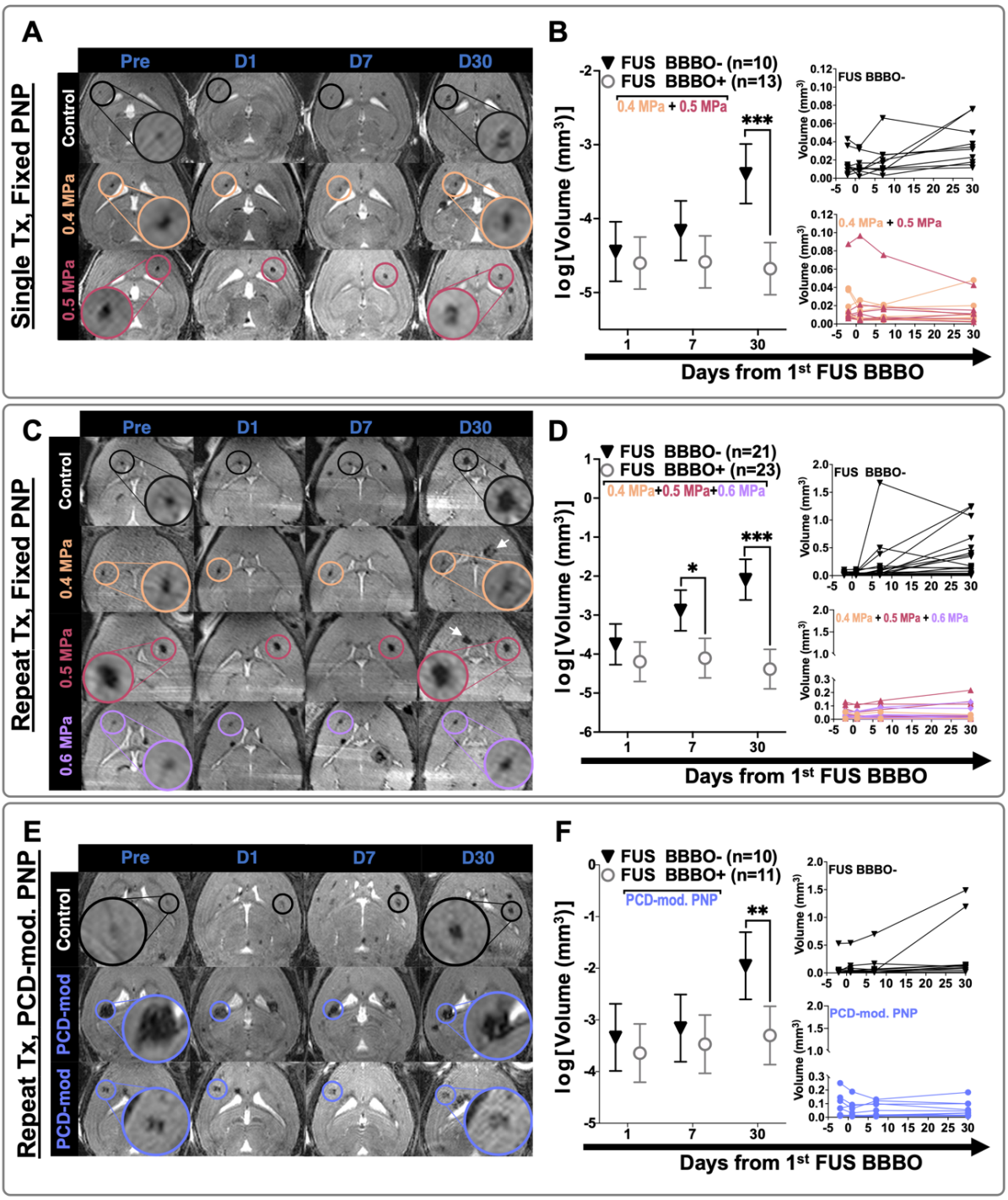
A
Single Tx, Fixed PNP
Pre
D1
D7
D30
Control
0.4 MPa
0.5 MPa
B
FUS BBBO- (n=10)
FUS BBBO+ (n=13)
0.4 MPa + 0.5 MPa
***
log[Volume (mm3)]
Volume (mm3)
FUS BBBO-
0.4 MPa + 0.5 MPa
Days from 1st FUS BBBO
C
Repeat Tx, Fixed PNP
Control
0.4 MPa
0.5 MPa
0.6 MPa
D
FUS BBBO- (n=21)
FUS BBBO+ (n=23)
0.4 MPa+0.5 MPa+0.6 MPa
*
***
FUS BBBO-
0.4 MPa + 0.5 MPa + 0.6 MPa
Days from 1st FUS BBBO
E
Repeat Tx, PCD-mod. PNP
Control
PCD-mod
PCD-mod
F
FUS BBBO- (n=10)
FUS BBBO+ (n=11)
PCD-mod. PNP
**
FUS BBBO-
PCD-mod. PNP
Days from 1st FUS BBBO

Figure 4.6. FUS BBBO arrests the growth of sonicated CCMs**.** (A, C, E) Longitudinal T2-weighted spin echo images for representative mice in the (A) single sonication with fixed PNP arm, (C) repeat sonication with fixed PNP arm, or (E) repeat sonication with PCD-modulated PNP arm. Black circles indicate non-sonicated, control lesions, and colored circles indicate sonicated lesions corresponding to PNP applied. White arrows denote new lesions formed in non-sonicated hemisphere. (B, D, F) Left: Summary plots comparing the natural log transform of CCM volume between sonicated CCMs and non-sonicated CCMs for mice in the (B) single sonication with fixed PNP arm, (D) repeat sonication with fixed PNP arm, or (F) repeat sonication with PCD-modulated PNP arm. Right: Line graphs of CCM volume for individual CCMs for each treatment group. At 30 days, sonicated CCMs are significantly smaller than non-sonicated control CCMs for all treatment arms. Linear mixed effects model: [log (Volume) ~ Treatment*Time + Starting Volume + (Mouse ID) + (Lesion ID)]; p=0.000254, p=1.64E-7, and p=0.00604 for the single, fixed PNP; repeat, fixed PNP; and repeat, PCD-mod. PNP arms, respectively. At 7 days, sonicated CCMs are significantly smaller than non-sonicated CCMs in the repeat FUS and fixed PNP arm. Linear mixed effects model: [log (Volume) ~ Treatment*Time + Starting Volume + (Mouse ID) + (Lesion ID)], p=0.0186.

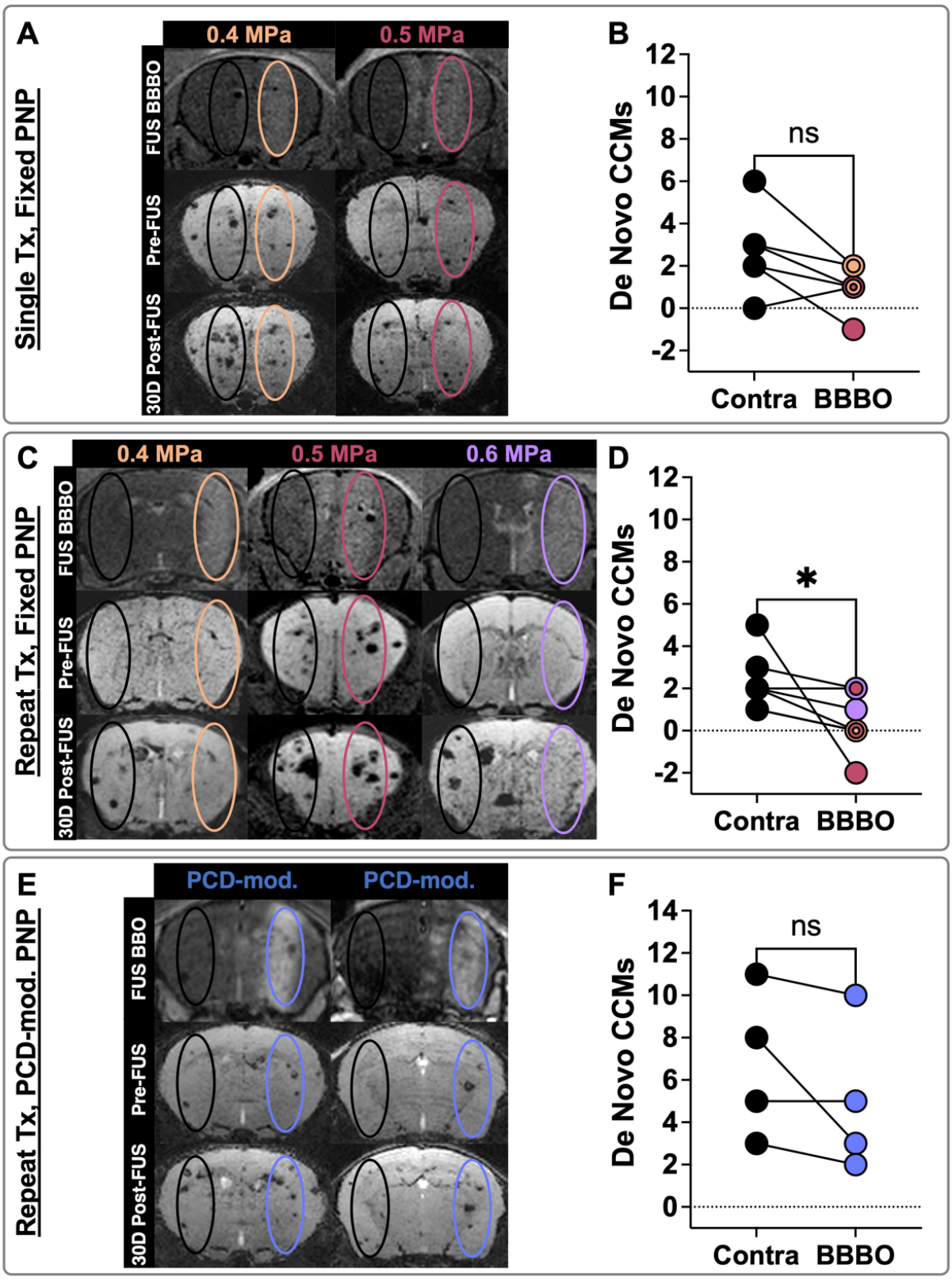
A
Single Tx, Fixed PNP
0.4 MPa
0.5 MPa
FUS BBBO
Pre-FUS
30D Post-FUS
B
De Novo CCMs
12
10
8
6
4
2
0
-2
ns
Contra
BBBO
C
Repeat Tx, Fixed PNP
0.4 MPa
0.5 MPa
0.6 MPa
FUS BBBO
Pre-FUS
30D Post-FUS
D
De Novo CCMs
12
10
8
6
4
2
0
-2
*
Contra
BBBO
E
Repeat Tx, PCD-mod. PNP
PCD-mod.
PCD-mod.
FUS BBO
Pre-FUS
30D Post-FUS
F
De Novo CCMs
14
12
10
8
6
4
2
0
ns
Contra
BBBO

Figure 4.7. FUS BBBO with fixed PNP and repeat sonications can prevent *de novo* lesion formation. (A, C, E) Top row: T1-weighted spin echo images taken immediately following FUS BBBO with hyperintense signal denoting the focal column. Middle and bottom rows: minimum intensity projection images of longitudinal T2-weighted spin echo images to visualize through 1 mm of the focal column for representative mice in the (A) single sonication with fixed PNP arm, (C) repeat sonication with fixed PNP arm, or (E) repeat sonication with PCD-modulated PNP arm. Black ovals denote contralateral, non-sonicated ROIs for *de novo* quantification, while colored ovals represent sonicated ROIs. (B, D, F) Paired line graph comparing the change in CCM number one month following FUS BBBO between the sonicated brain region and the contralateral non-sonicated brain region for mice in the (B) single sonication with fixed PNP arm, (D) repeat sonication with fixed PNP arm, or (F) repeat sonication with PCD-modulated PNP arm. Concentric circles indicate multiple mice with the same number of *de novo* CCMs. Colors indicate applied PNP. For mice receiving the repeat FUS regimen with fixed PNP, the number of new lesions formed in the sonicated brain region is significantly reduced compared to the contralateral brain region. Wilcoxon matched-pairs signed rank test, $p=0.0312$.

4.7 CHAPTER 4 SUPPLEMENTAL FIGURES

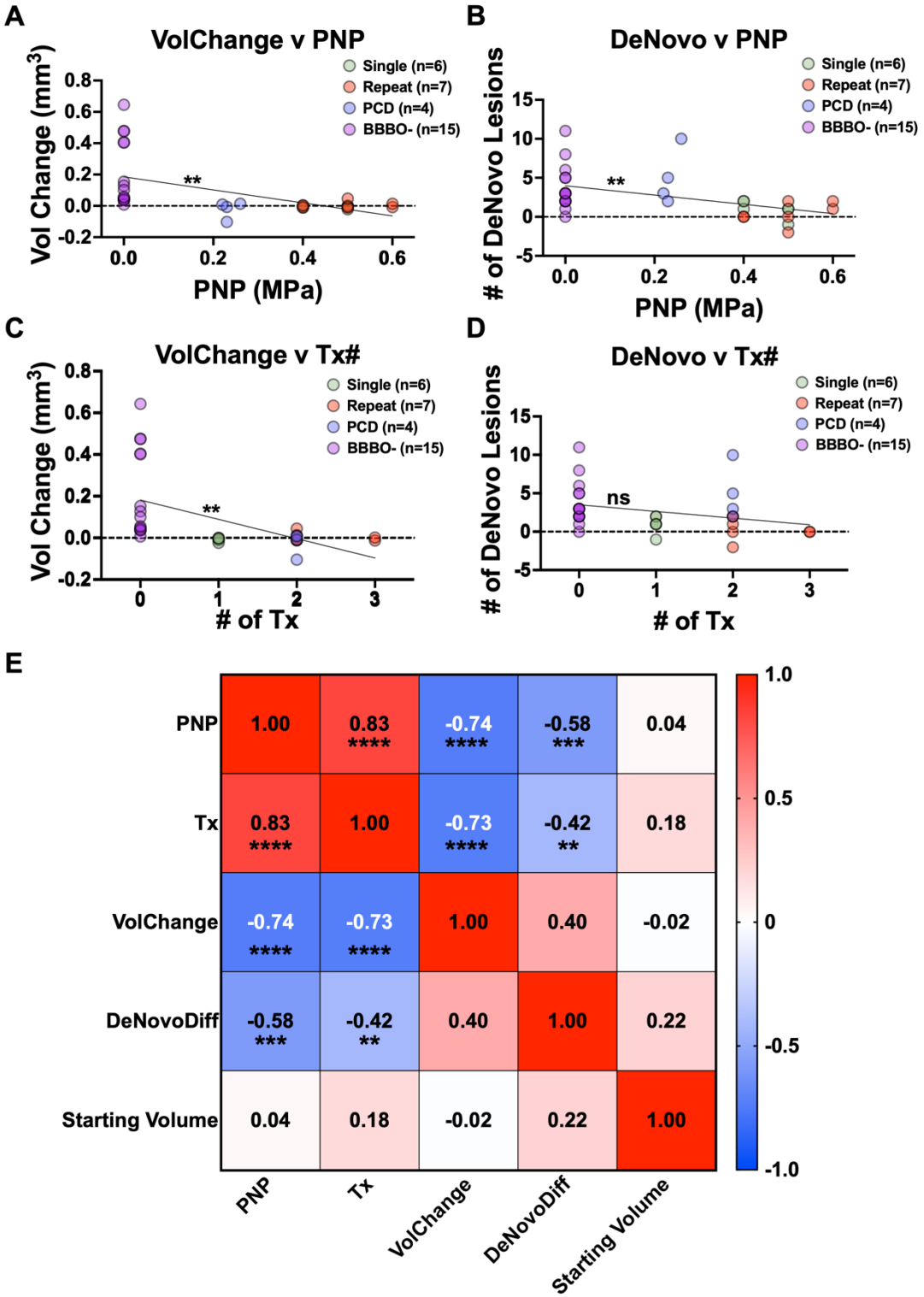

Figure 4.S1. Correlations of FUS BBBO PNP and treatment number on CCM volume change and formation. (A) Plot of lesion volume change and PNP for all treatment conditions. Linear regression indicates that volume change and PNP are inversely correlated, p=0.0017. (B) Plot of *de novo* CCM formation and PNP for all treatment conditions. Linear regression indicates that *de novo* CCM formation and PNP are inversely correlated, p=0.0064. (C) Plot of lesion volume change and number of FUS applications (i.e. Tx#) for all treatment conditions. Linear regression indicates that volume change and Tx# are inversely correlated, p=0.0021. (D) Plot of *de novo* CCM formation and number of FUS applications (i.e. Tx#) for all treatment conditions. Linear regression indicates that *de novo* CCM formation and Tx# are not inversely correlated, p=0.0914. (E) Spearman correlation matrix for FUS BBBO and CCM parameters, indicating significant inverse correlations between lesion volume change and PNP ($p<0.0001$), lesion volume change and Tx# (p=0.0006), *de novo* CCM formation and PNP ($p<0.0001$), and *de novo* CCM formation and Tx# (p=0.0164).

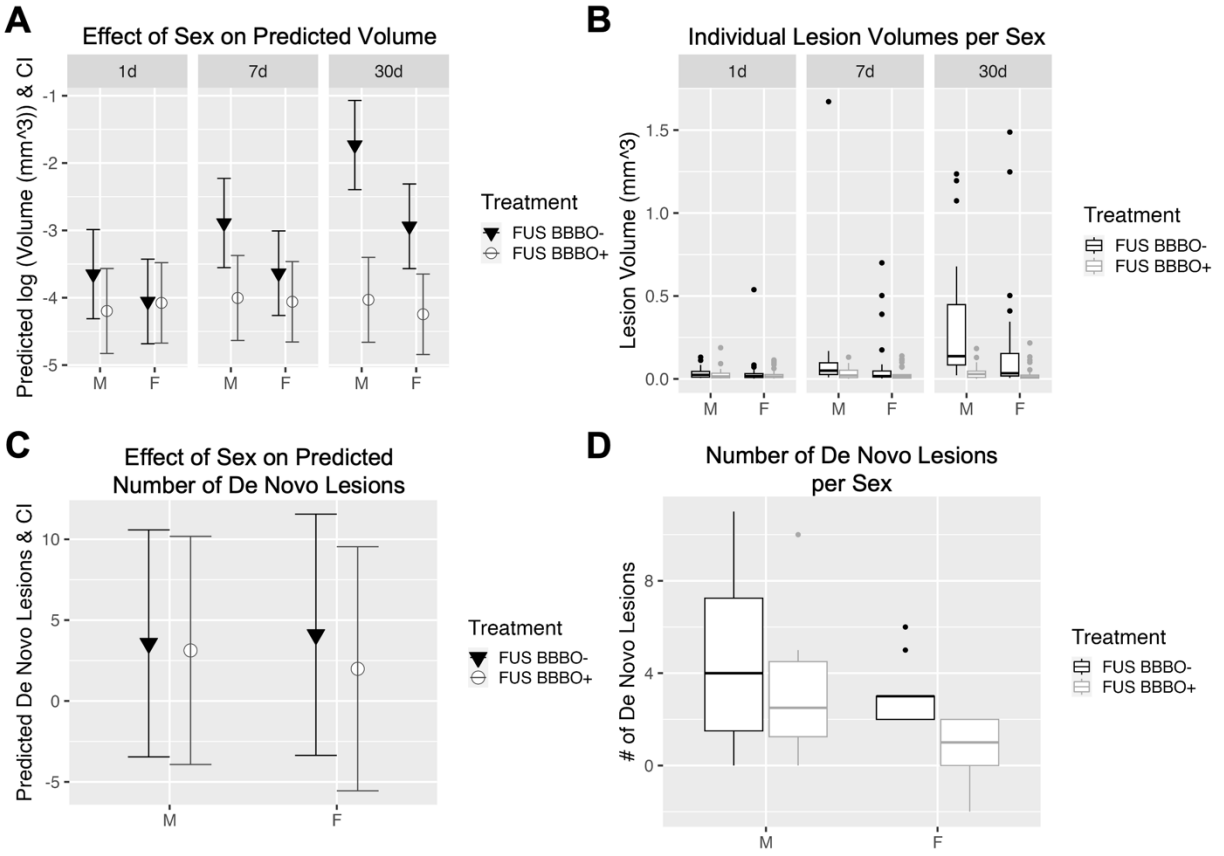

Figure 4.S2. Effect of sex on the therapeutic outcomes of FUS BBBO for CCM. (A) Summary plots comparing the natural log transform of CCM volume between sonicated CCMs and non-sonicated CCMs over time disaggregated by sex. At 1 month, CCMs in male mice were larger than those in female mice, regardless of FUS BBBO treatment (Linear mixed effect model: Table S2). Sex did not significantly alter the ability of FUS BBBO to control CCM growth (Linear mixed effect model: Table S2). (B) Plots of CCM volume for individual CCMs for each treatment group over time disaggregated by sex. (C) Summary plots comparing the number of *de novo* CCMs between sonicated CCMs and non-sonicated CCMs disaggregated by sex. Sex did not significantly alter the ability of FUS BBBO to control CCM formation (Linear mixed effect model: Table S2). (D) Boxplots of *de novo* comparing the number of *de novo* CCMs for each treatment group disaggregated by sex.

4.8 CHAPTER 4 SUPPLEMENTAL TABLES

Table S4.1: Mouse and treatment assignment characteristics

Mouse ID	Tx Cohort	PNP (or AVG PNP)	Litter #	Sex	Age at Tx (wk)
32	Repeat	0.5	1	F	10
33	Repeat	0.6	1	F	10
37	Repeat	0.4	2	M	10
38	Repeat	0.6	2	M	10
103	Repeat	0.5	3	F	9
104	Repeat	0.4	3	F	9
106	Repeat	0.4	3	F	9
81	Repeat	0.5	4	F	10
83	Repeat	0.6	4	M	10
903	Single	0.5	5	F	9
904	Single	0.4	5	F	9
74	Single	0.5	6	F	9
75	Single	0.5	6	F	9
76	Single	0.4	6	F	9
79	Single	0.4	6	M	9
841	PCD	0.26	7	M	13
831	PCD	0.23	8	M	13
306	PCD	0.22	9	M	11
311	PCD	0.23	9	F	11

Table 4.S2: Statistical tests and p-values for manuscript figures

Figure 1C: One-way ANOVA with Dunnett's Multiple Comparisons Test	
Comparison	p-value
Pre vs. 0.2	0.9986
Pre vs. 0.3	0.0054
Pre vs. 0.4	<0.0001
Pre vs. 0.5	<0.0001
Pre vs. 0.6	<0.0001
Figure 2B: Wilcoxon Matched-Pairs Signed Rank Test	
Comparison	p-value
Pre-FUS vs. Post-FUS	0.4143
Figure 2D: Wilcoxon Matched-Pairs Signed Rank Test	
Comparison	p-value
Pre-FUS vs. Post-FUS	0.3396
Figure 3B: Two-way ANOVA with Šidák's Multiple Comparisons Test	
Comparison	p-value
0.4 MPa: WT vs. CCM	0.9238
0.5 MPa: WT vs. CCM	0.9998
0.6 MPa: WT vs. CCM	0.9590
Figure 3D: Two-way ANOVA with Šidák's Multiple Comparisons Test	
Comparison	p-value
Subharmonic: 0.4 MPa: WT vs. CCM	0.8640
Subharmonic: 0.5 MPa: WT vs. CCM	0.9864
Subharmonic: 0.6 MPa: WT vs. CCM	0.9573
1st Ultraharmonic: 0.4 MPa: WT vs. CCM	0.9058
1st Ultraharmonic: 0.5 MPa: WT vs. CCM	0.9934
1st Ultraharmonic: 0.6 MPa: WT vs. CCM	0.8039
Broadband: 0.4 MPa: WT vs. CCM	0.8457
Broadband: 0.5 MPa: WT vs. CCM	0.9900
Broadband: 0.6 MPa: WT vs. CCM	0.4019
Figure 3E: Two-way ANOVA with Šidák's Multiple Comparisons Test	
Comparison	p-value
2nd Harmonic: 0.4 MPa: WT vs. CCM	>0.9999
2nd Harmonic: 0.5 MPa: WT vs. CCM	0.9998
2nd Harmonic: 0.6 MPa: WT vs. CCM	<0.0001
3rd Harmonic: 0.4 MPa: WT vs. CCM	>0.9999
3rd Harmonic: 0.5 MPa: WT vs. CCM	>0.9999
3rd Harmonic: 0.6 MPa: WT vs. CCM	0.0006
4th Harmonic: 0.4 MPa: WT vs. CCM	0.9999
4th Harmonic: 0.5 MPa: WT vs. CCM	0.7607
4th Harmonic: 0.6 MPa: WT vs. CCM	<0.0001
Figure 4B: 2nd Order Polynomial Regression Comparison of Fits	
Null hypothesis	One curve for all data sets

Alternative hypothesis	Different curve for each data set
p-value	0.0473
Figure 4C: 2nd Order Polynomial Regression Comparison of Fits	
Null hypothesis	One curve for all data sets
Alternative hypothesis	Different curve for each data set
p-value	0.7734
Figure 4E: Two-way ANOVA with Holm-Šidák's Multiple Comparisons Test	
Comparison	p-value
Single: Edema: 0.4 MPa: WT vs. CCM	0.1368
Single: Edema: 0.5 MPa: WT vs. CCM	0.1368
Single: Hemosiderin: 0.4 MPa: WT vs. CCM	0.5386
Single: Hemosiderin: 0.5 MPa: WT vs. CCM	0.5386
Repeat: Edema: 0.4 MPa: WT vs. CCM	0.7316
Repeat: Edema: 0.5 MPa: WT vs. CCM	0.9667
Repeat: Edema: 0.6 MPa: WT vs. CCM	0.0923
Repeat: Hemosiderin: 0.4 MPa: WT vs. CCM	0.9965
Repeat: Hemosiderin: 0.5 MPa: WT vs. CCM	0.5754
Repeat: Hemosiderin: 0.6 MPa: WT vs. CCM	0.9965
Figure 5C: Wilcoxon Matched-Pairs Signed Rank Test	
Comparison	p-value
Pre-FUS vs. Post-FUS	0.0156
Figure 5D: One-way ANOVA with Dunnett's Multiple Comparisons Test	
Comparison	p-value
PCD vs. 0.2	<0.0001
PCD vs. 0.3	0.0018
PCD vs. 0.4	0.0368
PCD vs. 0.5	0.2864
PCD vs. 0.6	0.9918
Figure 5F: Two-way ANOVA with Šidák's Multiple Comparisons Test	
Comparison	p-value
Subharmonic: PCD vs. 0.4	0.9993
Subharmonic: PCD vs. 0.5	>0.9999
Subharmonic: PCD vs. 0.6	0.3381
Subharmonic: 0.4 vs. 0.5	0.9995
Subharmonic: 0.4 vs. 0.6	0.5210
Subharmonic: 0.5 vs. 0.6	0.3475
Broadband: PCD vs. 0.4	0.3359
Broadband: PCD vs. 0.5	0.5648
Broadband: PCD vs. 0.6	0.6860
Broadband: 0.4 vs. 0.5	0.9979

Broadband: 0.4 vs. 0.6		0.0538	
Broadband: 0.5 vs. 0.6		0.0954	
2nd Harmonic: PCD vs. 0.4		>0.9999	
2nd Harmonic: PCD vs. 0.5		>0.9999	
2nd Harmonic: PCD vs. 0.6		0.0032	
2nd Harmonic: 0.4 vs. 0.5		>0.9999	
2nd Harmonic: 0.4 vs. 0.6		0.0027	
2nd Harmonic: 0.5 vs. 0.6		0.0031	
Figure 5I: Linear Regression			
Edema: Is slope significantly non-zero?			
F		0.05758	
DFn, DFd		1, 17	
P value		0.8132	
Equation		Y = 0.03146*X + 0.9876	
Hemosiderin: Is slope significantly non-zero?			
F		6.897	
DFn, DFd		1, 17	
P value		0.0177	
Equation		Y = -0.3262*X + 1.066	
Figure 6B: Linear Mixed Effect Model by Restricted Maximum Likelihood			
logVolume ~ Treatment * Time + Starting Volume + (1 | Mouse) + (1 | Lesion)			
Random Effects:			
Groups	Name	Variance	Std. Dev.
Lesion ID	(Intercept)	0.1452	0.3811
Mouse ID	(Intercept)	0	0
Residual		0.2248	0.4742
Fixed Effects:			
Groups	Estimate	Std. Error	p-value
Intercept	-5.0212	0.2103	2.00E-16
FUS BBBO+	-0.156	0.2569	0.546599
7d	0.2827	0.2121	0.189679
30d	1.0516	0.2121	1.22E-05
Starting Volume	31.1736	5.2957	9.30E-06
FUS BBBO+:7d	-0.2667	0.2821	0.349698
FUS BBBO+:30d	-1.1272	0.2821	0.000254
Figure 6D: Linear Mixed Effect Model by Restricted Maximum Likelihood			
logVolume ~ Treatment * Time + Starting Volume + (1 | Mouse) + (1 | Lesion)			
Random Effects:			
Groups	Name	Variance	Std. Dev.
Lesion ID	(Intercept)	0.42707	0.6535
Mouse ID	(Intercept)	0.07932	0.2816
Residual		0.57282	0.7568
Fixed Effects:			
Groups	Estimate	Std. Error	p-value

Intercept	-4.5358	0.2689	7.81E-16
FUS BBBO+	-0.4472	0.3061	0.147764
7d	0.8683	0.2336	0.000362
30d	1.658	0.2336	3.73E-10
Starting Volume	27.8133	4.1755	4.97E-08
FUS BBBO+:7d	-0.7752	0.3231	0.018627
FUS BBBO+:30d	-1.8455	0.3231	1.64E-07
Figure 6F: Linear Mixed Effect Model by Restricted Maximum Likelihood			
logVolume ~ Treatment * Time + Starting Volume + (1 | Mouse) + (1 | Lesion)			
Random Effects:			
Groups	Name	Variance	Std. Dev.
Lesion ID	(Intercept)	0.3568	0.5973
Mouse ID	(Intercept)	0	0
Residual		0.3373	0.5808
Fixed Effects:			
Groups	Estimate	Std. Error	p-value
Intercept	-3.860709	0.281417	4.12E-15
FUS BBBO+	-0.30401	0.364332	0.40962
7d	0.178492	0.259738	0.49613
30d	1.385354	0.259738	4.66E-06
Starting Volume	7.297587	1.269863	1.90E-05
FUS BBBO+:7d	-0.006141	0.35888	0.98644
FUS BBBO+:30d	-1.043723	0.35888	0.00604
Figure 7B: Wilcoxon Matched-Pairs Signed Rank Test			
Comparison		p-value	
Contra vs. BBBO		0.1250	
Figure 7D: Wilcoxon Matched-Pairs Signed Rank Test			
Comparison		p-value	
Contra vs. BBBO		0.0312	
Figure 7F: Wilcoxon Matched-Pairs Signed Rank Test			
Comparison		p-value	
Contra vs. BBBO		0.2500	
Figure S1A: Linear Regression			
Is slope significantly non-zero?			
F		11.96	
DFn, DFd		1, 30	
P value		0.0017	
Equation		Y = -0.4156*X + 0.1854	
Figure S1B: Linear Regression			
Is slope significantly non-zero?			
F		8.600	
DFn, DFd		1, 30	
P value		0.0064	
Equation		Y = -5.941*X + 3.982	
Figure S1C: Linear Regression			

Is slope significantly non-zero?					
F			11.32		
DFn, DFd			1, 30		
P value			0.0021		
Equation			Y = -0.09265*X + 0.1796		
Figure S1D: Linear Regression					
Is slope significantly non-zero?					
F			3.042		
DFn, DFd			1, 30		
P value			0.0914		
Equation			Y = -0.8686*X + 3.471		
Figure S1E: Spearman Correlation Matrix					
	PNP	Tx	VolChange	DeNovoDiff	Start Vol
PNP		p<0.0001	p<0.0001	p=0.0006	p=0.8444
Tx	p<0.0001		p<0.0001	p=0.0164	p=0.3145
VolChange	p<0.0001	p<0.0001		p=0.0223	p=0.9227
DeNovoDiff	p=0.0006	p=0.0164	p=0.0223		p=0.2356
Start Vol	p=0.8444	p=0.3145	p=0.9227	p=0.2356	
Figure S2A: Linear Mixed Effect Model by Restricted Maximum Likelihood					
logVol ~ Sex * Treatment * Time + StartVol + (1 | Mouse) + (1 | Lesion) + (1 | Cohort)					
Random Effects:					
Groups	Name		Variance	Std. Dev.	
Lesion ID	(Intercept)		0.49951	0.7068	
Mouse ID	(Intercept)		0.08626	0.2937	
Cohort	(Intercept)		0.037	0.1924	
Residual			0.41209	0.6419	
Fixed Effects					
Groups	Estimate		Std. Error	p-value	
(Intercept)	-4.43661		0.25911	3.44E-08	
M	0.40544		0.36007	0.2659	
FUSBBBO+	-0.02104		0.26514	0.9369	
7d	0.4201		0.18157	0.0219	
30d	1.11647		0.18157	5.50E-09	
Starting Volume	10.56322		1.42424	1.20E-10	
M:FUSBBBO+	-0.52574		0.42373	0.2168	
M:7d	0.33961		0.29065	0.2443	
M:30d	0.80099		0.29065	0.0065	
FUS BBBO+:7d	-0.40329		0.2498	0.1083	
FUS BBBO+:30d	-1.28541		0.2498	7.37E-07	
M:FUSBBBO+:7d	-0.16299		0.3966	0.6816	
M:FUSBBBO+:30d	-0.46596		0.3966	0.2417	
Figure S2C: Linear Mixed Effect Model by Restricted Maximum Likelihood					
De Novo Lesions ~ Sex * Treatment + StartingVolume + (1 | Mouse) + (1 | Cohort)					
Random Effects:					

Groups	Name	Variance	Std. Dev.
Mouse ID	(Intercept)	1.664	1.29
Cohort	(Intercept)	9.58	3.095
Residual		1.715	1.31
Fixed Effects:			
Groups	Estimate	Std. Error	p-value
(Intercept)	4.6864	1.9186	0.12436
M	-0.5358	1.0766	0.62392
FUS BBBO+	-2.1063	0.608	0.0036
Starting Volume	-9.7962	3.4981	0.00972
M:FUS BBBO+	1.6714	0.9845	0.11182

CHAPTER 5: MRI MAPPING TO ADVANCE FOCUSED ULTRASOUND-TARGETED THERAPEUTIC DELIVERY IN CEREBRAL CAVERNOUS MALFORMATIONS

Delaney G. Fisher[#], Matthew R. Hoch[#], Catherine M. Gorick, Khadijeh A. Sharifi, Petr Tvrdik, G. Wilson Miller, Richard J. Price

[#] authors contributed equally

5.1 ABSTRACT

BACKGROUND: Cerebral cavernous malformations (CCMs) are abnormal blood vessel clusters in the brain, inducing recurring hemorrhages and debilitating symptoms in affected individuals. Surgical resection, the primary treatment, poses significant risks, motivating the need for effective nonsurgical interventions. Focused ultrasound-mediated blood-brain barrier opening (FUS BBBO) has emerged as a promising non-invasive drug delivery technology, and our recent findings demonstrate its ability to arrest CCM growth. Building on this discovery, this study employs quantitative MRI methods to evaluate the delivery of different-sized molecules to CCMs with and without FUS BBBO, laying the foundation for potential treatment regimens to induce CCM regression and clearance.

METHODS: Quantitative T1 mapping MRI sequences were used with 1 kDa (MultiHance) and 17 kDa (GadoSpin D) contrast agents to measure model drug delivery with FUS BBBO. These measurements enabled temporal assessments of delivery after contrast injection and/or FUS BBBO along with spatial assessments of delivery in the CCM core and perilesional space.

RESULTS: FUS BBBO significantly elevated the delivery rate of MultiHance in the lesion core 3-fold and in the perilesional space 5-fold. Representing the therapeutic potential of FUS BBBO for small molecules, the total delivery of MultiHance more than doubled in the lesion core and tripled in the perilesional space when FUS BBBO was applied immediately prior to contrast injection. The benefit of FUS BBBO enhanced delivery in CCMs was even more apparent for biologic-sized molecules, as demonstrated by 22-fold and 3.8-fold increases in the lesion core and perilesional space, respectively, for GadoSpin D. Intriguingly, our results predict that FUS BBBO will elicit greater small molecule delivery to the perilesional space and greater small biologic delivery to the intralesional space.

CONCLUSIONS: This work showcases the capacity of FUS BBBO to enhance therapeutic delivery across diverse molecular sizes to the CCM microenvironment. Combined with our prior demonstration of its independent efficacy in halting CCM growth and formation, these findings highlight the unprecedented potential of FUS BBBO to generate transformative treatment paradigms for CCM.

5.2 INTRODUCTION

Cerebral cavernous malformation (CCM) is a vascular disorder characterized by the development of abnormal, dilated clusters of blood vessels in the brain[1]. These malformations are prone to repetitive hemorrhages, inducing debilitating symptoms, such as neurological deficits, seizures, and stroke, in affected individuals[43–45]. Presently, the prevailing recourse for treating symptomatic CCMs is surgical resection. However, surgical excision of CCMs poses an elevated risk of complications and morbidity, evident by a distressing rate of surgical adverse events[2,103].

Despite multiple studies investigating therapeutic targets and screening pharmacological treatments for CCM[104–115], effective nonsurgical interventions remain elusive. The majority of tested pharmacological agents for CCM are small molecules, highlighting the unexplored potential of larger molecules such as antibodies and gene therapies. Additionally, drugs showing promise in acute CCM models often demonstrate limited efficacy in more clinically-representative chronic models, suggesting a potential need for greater local doses of these therapies[52,53]. Indeed, though CCMs are known to be more permeable than healthy cerebrovasculature[11,13,14,40], delivery of systemically administered drugs to these lesions is poorly understood.

Focused ultrasound (FUS)-mediated blood-brain barrier opening (BBBO) has emerged as a promising non-invasive drug delivery technology[25,79,80]. FUS concentrates acoustic energy into a confined volume, facilitating the oscillation of intravenously administered gas-filled microbubbles within blood vessels of the targeted region. These microbubble oscillations induce a transient disruption of endothelial tight junctions[116] and increased active transport[117], enabling therapeutic delivery across the BBB. Magnetic resonance imaging (MRI) guidance permits spatial targeting of FUS BBBO to specific brain regions and BBBO confirmation through the accumulation of gadolinium-based MRI contrast agents.

Recently, our group demonstrated that FUS BBBO, in the absence of therapeutic delivery, arrests the growth of CCMs[118]. This remarkable observation prompts the exploration of the combined impact of FUS BBBO-mediated lesion stabilization and therapeutic delivery on CCMs. While our previous study also confirmed that FUS BBBO enhanced MRI contrast beyond the natural permeability of CCMs, the MRI sequences only provided qualitative assessments. In particular, this qualitative MRI approach was sub-optimal for visualizing contrast agent delivery to the lesion core. Indeed, the cellular and molecular composition within the lesion core, including mutated endothelium, red blood cells, and their byproducts, differs substantially from the perilesional space, characterized by dense populations of astrocytes and microglia[93,118]. This difference not only affects MRI signal but may also have implications for drug delivery to these distinct regions. Consequently, to facilitate comprehensive measurements of potential enhanced therapeutic delivery with FUS BBBO in the intricate CCM microenvironment, quantitative MRI methods are needed.

Building on our recent demonstration of the growth-arresting effect of FUS BBBO on CCMs[118], the objective of this study is to establish a foundation for therapeutic delivery approaches that harness and synergize with this potent bioeffect. We have previously demonstrated that T1-contrast mapping can enable longitudinal, quantitative concentration measurements of gadolinium-based molecules in CCMs[93]. Thus, this is an ideal method to measure FUS BBBO-induced changes for therapeutic delivery to CCMs. To this end, we employed T1-contrast mapping MRI to quantitatively evaluate the delivery of a 1 kDa and a 17 kDa molecule to CCMs, comparing outcomes with and without FUS BBBO. This pursuit aims to lay the groundwork for treatment regimens capable of inducing CCM regression and clearance.

5.3 RESULTS

5.3.1 FUS BBBO ENHANCES DELIVERY RATE OF MULTIHANCE IN CCMS

We first tested if FUS BBBO would increase the delivery rate of a small molecule to the CCM microenvironment. We employed T1 mapping MRI to measure the concentration of the MRI contrast agent MultiHance (gadobenate dimeglumine; ~1 nm; ~1 kDa) before and after the application of FUS BBBO in CCM mice. One frontal hemisphere received FUS BBBO (6 sonication targets) with PCD feedback control 20 minutes following intravenous (i.v.) MultiHance injection. Meanwhile, the contralateral hemisphere was not sonicated (i.e., FUS- control) to illustrate the natural, baseline permeability in CCMs. As expected, prior to FUS BBBO, CCMs in the non-sonicated and sonicated hemispheres displayed similar rates of MultiHance accumulation (**Figure 5.1A**). FUS BBBO enhanced the fold change in MultiHance concentration in the lesion core 15 mins post-sonication ($p=0.0162$; **Figure 5.1A**) and also increased the delivery rate in the lesion core compared to the natural permeability of CCMs ($p=0.0221$; **Figure 5.1B**). Following FUS BBBO, the intralesional rate of MultiHance accumulation increased over the pre-FUS rate in the FUS-treated hemisphere by a factor of 3.1 while the rate of accumulation in the untreated hemisphere decreased between these time segments by a factor of 1.5 (**Figure 5.1B**). Predictably, the perilesional space of these CCMs also displayed the same permeability rate prior to FUS BBBO in both groups (**Figure 5.1C**). FUS BBBO trended towards augmenting fold change in MultiHance concentration in the perilesional space 15 mins post-sonication ($p=0.1342$; Figure 1C) and significantly increased the delivery rate in the perilesional space compared to the natural CCM permeability ($p<0.0001$; **Figure 5.1D**). Following FUS BBBO, the perilesional rate of MultiHance accumulation increased over the pre-FUS rate in the FUS-treated hemisphere by a factor of 5.0 while the rate of accumulation in the untreated hemisphere decreased between these time segments by a factor of 1.3 (**Figure 5.1D**). These results indicate that FUS BBBO enhances

the delivery rate of small molecules both in the lesion core and in the surrounding CCM microenvironment.

5.3.2 FUS BBBO Enhances Total Delivery of MultiHance in CCMs

We then tested the ability of FUS BBBO to augment small molecule delivery to CCMs using a protocol wherein the timing of i.v. MultiHance injection with respect to FUS BBBO application was specifically chosen to yield highly effective model drug delivery. For these experiments, T1 mapping MRI was conducted on CCM mice following MultiHance i.v. injection for 20 mins. One day later, FUS BBBO was applied to one frontal hemisphere of the same CCM mice immediately before i.v. Multihance injection. T1 mapping MRI was conducted for 20 mins thereafter. FUS BBBO boosted the intralesional space mean concentration of MultiHance 2.5-fold (p=0.0070; **Figure 5.2A**) and the perilesional space concentration 3.1-fold (p=0.0005; **Figure 5.2B**) at 20 mins post injection. Area under the curve measurements, which represent the integrated exposure of CCM tissue to the model drug through time, also suggest that FUS BBBO enhances total delivery to both the intralesional (1.9-fold; p=0.0122; **Figure 5.2C**) and the perilesional (2.9-fold; p=0.0007; **Figure 5.2D**) spaces. MultiHance delivery after FUS BBBO is evident in the perilesional space before the intralesional space (0.040 mM versus 0.029 mM, respectively, after 4.4 mins), yet both locations plateau to the same mean concentration by 20 mins post-injection (0.069 mM each). These results reveal that FUS BBBO can more than double the amount of a small molecule delivered to the lesion core and triple the amount in the surrounding CCM microenvironment.

5.3.3 FUS BBBO Enhances Total Delivery of GadoSpin D in CCMs

Next, we tested the ability of FUS BBBO to enhance the total delivery of a model drug with a size that is larger and more representative of biologic agents, which are typically >1 kDa. Specifically, we compared the total delivery of the MRI contrast agent GadoSpin D (dendritic Gd-chelate; ~5 nm; ~17 kDa) with and without FUS BBBO in the same CCMs. FUS BBBO improved the total GadoSpin D delivery in both the intralesional space and the perilesional space compared to the natural CCM permeability (**Figure 5.3A, B**). Strikingly, FUS BBBO elicited a 22-fold increase in GadoSpin D delivery to the lesion core (p=0.0106; **Figure 5.3A**) and amplified perilesional delivery by 3.8-fold (p= 0.0021; **Figure 5.3B**) at 20 mins post-injection. Area under the curve analysis also indicated that FUS BBBO increased the total CCM tissue exposure of GadoSpin D with a 4.8-fold increase in intralesional exposure (p=0.0078; **Figure 5.3B**) and a 2.2-fold increase in perilesional exposure (p=0.0195; **Figure 5.3D**). The lesion core and perilesional space follow a similar temporal pattern of enhancement following FUS BBBO, but the intralesional space peaks at a higher concentration than the perilesional space (0.010 mM versus 0.0076 mM, respectively). These data demonstrate that FUS BBBO can boost the delivery of biologic agents in the ~5 nm (~17 kDa) range by more than 20-fold in the lesion core and 4-fold in the CCM microenvironment.

5.3.4 FUS BBBO Differentially Enhances Total Delivery Location for MultiHance versus GadoSpin D

Lastly, we investigated if FUS BBBO differentially affects total delivery of MultiHance and GadoSpin D. To this end, we first compared the magnitude of FUS BBBO enhancement for the two contrast agents (**Figure 5.4A-B**). In the lesion core, GadoSpin D trended towards a greater delivery enhancement with FUS BBBO (**Figure 5.4A**); however, the variability of enhancement

was much larger with GadoSpin D compared to MultiHance (**Figure 5.S1A**). In the perilesional space, MultiHance and GadoSpin D predominantly experienced the same degree of enhancement (**Figure 5.4B**), with trends in differential enhancement only apparent after 15 mins post-injection (**Figure 5.S1B**). Next, we compared the location most enhanced by FUS BBBO for the two contrast agents. Area under the curve analysis uncovered a statistically significant difference in the location of FUS BBBO enhancement for GadoSpin D and MultiHance ($p=0.0449$; **Figure 5.4C**). The intralesion-to-perilesion ratio of FUS BBBO enhancement was larger than one for all GadoSpin D timepoints suggesting preferential enhancement in the intralesional space, while this ratio was less than one for most MultiHance timepoints, suggesting a greater enhancement in the perilesional space (**Figure 5.S1C**). These results indicate that FUS BBBO has a greater effect on small molecule delivery to the perilesional space and a greater effect on small biologic delivery to the intralesional space.

5.4 Discussion

In our prior work, we elucidated that FUS BBBO halts CCM growth and diminishes CCM formation, even in the absence of therapeutic delivery[118]. Building on this baseline offered by FUS BBBO, we now aimed to advance these curative effects by establishing the synergistic potential for concurrent therapeutic delivery with this approach. Utilizing longitudinal T1 mapping MRI, we quantified the impact of FUS BBBO on therapeutic delivery of varying-sized molecules, modeling small molecule and biologic drugs, in CCMs. Our findings revealed a significant enhancement in the delivery rate of a 1 kDa small molecule, exhibiting a 3-fold increase in the lesion core and a 5-fold increase in the perilesional space. Moreover, FUS BBBO augmented overall delivery of both the 1 kDa small molecule and a 17 kDa model biologic to CCMs, with a 2.5-fold increase for the small molecule and an impressive 22-fold increase for the model biologic in the lesion core. In the perilesional space, there was a 3.1-fold increase for the small molecule and a 3.8-fold increase for the model biologic. Finally, our analysis uncovered a nuanced aspect of FUS BBBO enhancement, wherein the effect is more pronounced for the small molecule in the perilesional space and for the model biologic in the lesion core. These results collectively establish a robust foundation for employing FUS BBBO in targeted treatment regimens to effectively mitigate CCMs.

5.4.1 T1 Mapping MRI Enables Spatiotemporal, Intra-CCM, Delivery Comparisons

Given the notable heterogeneity in CCM permeability[12,14,93], methods allowing for comparative measurements in the same CCMs over time are crucial for generating accurate conclusions. As demonstrated in Fisher and Sharifi et al., T1 mapping enables longitudinal and quantitative assessments of contrast agent deposition in individual CCMs[93]. Thus, this MRI approach is ideal for comparing drug accumulation across different delivery techniques and

pharmacological agents. Moreover, this approach permits sufficient spatial resolution to discern differences in the diverse compartments of the CCM tissue. Indeed, the lesion core harbors mutated, cavernous vessels filled with clotted blood components, while the perilesional space surrounds the core with dense populations of astrocytes, microglia, and macrophages[93,118,119]. These regional differences in the CCM microenvironment pose varying biotransport challenges that can influence the efficacy of different delivery approaches and molecule sizes. T1 mapping MRI enabled us to capture differences in delivery, with and without FUS BBBO, for 1 kDa and 17 kDa molecules, within distinct regions of the CCM microenvironment. Ultimately, T1 mapping MRI provides a far superior approach for spatiotemporal drug delivery comparisons in the CCM microenvironment, surpassing end-point-requiring assessments such as immunohistochemistry.

5.4.2 FUS BBBO Increases the Local Concentration of Therapeutics to the CCM Microenvironment

We previously showed that FUS BBBO elevated T1 contrast enhancement in the CCM microenvironment with qualitative MRI methods[118]. However, this qualitative MRI approach did not enable important observations for therapeutic delivery, such as exact concentration measurements, contrast visualization in the lesion core, or comparisons with other molecules. Thus, in this study, we addressed these limitations by employing T1 mapping following contrast agent delivery with FUS BBBO in CCM mice. As expected, T1 mapping confirmed that FUS BBBO increases delivery rate and total delivery of MultiHance, the same contrast agent used in our previous study. Notably, T1 mapping enabled us to measure the exact concentration of MultiHance and GadoSpin D in both the intralesional and perilesional spaces, with and without FUS BBBO. Expanding these measurements to therapeutic delivery, we anticipate FUS BBBO to more than double the delivery of small molecule therapeutics and more than quadruple the

delivery of small biologics to CCMs. Ultimately, our findings underscore the potential of FUS BBBO in significantly improving the local dose of therapeutics in the CCM microenvironment.

5.4.3 Differential Spatial Delivery Enhancement for Varying-sized Molecules with FUS BBBO

In this study, we uncover that FUS BBBO differentially augments where in the CCM microenvironment molecules of differing sizes are delivered. Specifically, we observe greater delivery to the perilesional space for MultiHance and in the intralesional space for GadoSpin D. Projecting these findings to therapeutic delivery, we anticipate that FUS BBBO will exert the most significant impact on increasing the local dose to the lesion core with biologics and to the perilesional space with small molecules. However, a closer inspection of Figure 5.4 suggests that the enhancement of small molecules and biologics with FUS BBBO will be comparable in the perilesional space, while in the lesion core, biologic enhancement will be elevated compared to small molecules. Thus, these data collectively indicate that biologics stand to gain the most from delivery augmentation with FUS BBBO for the CCM microenvironment as a whole.

5.4.4 Potential Causes of Differential Spatial Enhancement for Varying-sized Molecules

To explore the potential causes behind the observed differential spatial delivery of varying-sized molecules with FUS BBBO, it is important to recognize vascular permeability as a spectrum. FUS BBBO does not discretely eliminate the physical barrier; rather, it modulates permeability, offering varying degrees of benefit based on the diffusion constraints of a given molecule[120]. Noting that the increase in permeability induced by FUS had a greater effect for MultiHance in the

perilesional space, we postulate that the benefit of FUS for a small molecule delivery in regions with an already disrupted BBB (i.e. the lesion core) is less than in areas that have a more intact BBB (i.e. the perilesional space). Conversely, for a 17 kDa molecule like GadoSpin D, crossing the disrupted BBB in the lesion core may be less feasible due to biophysical constraints against transporting a larger molecule. FUS BBBO partially alleviate these constraints, applying radiation forces and promoting transport processes that ultimately provide a larger benefit for larger molecules than for small molecules in the leaky CCM core. In regions harboring a more intact BBB, even small molecules cannot effectively cross into the brain parenchyma; thus, FUS BBBO is anticipated to have a larger benefit in this region. For larger molecules, the advantage of FUS may be less pronounced in regions with an intact BBB than in regions with a disrupted BBB, once again due to increased biophysical transport constraints. Collectively, these results shed light on the biotransport challenges inherent in different compartments of the CCM microenvironment for therapeutic delivery.

5.4.5 Non-Responders to FUS BBBO are More Prevalent for MultiHance than GadoSpin D

While uncommon, some CCMs did not exhibit enhancement with FUS BBBO. Intriguingly, non-responsiveness was more frequently observed with MultiHance delivery compared to GadoSpin D. Once more, the spatial compartment of the CCM appears to influence these outcomes. For MultiHance, the delivery rate of several CCMs was not elevated in the lesion core with FUS BBBO compared to non-sonicated CCMs, but the delivery rate was elevated in the perilesional space for almost all CCMs. Moreover, the total delivery of MultiHance did not meaningfully increase in the lesion core for four CCMs, but this only occurred in the perilesional

space of 2 CCMs. Conversely, the total delivery of GadoSpin D increased in the lesion core for all CCMs and all but two in the perilesional space.

In addition to the factors mentioned earlier, additional considerations may shed light on the varying enhancement of drug delivery with FUS BBBO in different spatial compartments of CCM. First, distinct transport mechanisms modulated by FUS BBBO may contribute to responsiveness in drug delivery enhancement for small and large molecules. FUS BBBO disruption of tight junctions[116], which would primarily benefit small molecules, may have little impact in the lesion core where the mutated endothelium already has disrupted junctions. However, tight junction disruption would still be effective for the perilesional vasculature. FUS BBBO can also increase active transport[117], which may vary in its effect for different-sized molecules. Given the different cell populations in the intralesional and perilesional spaces, FUS-induced active transport may also differ for different compartments of the CCM.

Moreover, hemodynamic factors may also play a role in drug delivery responsiveness. The CCM microenvironment has altered blood flow dynamics, characterized by delayed and poor perfusion[121,122]. Additionally, FUS BBBO can alter blood flow dynamics, changing convective gradients[123–125] and reducing the blood flow transiently following sonication[126]. The integrated effect of these complex dynamics for differing sized-molecules are unknown but are likely to be disparate.

Lastly, clearance mechanisms within the CCM microenvironment for small molecules and biologics could also impact the integrated exposure of tissue to drug. While there is evidence that FUS BBBO alters clearance mechanisms through modification of the glymphatic system[127–129] and BBB efflux pumps[130,131], its specific influence on the clearance of varying-sized molecules remains unclear. Our data indicates that GadoSpin D concentrations rapidly decrease without

FUS BBBO compared to MultiHance without FUS or GadoSpin D with FUS, highlighting that differential clearance is likely a significant determinant of tissue-drug exposure.

The differential responsiveness of contrast agents to FUS BBBO in CCMs emphasizes the need for a multifaceted approach to understanding the intricate interplay between drug properties, CCM spatial compartments, and FUS BBBO effects. This observation sheds lights on numerous factors influencing drug delivery in CCMs, which will be important for optimizing therapeutic strategies in the clinical management of these lesions.

5.4.5 Potential for Clinical Impact on Therapeutic Delivery in CCM

The objective of this work was to showcase the transformative potential of FUS BBBO in CCM treatment, owing to its independent bioeffects and synergistic therapeutic delivery capabilities. We demonstrate that FUS BBBO enhances therapeutic delivery for molecules of different sizes in both the CCM core and surrounding perilesional space. In the clinic, this heightened delivery translates to increased local delivery given the same systemic dose, thereby increasing the therapeutic index. Furthermore, enhanced on-target drug delivery reduces the risk of side effects associated with off-target delivery. The greater benefit observed for larger molecules with FUS BBBO opens the door for biologic delivery exploration for CCM. Indeed, our study highlights that, in the absence of FUS BBBO, the delivery of biologics is minimal, with rapid clearance for both the intralesional and perilesional spaces. However, with FUS BBBO, biologic-sized molecules are effectively retained in both CCM compartments. These findings pave the way for future investigation into even larger molecules with promising therapeutic potential for CCM, such as antibodies and gene therapy vectors.

Notably, FUS BBBO offers a level of precision that can be customized for either familial or sporadic cases of CCM. In these studies, we induce BBBO in a substantial volume—almost

one-quarter—of the CCM brain. In contrast, our previous study showcased targeting to a limited volume of the CCM brain[118]. For patients, FUS BBBO can be tailored to target a large volume, which may be necessary for familial patients with multiple CCMs, or it can be focused on a singular CCM, as is likely needed for sporadic cases. Moreover, the region of delivery can also be adapted for the mechanism of action of the delivered therapeutic. Drugs with a preventative effect could be more widely delivered than those with specific corrective functions in the CCM microenvironment. Ultimately, with its potent bioeffects and seamless integration with therapeutic delivery, FUS BBBO offers an unparalleled potential for the treatment of CCM.

5.5 Materials and Methods

5.5.1 Animals

All animal experiments conducted in this study adhered to ethical guidelines and were approved by the University of Virginia Animal Care and Use Committee. The animals were housed in accordance with standard laboratory conditions, maintaining a temperature of 22°C and a 12-hour light/12-hour dark cycle. The generation of the CCM murine model utilized in these investigations was established as previously detailed[93]. Briefly, *Krit1*$^{fl/null}$ or *Krit1*$^{fl/fl}$ male or females were generated under the endothelial promoter Pdgfb^{CreER}. On postnatal day 5, induction of *Krit1* was initiated with a subcutaneous injection of tamoxifen (50 µL at 2mg/mL in corn oil). Genotypes were subsequently verified using Transnetyx (Cordova, TN). Mice were studied between 2 and 3 months old.

5.5.2 MRI Acquisition

Data for T1 maps were acquired with a set of multi-slice 2D spin echo (SE) images at varied repetition times (TR) to generate a saturation recovery curve. 2 sets of 7 images, total of 14 scans, were acquired prior to FUS and contract agent administration to obtain saturation recovery curves with a satisfactory dynamic range. The two sets of image series were offset by the slice thickness in the slice select plane to ensure 3D coverage of the brain. The parameters for these scans were: TR=790, 1040, 1350, 1750, 2300, 3215, and 7000 ms, TE=6.71 ms, slice thickness=0.6 mm, slice gap=0.6 mm, FOV=35 x 35 mm, matrix size=180 x 180, rare factor=10, and R= 0.194 x 0.194 x 0.6 mm^3. After FUS and contrast agent administration, 14 SE images were acquired with identical parameters except at a fixed TR=1040 ms. The acquisitions alternated between slice package orientations resulting in 7 images at each slice profile geometry. Time per acquisition was 1 minute and 28 seconds.

5.5.3 DATA PROCESSING

A saturation recovery approach was utilized to calculate M_0 and all T1 values (pre and post contrast) on a voxel-by-voxel basis by fitting the data to the signal equation:

$$|S| = M_0\left(1 - e^{\frac{-TR}{T1}}\right)e^{\frac{-TE}{T2}} \qquad \text{Eqn [5.1]}$$

In equation 5.1, $|S|$ is the magnitude of the signal within the voxel, M_0 is the product of the thermal equilibrium magnetization and coil sensitivity, TR is the repetition time (ms), T1 is the spin-lattice relaxation (ms), TE is the echo time (ms), and T2 is the spin-spin relaxation (ms). The echo time exponential is assumed to be 1 due to TE<<T2, resulting in the final form seen in equation 5.2.

$$|S| = M_0\left(1 - e^{\frac{-TR}{T1}}\right) \qquad \text{Eqn [5.2]}$$

A custom written MATLAB script fit the signal magnitude data on a voxel-by-voxel basis to equation 5.2. Each fitting procedure simultaneously fit the data to 8 functions: function 1 incorporated the 7 pre-contrast variable TR scans, while functions 2-8 incorporated the singular scan at a fixed TR but different time points. The fits were constrained to having the same M_0 value but allowed different T1 values. Pre-contrast and post-contrast T1 values were then used to calculate the contrast agent concentration on a voxel-by-voxel basis at each time point using equation 5.3.

$$\frac{1}{T_{1\_Post}} = \frac{1}{T_{1\_Pre}} + r_1 C_1 \quad \text{Eqn [5.3]}$$

In equation 5.3, T_{1_Post} is the post-contrast value at a particular time point (ms), T_{1_Pre} is the pre-contrast T1 value (ms), r_1 is the contrast agent relaxivity (L/mmol/ms), and C1 is the contrast agent concentration (mM). At the conclusion of this process, concentration values for slice package 1 existed for time points (minutes): 1.47, 4.40, 7.33, 10.27, 13.2, 16.13, and 19.07, while concentration values for slice package 2 existed for time points (minutes): 2.93, 5.87, 8.80, 11.73, 14.67, 17.60, and 20.53. To obtain 3D coverage at each time point, concentration data was calculated at the missing time points by linearly interpolating between the acquired points. This required an assumption of 0 concentration at minute 0 for slice package 2. The 20.53-minute time point was not used because it required data be extrapolated past minute 19.07 for slice package 1.

A second custom MATLAB script was used to calculate average concentrations with manually drawn regions of interest (ROIs) on the concentration maps. To ensure the iron rich intralesional data was not skewed by susceptibility artifacts, a data exclusion method was developed. Briefly, a ROI of healthy brain tissue on the contralateral hemisphere was used to calculate an average residuals value for the fit. If any residuals value for the voxels within the lesion core were 3 times greater than this average, they were excluded from the analysis. The value of 3 was empirically determined. To maintain consistency within data processing, this was also applied to all perilesional data.

5.5.4 FUS BBBO

The FUS BBBO procedure was conducted using the RK-300 small bore FUS device (FUS Instruments, Toronto, CA). Mice were prepared by shaving and depilating their heads before being placed in a supine position and coupled to the transducer using degassed ultrasound gel. BBBO was achieved using a 1.1 MHz single-element transducer with a 10 ms burst length over a 2000 ms period. A total of 60 sonications were administered during a 2-minute sonication duration. The FUS Instruments software, operating in the "Blood-brain Barrier" mode, facilitated PCD-modulated PNP. The feedback control system parameters were set as follows: a starting pressure of 0.2 MPa, pressure increment of 0.05 MPa, maximum pressure of 0.4 MPa, 20 sonication baselines without microbubbles, area under the curve (AUC) bandwidth of 500 Hz, AUC threshold of 10 standard deviations, pressure drop of 0.95, and frequency selection of the subharmonic, first ultraharmonic, and second ultraharmonic. Optison™ (GE HealthCare) microbubbles were intravenously injected as a bolus dose of 10^5 microbubbles per gram of body weight. Prior to sonication, the distribution of microbubble diameter and concentration was assessed using a Coulter counter (Multisizer 3; Beckman Coulter, Fullerton, California). T1 mapping MRI sequences were used to guided sonication targeting. Six non-overlapping sonication targets were placed over one frontal hemisphere with placement optimized to target CCMs.

5.5.5 Contrast Agent Injections

MultiHance ® (gadobenate dimeglumine; Bracco) and GadoSpin D™ (dendritic Gd-chelate; Viscover) were injected as a bolus intravenously at a dose of 0.01 and 0.0002 mmol, respectively, diluted in saline. Injection of contrast agent was given immediately prior to MRI acquisition for FUS- control studies and immediately following the initiation of FUS BBBO for FUS+ studies.

5.5.6 Passive Cavitation Detection

Acoustic emissions during FUS BBBO were detected with a fiber-optic hydrophone (Precision Acoustics, Dorset, UK) of 10 um diameter and 15 mm aperture center-mounted within the ultrasound transducer. Emissions data was processed with a custom MATLAB script. The area under the curve of the acoustic emissions at the subharmonic (0.5f) and ultra-harmonics (1.5f, 2.5f) after applying a 300 Hz bandwidth filter. Broadband emissions were evaluated by summing acoustic emissions following the removal of all emissions at the fundamental frequency, harmonics (2f, 3f, 4f), subharmonic (0.5f), and ultra-harmonics (1.5f, 2.5f, 3.5f).

5.5.7 Statistical Analysis

All results are reported as mean ± standard error of the mean (SEM). The “n” values per group are made evident either by individual data points shown or statement of “n” value in figure or figure legend. Statistical significance was assessed at $p < 0.05$ for all experiments and were calculated using GraphPad Prism 9 (San Diego, USA).

5.6 CHAPTER 5 FIGURES

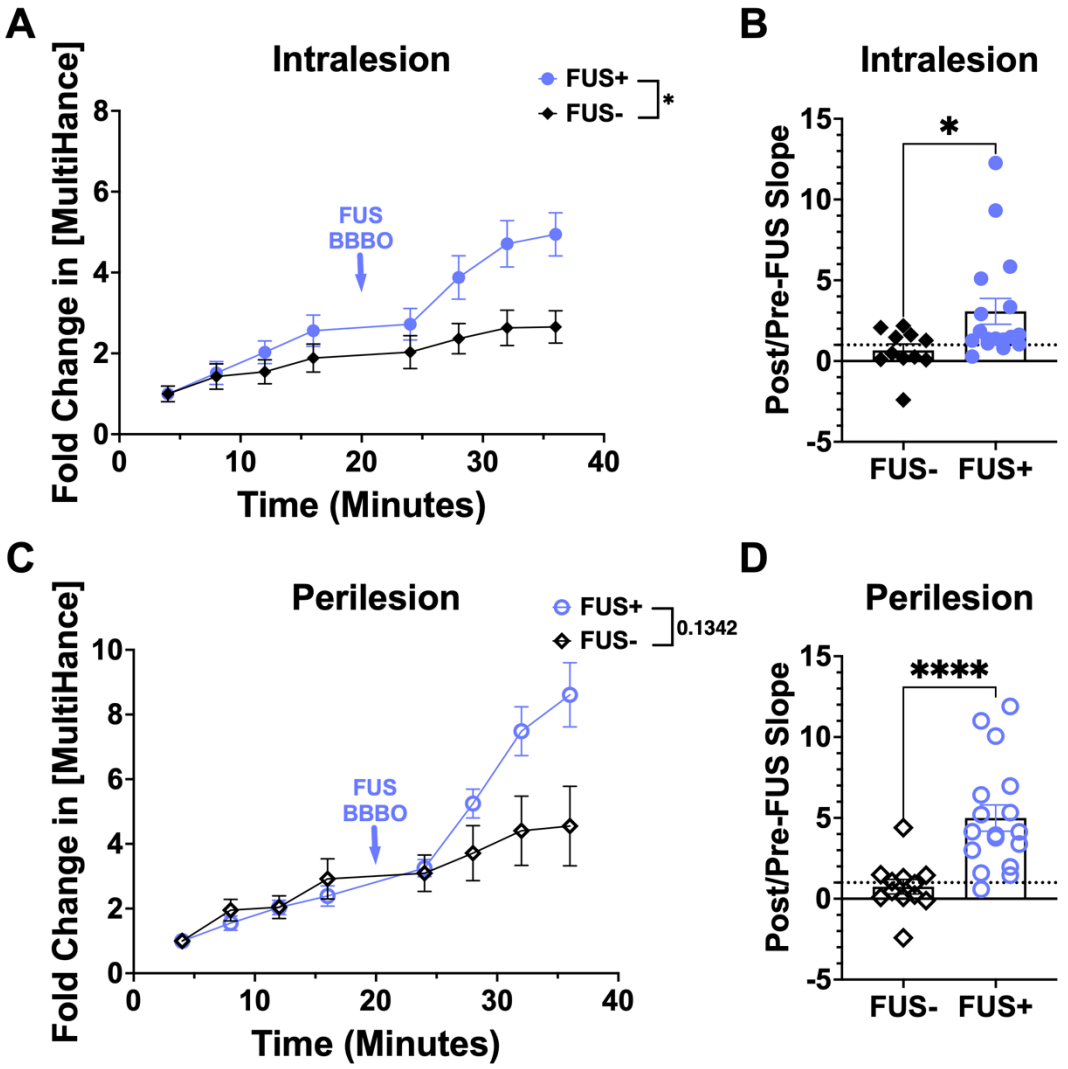

Figure 5.1. FUS BBBO Enhances Delivery Rate of MultiHance in CCMs. (A,C) Temporal fold change in MultiHance concentration over the average initial concentration for FUS- and FUS+ CCMs. Timepoints of 4, 8, 12, and 15 mins are prior to FUS BBBO. Timepoints of 24, 28, 32, and 36 mins are after FUS BBBO for FUS+ CCMs. (B,D) Comparison of the ratio of the slope of post-FUS time segments (24-36 mins) to the slope of pre-FUS time segments (4-15 mins) for MultiHance concentratation between FUS- and FUS+ CCMs. (A) Temporal fold change in MultiHance concentration for the CCM core (i.e. intralesion). Fold change in MultiHance concentration is significantly elevated for the FUS+ group relative to the FUS- group at 36 mins inside the CCM core. Repeated measures two-way ANOVA with Geisser-Greenhouse correction and Holm-Šidák's multiple comparisons test, p=0.0162. (B) Delivery rate in the CCM core is enhanced following FUS BBBO for FUS+ CCMs compared to FUS- CCMs. Mann-Whitney test, p=0.0221. (C) Temporal fold change in MultiHance concentration for the perilesional space. Fold change in MultiHance concentration exhibits trends towards enhancement for the FUS+ group relative to the FUS- group at 36 mins. Repeated

measures two-way ANOVA with Geisser-Greenhouse correction and Holm-Šidák's multiple comparisons test, $p=0.01342$. (D) Delivery rate in the perilesional space is enhanced following FUS BBBO for FUS+ CCMs compared to FUS- CCMs. Mann-Whitney test, $p<0.0001$.

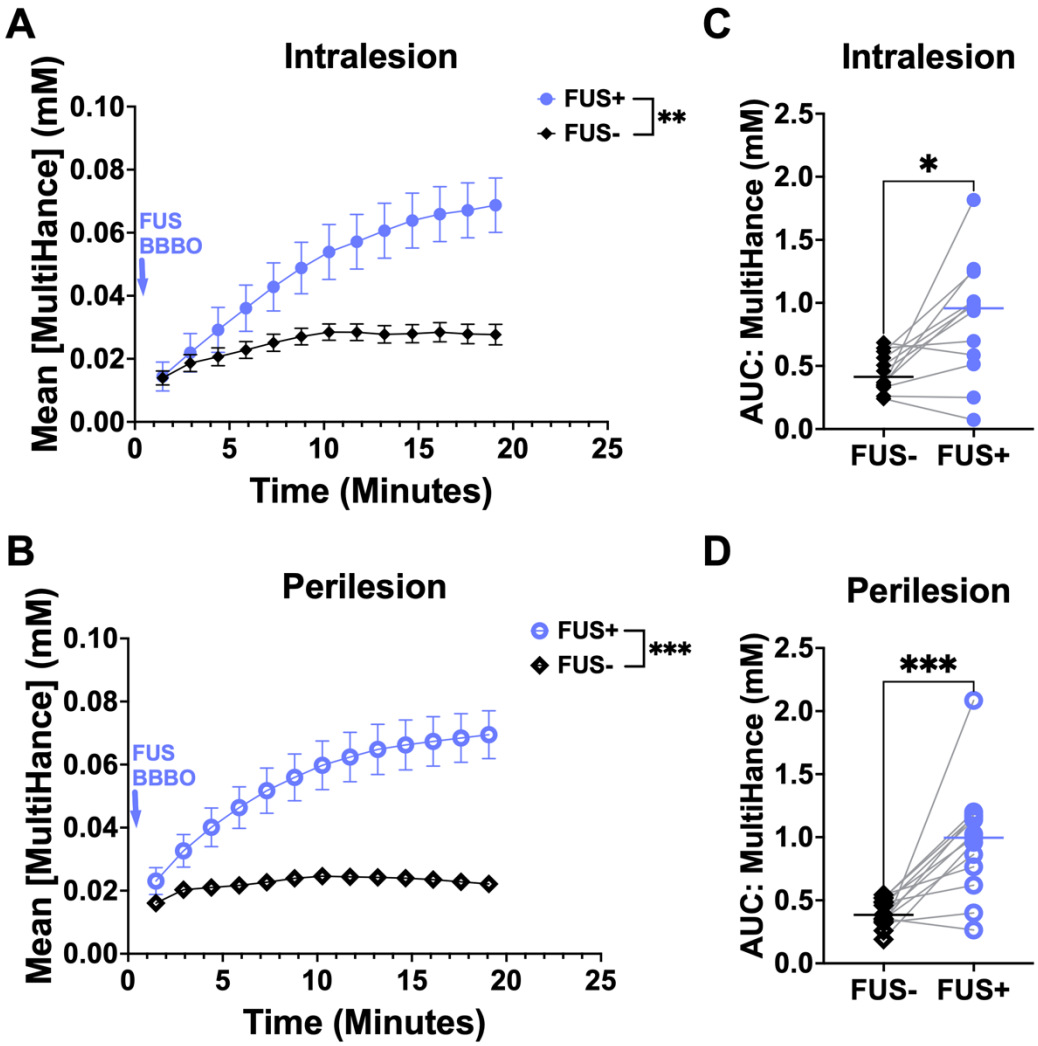

Figure 5.2. FUS BBBO Enhances Total Delivery of MultiHance in CCMs. (A, B) Temporal MultiHance concentration in the same CCMs without FUS or with FUS applied one day later. Temporal MultiHance concentration is significantly enhance 20 mins after FUS BBBO in the (A) intralesional and (B) perilesional spaces. Repeated measures two-way ANOVA with Geisser-Greenhouse correction and Holm-Šidák's multiple comparisons test; p=0.0070 and p=0.0005, respectively. (C,D) Area under the curve of the temporal data in (A,B) representing CCM tissue exposure to MultiHance. MultiHance exposure is significantly augmented with FUS BBBO in the (C) intralesional and (D) perilesional spaces. Wilcoxon matched-pairs signed rank test; p=0.0122 and p=0.0007, respectively.

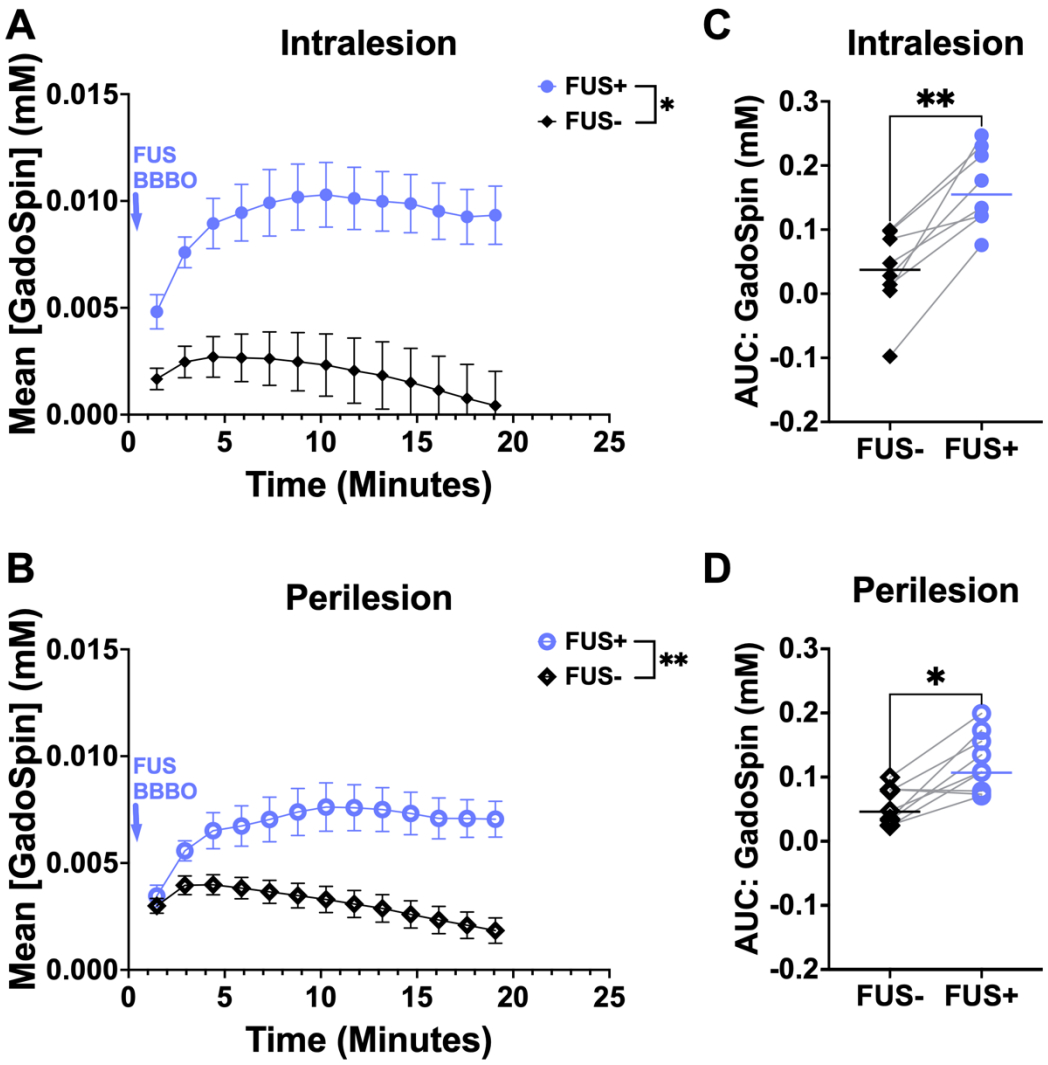

Figure 5.3. FUS BBBO Enhances Total Delivery of GadoSpin D in CCMs. (A, B) Temporal GadoSpin D concentration in the same CCMs without FUS or with FUS applied one day later. Temporal GadoSpin D concentration is significantly enhance 20 mins after FUS BBBO in the (A) intralesional and (B) perilesional spaces. Repeated measures two-way ANOVA with Geisser-Greenhouse correction and Holm-Šidák's multiple comparisons test; p=0.0106 and p=0.0021, respectively. (C,D) Area under the curve of the temporal data in (A,B) representing CCM tissue exposure to GadoSpin D . GadoSpin D exposure is significantly augmented with FUS BBBO in the (C) intralesional and (D) perilesional spaces. Wilcoxon matched-pairs signed rank test; p=0.0078 and p=0.0195, respectively.

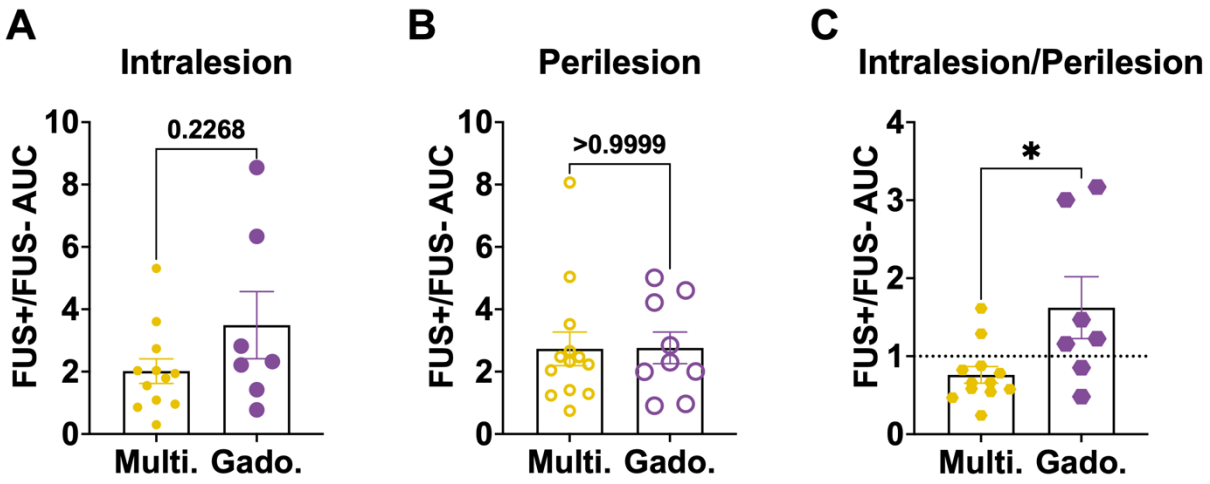

Figure 5.4. FUS BBBO Differentially Enhances Total Delivery Location for MultiHance versus GadoSpin D. (A-C) Comparison of the ratio of area under the curve analysis with FUS to without FUS for MultiHance versus GadoSpin D. (A) FUS BBBO augmented delivery trends towards increases in GadoSpin D delivery relative to MultiHance in the intralesional space. Mann-Whitney test, p=0.2268. (B) FUS BBBO augmented delivery is comparable in the perilesional space for MultiHance and GadoSpin D. Mann-Whitney test, p>0.9999. (C) Ratio of intralesion-to-perilesion FUS BBBO augmented delivery indicates a significant difference between MultiHance and GadoSpin D. A value less than 1 for MultiHance indicates preference in the perilesional space, and a value greater than 1 for GadoSpin D indicates a preference in the intralesional space. Mann-Whitney test, p=0.049.

5.7 Chapter 5 Supplemental Figure

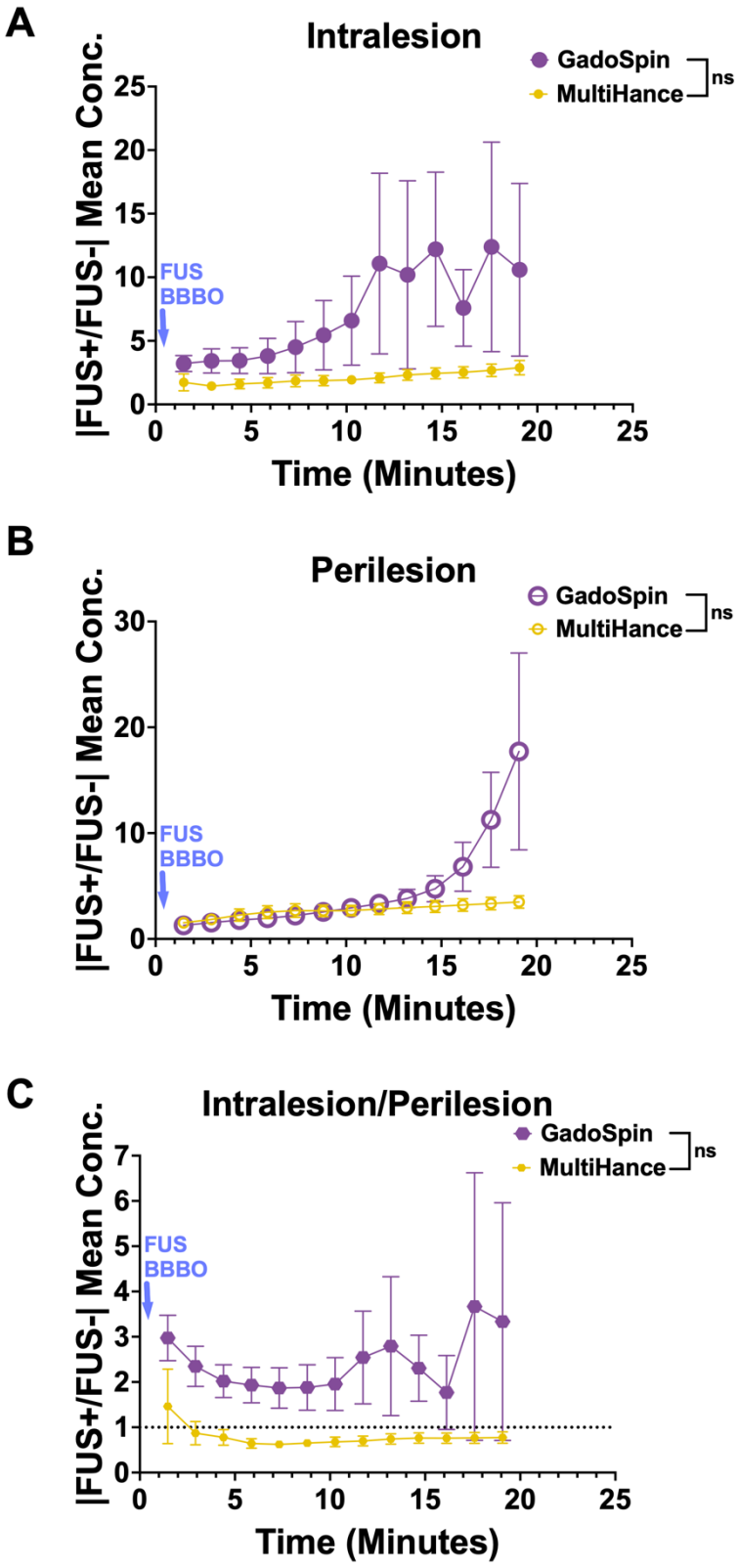

Figure 5.S1. Spatiotemporal effects of FUS BBBO augmented delivery for MultiHance and GadoSpin D. (A-C) Temporal magnitude of the ratio of the model drug mean concentration with FUS to without FUS. (A) GadoSpin D displays trends in increased augmented delivery with FUS BBBO compared to MultiHance in the (A) intralesional space and (B) perilesional space. Mixed-effects model with Geisser-Greenhouse correction and Holm-Šidák's multiple comparisons test; p=0.8348 and p=0.8850, respectively. (C) Ratio of intralesion-to-perilesion FUS BBBO augmented delivery indicates trends in GadoSpin D preference in the intralesional space and MultiHance preference in the perilesional space. Mixed-effects model with Geisser-Greenhouse correction and Holm-Šidák's multiple comparisons test; p=0.6500.

CHAPTER 6: FUTURE DIRECTIONS

6.1 Leverage Longitudinal MRI Data of *Krit1* Mouse Model to Enhance Characterization of CCM Dynamics

In Chapter 3 of this dissertation, we collected an extensive MRI dataset of our chronic CCM mouse model. This dataset encompasses volumetric, permeability, and susceptibility information for numerous CCMs over the lifespan of several CCM mice. Chapter 3 delved into several aspects of CCM dynamics using this dataset. However, there remains untapped potential within this MRI dataset to deepen our comprehension of CCMs. Moreover, in Chapter 4, we obtained volumetric MRIs at even more refined temporal intervals, and in Chapter 5, we acquired permeability MRIs over extended durations and with varying sizes of molecules. Together, these chapters contribute to a comprehensive dataset that allows for a deeper exploration of the poorly understood dynamics governing CCM stability.

6.1.1 Influence of Brain Region on CCM Dynamics

First, our dataset presents an opportunity to deepen our understanding of how brain location influences CCMs. As highlighted in Chapter 3, CCMs frequently manifest in brain regions such as the cerebellum, olfactory bulb, thalamus, cerebral cortex, brainstem, and periventricular striatum, suggesting a potential link between brain region and CCM formation. Notably, in patients, CCMs predominantly develop in white matter regions[132,133]. Interestingly, our MRI dataset suggests that brain regions may also influence the stability of these lesions. Of note, many of our most permeable CCMs in this study were located in the cerebellum and brainstem. In clinical cases, brainstem CCMs are also associated with a heightened risk of hemorrhage[10]. To explore the impact of brain region on CCM dynamics, we can employ recently developed algorithms from other research groups to automatically register our MRIs to brain atlases[134,135]. This approach facilitates an examination of how brain region influences CCM formation, growth,

and permeability, providing valuable insights that could inform decisions regarding the treatment of CCMs based on their specific location.

6.1.2 Predictive MRI Markers of CCM Formation and Stability

The longitudinal nature of this dataset provides the opportunity to assess markers that may predict CCM formation and stability. As CCM trajectory in patients is still poorly understood, identifying predictive markers using the existing MRI monitoring methods holds significant value. Indeed, several MRI methods have been deployed in patients with the goal of creating predictive models of CCM stability[11–14]. Leveraging the integration of artificial intelligence and medical imaging, the emerging field of radiomics involves mining medical images with sophisticated algorithms to enhance the information extracted from these images[136].

Applying radiomic approaches to our extensive MRI dataset collected across Chapters 3, 4, and 5 allows for the identification of imaging features not readily discernible through traditional analyses. Radiomic workflows can extract intricate features related to shape, intensity, and texture. For example, the radiomic features of skewness and kurtosis describe asymmetry and tailedness of the data intensity distribution[137]. Implementing a radiomic workflow on our CCM MRI dataset enables the development of models to predict indicators of CCM instability, including formation, growth, and hemorrhage, as well as indicators of stability such as volume regression and reduced permeability. Ultimately, these models could then be integrated into the clinical assessment of CCM patients and guide clinicians in determining the most effective course of treatment based on individualized predictions and characteristics.

6.2 Expand Evaluation of FUS BBBO for CCM Treatment

In Chapter 4, we presented evidence showcasing the therapeutic promise of FUS BBBO in our *Krit1* model of CCM. These findings are not only compelling but also raise numerous questions regarding the broader applicability and potential of FUS BBBO as a treatment option for CCM.

6.2.1 Therapeutic Potential of FUS BBBO in Diverse CCM Models

In Chapter 4, our investigation into the effects of FUS BBBO was centered on a chronic *Krit1* model of CCM. *KRIT1* mutation is the most prevalent mutation in familial cases of CCM[1]. However, familial cases also arise from mutations in *CCM2* and *PDCD10*. Additionally, approximately 80% of clinical CCM cases are comprised of sporadic cases[10]. To establish the broad effectiveness of FUS BBBO for all CCM patients, additional studies should be conducted applying this approach in other familial models and sporadic models of the disease.

Given the different functions of the three CCM genes, variations in the therapeutic benefits of FUS BBBO may occur. Clinically, *CCM2* mutation tends to result in a lower lesion burden and more asymptomatic cases[138]. Thus, we may anticipate similar results for *Ccm2* models as seen with our *Krit1* model. However, *PDCD10* mutation is known to impact more signaling pathways than that of *KRIT1* and *CCM2* and leads to a more aggressive disease presentation in patients[139–141]. Therefore, we could expect a reduced therapeutic potential in *Pdcd10* models. Moreover, the inclusion of the gain-of-function mutation of *Pik3ca* in the sporadic CCM mouse model developed by Mark Kahn's group, which mirrors the mutation found in biopsied CCMs from patients, introduces the potential for a more aggressive phenotype that could influence the therapeutic effects of FUS BBBO[42].

Exploring the impact of FUS BBBO in these diverse CCM models not only helps to validate its effectiveness across different genetic contexts but also sheds light on potential mechanistic variations underlying this therapeutic approach. In essence, expanding the application of FUS BBBO to various CCM models contributes to a more comprehensive understanding of its therapeutic potential for the diverse landscape of CCM presentations.

6.2.2 Application of FUS BBBO in Other CNS Locations for CCM

Our study in Chapter 4 targeted CCMs located in the caudoputamen, corpus callosum, and cerebral cortex, leveraging our expertise in targeting these specific brain regions and minimizing potential technical challenges arising in alternative locations. This strategic approach allowed us to concentrate on assessing the impact of FUS BBBO on CCM, rather than diverting attention to the optimization of FUS BBBO for various brain regions.

Now that we have established the therapeutic efficacy of FUS BBBO for CCM, it is imperative to broaden our investigation to encompass other locations within the CNS where cavernous malformations commonly manifest. Notably, cavernous malformations in the brainstem and spinal cord pose a critical need for non-invasive treatment options, given the heightened risks associated with surgical interventions in these regions[103,142,143]. Others in the FUS field have demonstrated the feasibility of targeting the brainstem and spinal cord in both rodent models and humans[144–147]. Further, Stefanyda Maslova of the Sheybani lab at UVA has recently developed a protocol for cerebellum/brainstem targeting with the same FUS equipment used in Chapter 4.

As brainstem and spinal cord cavernous malformation has dismal surgical outcomes, validating the feasibility and effectiveness of FUS BBBO in these regions holds substantial clinical significance. Additionally, as patients with brainstem and spinal cord lesions often lack viable surgical resection options[103], it is likely that the initial clinical applications of FUS BBBO would be

in patients with brainstem or spinal cord lesions. This expansion of our research scope not only broadens the potential clinical impact of FUS BBBO but also aligns with the urgent need for non-invasive treatment options in critical CNS locations.

6.2.3 Dose and Staging Optimization of FUS BBBO for CCM

In Chapter 4, we explored several treatment regimens of FUS BBBO, encompassing single and repeat sonications, along with a range of fixed and feedback-controlled PNPs. Meanwhile, other aspects of our treatments were more rigid. For instance, repeat sonications were consistently performed three days apart, aligning with the approximate half-life of antibodies in mice, and treatments in CCM mice were always initiated between two and three months of age.

Our findings indicated that PNP and the number of sonications correlated with the therapeutic effect of FUS BBBO. Thus, it would be worth exploring alternative dosing and staging strategies of FUS BBBO for CCM. It should be noted that, clinically, PCD-feedback control will be used to modulate the applied PNP during FUS BBBO[87,89–92,99]. Therefore, efforts of may be best focused on elucidating the optimal number and timing of treatments. Implementing logistically-feasible weekly or bi-weekly staged FUS BBBO sessions over one or two months could provide valuable insights into the cumulative effects of numerous treatments. Additionally, our study focused on treating mice when the lesion burden was moderate. However, investigating the potential of FUS BBBO in younger mice could shed light on its preventative effects. Finally, to uncover the full potential of this approach, FUS BBBO should be applied to a larger volume, potentially covering the entire brain area, and its impact on survival assessed. Notably, this study should be limited to animal models of CCM with only brain vasculature affected like those with brain-specific Cre promoters and the Kahn group's sporadic model. These comprehensive

investigations are poised to contribute significantly to the optimization of FUS BBBO protocols for CCM, ultimately maximizing its potential as a therapeutic option for patients with this condition.

6.2.4 Mechanistic Evaluation of FUS BBBO for CCM

We demonstrate in Chapter 4 that FUS BBBO arrests the growth of CCMs and can also reduce the formation of new CCMs. Despite these promising outcomes, the specific mechanisms contributing to these therapeutic effects were not fully elucidated. Understanding these mechanisms would enable informed optimization of our FUS BBBO parameters, dosing, and targeting. In the context of Alzheimer's disease, favorable bioeffects following FUS BBBO have been linked to increases in glial activation, neurogenesis, memory enhancement, endogenous antibody delivery, and clearance of amyloid beta plaques and tau[24,28,30,81–84]. Mechanical stimulation from microbubble cavitation during FUS BBBO is also postulated to induce beneficial signaling changes, which may be particularly impactful in the case of CCM.

To glean insight into the mechanisms underlying the therapeutic effects of FUS BBBO in CCM, studies could be conducted to survey mechanistic contributions from various sources. Temporal single-cell transcriptomics analyses could illuminate the changes in gene expression across different cell types induced by FUS BBBO and the persistence of these effects in CCM. Spatial transcriptomics could also uncover the influence of FUS BBBO on different regions of CCM brain tissue (i.e. lesion core, perilesional space, and lesion-free, *Krit1* mutated tissue). Investigations into the influence of FUS BBBO-modulated microglia/macrophages on therapeutic benefits could involve depleting these cells in CCM mice before FUS BBBO with PLX3397 or PLX5622, and comparing the outcomes to those in CCM mice with intact microglia/macrophage populations. Further, longitudinal changes in neuroinflammation following FUS BBBO could be conducted using positron emission tomography (PET) imaging of ^{18}F-DPA-714, a translocator

protein (TSPO) radiotracer known to bind microglia, macrophages, and astrocytes[148–151]. To explore the potential contribution of reduced blood byproducts to FUS BBBO therapeutic effects, studies could measure iron changes following the procedure. Quantitative susceptibility mapping (QSM) conducted longitudinally before and after FUS BBBO could monitor changes in iron induced by this approach[11,49,50]. Lastly, to examine the influence of FUS BBBO-induced mechanical stimulation on therapeutic effects for CCM, FUS BBBO parameters affecting cavitation could be studied. In Chapter 4, we found that PNP correlated with both growth control and reduced lesion formation, indicating that cavitation strength likely plays a pivotal role in therapeutic outcome. The effect of cavitation duration could also be studied through increases in either total sonication duration or burst length. However, increasing burst length may also elevate the risk of tissue heating[152,153]. Consequently, any studies involving increased burst length should be conducted at lower PNPs and incorporate MR thermometry to ensure safety.

In summary, a comprehensive understanding of the mechanistic underpinnings of the therapeutic effects induced by FUS BBBO holds the key to optimizing and effectively applying this approach for the treatment of CCM.

6.2.5 Features of CCM Responders/Non-Responders to FUS BBBO

Through Chapters 4 and 5, we have demonstrated that FUS BBBO can alter the growth, formation, and permeability of CCMs. In these studies, we establish that FUS BBBO is highly effective at CCM growth control, yet *de novo* CCM formation was only significantly reduced with fixed PNPs and repeat treatments. Additionally, Chapter 5 revealed that certain CCMs did not exhibit enhanced permeability following FUS BBBO, especially for MultiHance.

Understanding the factors that distinguish CCM responders from non-responders to FUS BBBO can help inform best practices for CCM targeting. The extensive MRI and

immunofluorescence images collected during these studies provide a rich dataset to identify features associated with responding and non-responding CCMs for each FUS BBBO effect (i.e. growth control, formation, and permeability). Various characteristics, such as initial CCM size, brain region, hypo/hyperintensity signals, initial CCM permeability, glia population, *Krit1* vasculature properties, and the presence of red blood cells, could be explored as potential markers of responsiveness.

Determining which features are indicative of a positive response to treatment can aid in strategically deploying FUS BBBO by guiding the selection of CCMs for targeting and informing decisions on timing or dosing of sonications. Identifying these features of responsiveness is crucial for advancing the precision and effectiveness of FUS BBBO as a treatment for CCM, and ultimately improving patient outcomes.

6.2.6 Delivery of Therapeutic Agents with FUS BBBO for CCM

In Chapter 4, we illustrated the beneficial impact of FUS BBBO in the absence of therapeutic delivery for CCMs. Building on this, in Chapter 5, we demonstrate that FUS BBBO can enhance the delivery of both 1 kDa and 17 kDa molecules. These studies indicate great promise for the therapeutic potential of FUS BBBO combined with pharmacological agents for treating CCM.

Snellings et al. details numerous drugs under investigation for CCM[1], with most in the preclinical stage and a few entering early-phase clinical trials. Notably, the majority of these drugs are small molecules, which—based on our results in Chapter 5—should experience improved delivery to the CCM lesion core and perilesional space with FUS BBBO. Future studies should investigate the beneficial outcomes of FUS BBBO in delivering promising CCM drugs compared to FUS BBBO or the drug alone.

The potential for synergistic effects between FUS BBBO and therapeutic drug delivery is compelling. The secondary bioeffects induced by FUS BBBO create a dynamic environment that could amplify the efficacy of concurrently delivered therapeutic agents. For instance, thrombospondin-1 has exhibited the ability to prevent CCM formation through angiogenesis inhibition[154]. If we hypothesize that FUS BBBO controls the growth of CCMs through glial activation and mechanical stimulation, the combination of these effects with angiogenesis regulation could create a potent correction in signaling changes across the neurovascular unit and neuroinflammatory populations. In parallel, computational models of signaling networks in CCM endothelial cells and astrocytes, generated by Tanya Cruz and Ishaan Shah of the Price lab, can inform the selection of drugs that may work best or synergize effectively with FUS BBBO.

Given the independent benefits of FUS BBBO for CCM, coupled with its adaptability to integrate with any number of drugs, this approach presents an unprecedented therapeutic potential for CCM. Exploration of specific drug-FUS BBBO combinations is warranted to unlock the full therapeutic potential of this innovative treatment strategy.

6.3 Deploy Quantitative MRI Techniques to Further Characterize FUS BBBO for CCM

Throughout Chapters 3, 4, and 5, a diverse array of MRI approaches is employed to comprehensively characterize CCMs and assess the influence of FUS BBBO on them. The non-invasive nature of these quantitative MRI techniques allows for longitudinal measurements of CCM dynamics, a crucial aspect given the heterogeneous behavior of CCMs even within the same mouse brain. The success and versatility of MRI in these studies warrant a deeper exploration of the impacts of FUS BBBO on CCMs.

6.3.1 Retention of FUS BBBO Delivered Molecules in CCMs

In Chapter 5, we use T1 mapping MRI to measure the acute enhancement of FUS BBBO delivery of MultiHance (1 kDa) and GadoSpin D (17 kDa) contrast agents to the lesion core and perilesional space of CCMs. While we observed enhanced delivery within the initial 20 minutes after contrast agent intravenous injection, the long-term impact of FUS BBBO on contrast agent concentration in the CCM microenvironment remains unknown for later timepoints following sonication and injection.

Our study in Chapter 5 demonstrated that the concentration of both contrast agents reaches a steady-state level within the 20 min time period. However, these studies did not illuminate when the concentration begins to decline in the lesion core or perilesional space following FUS BBBO. Intriguingly, the GadoSpin D concentration in the absence of FUS BBBO declined within these 20 mins, suggesting that FUS BBBO may augment the retention of the contrast agent. Therefore, future studies should measure the concentration of these molecules in the CCM microenvironment at later acute timepoints (e.g., 1 hr, 3 hr, 6 hr post-sonication and injection) to elucidate if FUS BBBO influences the clearance of molecules over an extended period. As this effect was not seen within the initial 20-min window for MultiHance, molecule size will likely influence this retention effect of FUS BBBO.

Understanding the retention and clearance dynamics of FUS BBBO-delivered molecules can provide insights into the secondary effects induced by FUS BBBO in CCMs and could also guide when repeat treatments of FUS BBBO should be conducted for different sized molecules.

6.3.2 Longitudinal Effect of FUS BBBO on Permeability

In Chapter 4, T1 mapping was not conducted during our longitudinal assessment of FUS BBBO in CCM mice. Consequently, the long-term impact of FUS BBBO on the permeability of CCMs remains elusive. Subsequent investigations should focus on measuring weekly changes in permeability within sonicated CCMs in comparison to non-sonicated CCMs after a single FUS BBBO treatment. Moreover, the effectiveness of repeat FUS BBBO in increasing permeability following each subsequent application is still unknown. CCMs may exhibit sensitization, tolerance, or remain neutral in terms of permeabilization following repeat FUS BBBO treatments. To explore this, prospective studies should incorporate T1 mapping after each repeat FUS BBBO application, tracking the degree of FUS-induced permeability for each treatment iteration. Additional studies could also investigate whether a specific staging of FUS BBBO is superior in enhancing acute permeability of CCMs for improved delivery while concurrently mitigating chronic permeability, which may be associated with an elevated risk of hemorrhage. Collectively, these studies would inform the staging of FUS BBBO for CCMs and further elucidate the long-term effects of FUS BBBO for CCMs.

6.3.3 Evaluation of Large Molecule Delivery with FUS BBBO in CCMs

In Chapter 5, we investigate the FUS BBBO enhancement of contrast agents with sizes of 1 kDa and 17 kDa in CCMs, corresponding to that of small molecules and small proteins. To broaden our understanding, future studies should explore the ability of FUS BBBO to enhance the delivery of molecules that are sized similarly to that of antibodies, viral vectors, and other nanocarriers. Unfortunately, T1 mapping may not facilitate the examination of the enhancement of these larger molecules. The contrast agents used for T1 mapping induce a measurable T1 relaxivity, typically through the incorporation of gadolinium molecules[73,93]. However, as these

molecules increase in size, the concentration of the gadolinium molecules decrease which also decreases the signal and ability to measure permeability with T1 mapping approaches.

To address this limitation, more sophisticated quantitative MRI techniques will need to be leveraged to enable the study of larger molecule delivery with FUS BBBO in CCMs. Promising alternatives include QSM or chemical exchange saturation transfer (CEST) MRI techniques[155–159]. Currently undergoing optimization by Matt Hoch of the Price lab, these advanced MRI techniques have the potential to elucidate whether FUS BBBO facilitates efficient delivery of antibody- and gene therapy-sized molecules to CCMs. Furthermore, these MRI techniques could also be deployed to inform parameter, dosing, and staging optimization of FUS BBBO for different sizes of molecules.

6.4 SUMMARY

This body of work showcases the successful adaptation of clinical MR imaging protocols to our CCM mouse model, enabling the design and evaluation of a novel therapy involving FUS BBBO for CCM. Our findings establish FUS BBBO as a promising treatment modality for CCM, revealing its potential to independently impede CCM growth and formation while also enhancing the delivery of therapeutic agents to the CCM microenvironment. Following future studies, we hope this technique can be confidently deployed in the clinic to offer a considerably more attractive and effective therapy for CCM patients.

REFERENCES

1. Snellings DA, Hong CC, Ren AA, Lopez-Ramirez MA, Girard R, Srinath A, Marchuk DA, Ginsberg MH, Awad IA, Kahn ML. Cerebral Cavernous Malformation: From Mechanism to Therapy. *Circ Res* [Internet]. 2021 [cited 2021 Oct 19];129:195–215. Available from: https://www.ahajournals.org/doi/abs/10.1161/CIRCRESAHA.121.318174

2. Awad IA, Polster SP. Cavernous angiomas: deconstructing a neurosurgical disease: JNSPG 75th Anniversary Invited Review Article. *J Neurosurg* [Internet]. 2019 [cited 2021 Oct 27];131:1–13. Available from: https://thejns.org/view/journals/j-neurosurg/131/1/article-p1.xml

3. Malinverno M, Maderna C, Abu Taha A, Corada M, Orsenigo F, Valentino M, Pisati F, Fusco C, Graziano P, Giannotta M, Yu QC, Zeng YA, Lampugnani MG, Magnusson PU, Dejana E. Endothelial cell clonal expansion in the development of cerebral cavernous malformations. *Nat Commun 2019 101* [Internet]. 2019 [cited 2021 Oct 27];10:1–16. Available from: https://www.nature.com/articles/s41467-019-10707-x

4. Detter MR, Snellings DA, Marchuk DA. Cerebral Cavernous Malformations Develop Through Clonal Expansion of Mutant Endothelial Cells. *Circ Res* [Internet]. 2018 [cited 2021 Oct 27];123:1143–1151. Available from: https://www.ahajournals.org/doi/abs/10.1161/CIRCRESAHA.118.313970

5. Salman RAS, Hall JM, Horne MA, Moultrie F, Josephson CB, Bhattacharya JJ, Counsell CE, Murray GD, Papanastassiou V, Ritchie V, Roberts RC, Sellar RJ, Warlow CP. Untreated clinical course of cerebral cavernous malformations: a prospective, population-based cohort study. *Lancet Neurol*. 2012;11:217–224.

6. Garcia RM, Oh T, Cole TS, Hendricks BK, Lawton MT. Recurrent brainstem cavernous malformations following primary resection: blind spots, fine lines, and the right-angle method. *J Neurosurg* [Internet]. 2020 [cited 2021 Oct 27];135:671–682. Available from: https://thejns.org/view/journals/j-neurosurg/135/3/article-p671.xml

7. Minimally Invasive Surgery - Angioma Alliance [Internet]. [cited 2021 Nov 8];Available from: https://www.angioma.org/cavernous-angioma-in-depth/surgery/minimally-invasive-surgery/

8. Willie JT, Malcolm JG, Stern MA, Lowder LO, Neill SG, Cabaniss BT, Drane DL, Gross RE. Safety and effectiveness of stereotactic laser ablation forepileptogenic cerebral cavernous malformations. *Epilepsia* [Internet]. 2019 [cited 2021 Nov 9];60:220. Available from: /pmc/articles/PMC6365175/

9. Al-Shahi R, Salman E, Berg MJ, Morrison ; Leslie, Awad IA. Hemorrhage From Cavernous Malformations of the Brain Definition and Reporting Standards. 2008 [cited 2021 Oct 27];Available from: http://stroke.ahajournals.org

10. Flemming KD, Lanzino G. Cerebral Cavernous Malformation: What a Practicing Clinician Should Know. *Mayo Clin Proc* [Internet]. 2020 [cited 2021 Oct 27];95:2005–2020. Available from: http://www.mayoclinicproceedings.org/article/S0025619619309966/fulltext

11. Girard R, Fam MD, Zeineddine HA, Tan H, Mikati AG, Shi C, Jesselson M, Shenkar R, Wu M, Cao Y, Hobson N, Larsson HBW, Christoforidis GA, Awad IA. Vascular permeability and iron deposition biomarkers in longitudinal follow-up of cerebral

cavernous malformations. *J Neurosurg* [Internet]. 2016 [cited 2021 Aug 31];127:102–110. Available from: https://thejns.org/view/journals/j-neurosurg/127/1/article-p102.xml

12. Hart BL, Taheri S, Rosenberg GA, Morrison LA. Dynamic Contrast-Enhanced MRI Evaluation of Cerebral Cavernous Malformations. *Transl Stroke Res 2013 45* [Internet]. 2013 [cited 2021 Aug 31];4:500–506. Available from: https://link.springer.com/article/10.1007/s12975-013-0285-y

13. Mikati AG, Tan H, Shenkar R, Li L, Zhang L, Guo X, Larsson HBW, Shi C, Liu T, Wang Y, Shah A, Edelman RR, Christoforidis G, Awad I. Dynamic Permeability and Quantitative Susceptibility. *Stroke* [Internet]. 2014 [cited 2021 Aug 31];45:598–601. Available from: https://www.ahajournals.org/doi/abs/10.1161/STROKEAHA.113.003548

14. Mikati AG, Khanna O, Zhang L, Girard R, Shenkar R, Guo X, Shah A, Larsson HB, Tan H, Li L, Wishnoff MS, Shi C, Christoforidis GA, Awad IA. Vascular Permeability in Cerebral Cavernous Malformations: *http://dx.doi.org/101038/jcbfm201598* [Internet]. 2015 [cited 2021 Aug 31];35:1632–1639. Available from: https://journals.sagepub.com/doi/10.1038/jcbfm.2015.98?url_ver=Z39.88-2003&rfr_id=ori%3Arid%3Acrossref.org&rfr_dat=cr_pub++0pubmed

15. Mainprize T, Lipsman N, Huang Y, Meng Y, Bethune A, Ironside S, Heyn C, Alkins R, Trudeau M, Sahgal A, Perry J, Hynynen K. Blood-Brain Barrier Opening in Primary Brain Tumors with Non-invasive MR-Guided Focused Ultrasound: A Clinical Safety and Feasibility Study. *Sci Rep* [Internet]. 2019;9:1–7. Available from: http://dx.doi.org/10.1038/s41598-018-36340-0

16. Idbaih A, Canney M, Belin L, Desseaux C, Vignot A, Bouchoux G, Asquier N, Law-Ye B, Leclercq D, Bissery A, De Rycke Y, Trosch C, Capelle L, Sanson M, Hoang-Xuan K, Dehais C, Houillier C, Laigle-Donadey F, Mathon B, André A, Lafon C, Chapelon J-Y, Delattre J-Y, Carpentier A. Safety and Feasibility of Repeated and Transient Blood-Brain Barrier Disruption by Pulsed Ultrasound in Patients with Recurrent Glioblastoma. *Clin Cancer Res* [Internet]. 2019;clincanres.3643.2018. Available from: http://clincancerres.aacrjournals.org/lookup/doi/10.1158/1078-0432.CCR-18-3643

17. Carpentier A, Canney M, Vignot A, Reina V, Beccaria K, Horodyckid C, Karachi C, Leclercq D, Lafon C, Chapelon J-Y, Capelle L, Cornu P, Sanson M, Hoang-Xuan K, Delattre J-Y, Idbaih A. Clinical trial of blood-brain barrier disruption by pulsed ultrasound. *Sci Transl Med* [Internet]. 2016 [cited 2019 Jul 2];8:343re2-343re2. Available from: https://stm.sciencemag.org/content/8/343/343re2.abstract

18. Lipsman N, Meng Y, Bethune AJ, Huang Y, Lam B, Masellis M, Herrmann N, Heyn C, Aubert I, Boutet A, Smith GS, Hynynen K, Black SE. Blood-brain barrier opening in Alzheimer's disease using MR-guided focused ultrasound. *Nat Commun* [Internet]. 2018 [cited 2018 Sep 4];9:2336. Available from: http://www.ncbi.nlm.nih.gov/pubmed/30046032

19. Agrawal M, Saraf S, Saraf S, Antimisiaris SG, Chougule MB, Shoyele SA, Alexander A. Nose-to-brain drug delivery: An update on clinical challenges and progress towards approval of anti-Alzheimer drugs. *J Control Release* [Internet]. 2018;281:139–177. Available from: https://doi.org/10.1016/j.jconrel.2018.05.011

20. Gänger S, Schindowski K. Tailoring Formulations for Intranasal Nose-to-Brain Delivery: A Review on Architecture, Physico-Chemical Characteristics and Mucociliary Clearance of the Nasal Olfactory Mucosa. *Pharmaceutics*. 2018;10:116.

21. Jackson S, George RT, Lodge MA, Piotrowski A, Wahl RL, Gujar SK, Grossman SA. The effect of regadenoson on the integrity of the human blood–brain barrier, a pilot study. *J Neurooncol*. 2017;132:513–519.

22. Jackson S, Weingart J, Nduom EK, Harfi TT, George RT, McAreavey D, Ye X, Anders NM, Peer C, Figg WD, Gilbert M, Rudek MA, Grossman SA. The effect of an adenosine A2A agonist on intra-tumoral concentrations of temozolomide in patients with recurrent glioblastoma. *Fluids Barriers CNS* [Internet]. 2018;15:1–9. Available from: https://doi.org/10.1186/s12987-017-0088-8

23. Prados MD, Schold SC, Fine HA, Jaeckle K, Mechtler L, Fetell MR, Phuphanich S, Feun L, Janus J, Ford K, Graney W. Administered Intravenously for the Treatment of Recurrent Malignant Glioma 1. *Neuro Oncol*. 2003;96–103.

24. Todd N, Angolano C, Ferran C, Devor A, Borsook D, McDannold N. Secondary effects on brain physiology caused by focused ultrasound-mediated disruption of the blood–brain barrier. *J Control Release*. 2020;324:450–459.

25. Gorick CM, Breza VR, Nowak KM, Cheng VWT, Fisher DG, Debski AC, Hoch MR, Demir ZEF, Tran NM, Schwartz MR, Sheybani ND, Price RJ. Applications of focused ultrasound-mediated blood-brain barrier opening. *Adv Drug Deliv Rev*. 2022;191:114583.

26. Scarcelli T, Jordão JF, O'reilly MA, Ellens N, Hynynen K, Aubert I. Stimulation of hippocampal neurogenesis by transcranial focused ultrasound and microbubbles in adult mice. *Brain Stimul* [Internet]. 2014 [cited 2023 Nov 22];7:304. Available from: /pmc/articles/PMC4103630/

27. Shin J, Kong C, Lee J, Choi BY, Sim J, Koh CS, Park M, Na YC, Suh SW, Chang WS, Chang JW. Focused ultrasound-induced blood-brain barrier opening improves adult hippocampal neurogenesis and cognitive function in a cholinergic degeneration dementia rat model. *Alzheimers Res Ther* [Internet]. 2019 [cited 2023 Nov 22];11. Available from: https://pubmed.ncbi.nlm.nih.gov/31881998/

28. Jordão JF, Thévenot E, Markham-Coultes K, Scarcelli T, Weng YQ, Xhima K, O'Reilly M, Huang Y, McLaurin JA, Hynynen K, Aubert I. Amyloid-β plaque reduction, endogenous antibody delivery and glial activation by brain-targeted, transcranial focused ultrasound. *Exp Neurol*. 2013;248:16–29.

29. Karakatsani ME, Kugelman T, Ji R, Murillo M, Wang S, Niimi Y, Small SA, Duff KE, Konofagou EE. Unilateral Focused Ultrasound-Induced Blood-Brain Barrier Opening Reduces Phosphorylated Tau from The rTg4510 Mouse Model. *Theranostics* [Internet]. 2019 [cited 2023 Nov 22];9:5396. Available from: /pmc/articles/PMC6691580/

30. Leinenga G, Götz J. Scanning ultrasound removes amyloid-b and restores memory in an Alzheimer's disease mouse model. *Sci Transl Med*. 2015;7.

31. Chesnut A. Focused Ultrasound Foundation State of the Field Report 2021. 2021;

32. Al-Holou WN, O'Lynnger TM, Pandey AS, Gemmete JJ, Thompson BG, Muraszko KM, Garton HJL, Maher CO. Natural history and imaging prevalence of cavernous malformations in children and young adults: Clinical article. *J Neurosurg Pediatr* [Internet]. 2012 [cited 2022 Oct 5];9:198–205. Available from: https://thejns.org/pediatrics/view/journals/j-neurosurg-pediatr/9/2/article-p198.xml

33. Ene C, Kaul A, Kim L. Natural history of cerebral cavernous malformations. *Handb Clin Neurol* [Internet]. 2017 [cited 2023 Nov 22];143:227–232. Available from: https://pubmed.ncbi.nlm.nih.gov/28552144/

34. Vernooij MW, Ikram MA, Tanghe HL, Vincent AJPE, Hofman A, Krestin GP, Niessen WJ, Breteler MMB, van der Lugt A. Incidental findings on brain MRI in the general population. *N Engl J Med* [Internet]. 2007 [cited 2023 Nov 22];357:1821–1828. Available from: https://pubmed.ncbi.nlm.nih.gov/17978290/

35. Chan AC, Drakos SG, Ruiz OE, Smith ACH, Gibson CC, Ling J, Passi SF, Stratman AN, Sacharidou A, Revelo MP, Grossmann AH, Diakos NA, Davis GE, Metzstein MM, Whitehead KJ, Li DY. Mutations in 2 distinct genetic pathways result in cerebral cavernous malformations in mice. *J Clin Invest* [Internet]. 2011 [cited 2022 Mar 16];121:1871–1881. Available from: http://www.jci.org

36. Kleaveland B, Zheng X, Liu JJ, Blum Y, Tung JJ, Zou Z, Chen M, Guo L, Lu MM, Zhou D, Kitajewski J, Affolter M, Ginsberg MH, Kahn ML. Regulation of cardiovascular development and integrity by the heart of glass-cerebral cavernous malformation protein pathway. *Nat Med* [Internet]. 2009 [cited 2023 Nov 22];15:169–176. Available from: https://pubmed.ncbi.nlm.nih.gov/19151727/

37. Whitehead KJ, Plummer NW, Adams JA, Marchuk DA, Li DY. Ccm1 is required for arterial morphogenesis: implications for the etiology of human cavernous malformations. *Development* [Internet]. 2004 [cited 2022 Mar 16];131:1437–1448. Available from: https://journals.biologists.com/dev/article/131/6/1437/64462/Ccm1-is-required-for-arterial-morphogenesis

38. Akers A, Al-Shahi Salman R, Awad IA, Dahlem K, Flemming K, Hart B, Kim H, Jusue-Torres I, Kondziolka D, Lee C, Morrison L, Rigamonti D, Rebeiz T, Tournier-Lasserve E, Waggoner D, Whitehead K, Yashar M, Kalani S, Tamargo RJ. Synopsis of Guidelines for the Clinical Management of Cerebral Cavernous Malformations: Consensus Recommendations Based on Systematic Literature Review by the Angioma Alliance Scientific Advisory Board Clinical Experts Panel. *Neurosurgery* [Internet]. 2017 [cited 2023 Nov 22];80:665–680. Available from: https://pubmed.ncbi.nlm.nih.gov/28387823/

39. Günel M, Awad IA, Finberg K, Anson JA, Steinberg GK, Batjer HH, Kopitnik TA, Morrison L, Giannotta SL, Nelson-Williams C, Lifton RP. A founder mutation as a cause of cerebral cavernous malformation in Hispanic Americans. *N Engl J Med* [Internet]. 1996 [cited 2023 Nov 22];334:946–951. Available from: https://pubmed.ncbi.nlm.nih.gov/8596595/

40. Yadla S, Jabbour PM, Shenkar R, Shi C, Camp bell PG, Awad IA. Cerebral cavernous malformations as a disease of vascular permeability: from bench to bedside with caution. *Neurosurg Focus* [Internet]. 2010 [cited 2023 Nov 22];29:1–7. Available from: https://pubmed.ncbi.nlm.nih.gov/20809762/

41. McDonald DA, Shi C, Shenkar R, Gallione CJ, Akers AL, Li S, De Castro N, Berg MJ, Corcoran DL, Awad IA, Marchuk DA. Lesions from patients with sporadic cerebral cavernous malformations harbor somatic mutations in the CCM genes: evidence for a common biochemical pathway for CCM pathogenesis. *Hum Mol Genet* [Internet]. 2014 [cited 2023 Nov 22];23:4357–4370. Available from: https://pubmed.ncbi.nlm.nih.gov/24698976/

42. Ren AA, Snellings DA, Su YS, Hong CC, Castro M, Tang AT, Detter MR, Hobson N,

Girard R, Romanos S, Lightle R, Moore T, Shenkar R, Benavides C, Beaman MM, Müller-Fielitz H, Chen M, Mericko P, Yang J, Sung DC, Lawton MT, Ruppert JM, Schwaninger M, Körbelin J, Potente M, Awad IA, Marchuk DA, Kahn ML. PIK3CA and CCM mutations fuel cavernomas through a cancer-like mechanism. *Nat 2021 5947862* [Internet]. 2021 [cited 2022 May 9];594:271–276. Available from: https://www.nature.com/articles/s41586-021-03562-8

43. Denier C, Labauge P, Brunereau L, Cavé-Riant F, Marchelli F, Arnoult M, Cecillon M, Maciazek J, Joutel A, Tournier-Lasserve E. Clinical features of cerebral cavernous malformations patients with KRIT1 mutations. *Ann Neurol* [Internet]. 2004 [cited 2022 May 9];55:213–220. Available from: https://pubmed.ncbi.nlm.nih.gov/14755725/

44. Gault J, Sain S, Hu LJ, Awad IA. Spectrum of genotype and clinical manifestations in cerebral cavernous malformations. *Neurosurgery* [Internet]. 2006 [cited 2022 May 9];59:1278–1284. Available from: https://pubmed.ncbi.nlm.nih.gov/17277691/

45. Gianfrancesco F, Cannella M, Martino T, Maglione V, Esposito T, Innocenzi G, Vitale E, Liquori CL, Marchuk DA, Squitieri F. Highly variable penetrance in subjects affected with cavernous cerebral angiomas (CCM) carrying novel CCM1 and CCM2 mutations. *Am J Med Genet B Neuropsychiatr Genet* [Internet]. 2007 [cited 2022 May 9];144B:691–695. Available from: https://pubmed.ncbi.nlm.nih.gov/17440989/

46. Weng J, Yang Y, Song D, Huo R, Li H, Chen Y, Nam Y, Zhou Q, Jiao Y, Fu W, Yan Z, Wang J, Xu H, Di L, Li J, Wang S, Zhao J, Wang J, Cao Y. Somatic MAP3K3 mutation defines a subclass of cerebral cavernous malformation. *Am J Hum Genet* [Internet]. 2021 [cited 2022 May 9];108:942–950. Available from: https://pubmed.ncbi.nlm.nih.gov/33891857/

47. Hong T, Xiao X, Ren J, Cui B, Zong Y, Zou J, Kou Z, Jiang N, Meng G, Zeng G, Shan Y, Wu H, Chen Z, Liang J, Xiao X, Tang J, Wei Y, Ye M, Sun L, Li G, Hu P, Hui R, Zhang H, Wang Y. Somatic MAP3K3 and PIK3CA mutations in sporadic cerebral and spinal cord cavernous malformations. *Brain* [Internet]. 2021 [cited 2022 May 9];144:2648–2658. Available from: https://pubmed.ncbi.nlm.nih.gov/33729480/

48. Tan H, Zhang L, Mikati AG, Girard R, Khanna O, Fam MD, Liu T, Wang Y, Edelman RR, Christoforidis G, Awad IA. Quantitative Susceptibility Mapping in Cerebral Cavernous Malformations: Clinical Correlations. *AJNR Am J Neuroradiol* [Internet]. 2016 [cited 2022 May 9];37:1209–1215. Available from: https://pubmed.ncbi.nlm.nih.gov/26965464/

49. Zeineddine HA, Girard R, Cao Y, Hobson N, Fam MD, Stadnik A, Tan H, Shen J, Chaudagar K, Shenkar R, Thompson RE, McBee N, Hanley D, Carroll T, Christoforidis GA, Awad IA. Quantitative susceptibility mapping as a monitoring biomarker in cerebral cavernous malformations with recent hemorrhage. *J Magn Reson Imaging* [Internet]. 2018 [cited 2022 May 9];47:1133–1138. Available from: https://pubmed.ncbi.nlm.nih.gov/28791783/

50. Girard R, Li Y, Stadnik A, Shenkar R, Hobson N, Romanos S, Srinath A, Moore T, Lightle R, Shkoukani A, Akers A, Carroll T, Christoforidis GA, Koenig JI, Lee C, Piedad K, Greenberg SM, Kim H, Flemming KD, Ji Y, Awad IA. A Roadmap for Developing Plasma Diagnostic and Prognostic Biomarkers of Cerebral Cavernous Angioma With Symptomatic Hemorrhage (CASH). *Neurosurgery* [Internet]. 2021 [cited 2023 Nov 22];88:686. Available from: /pmc/articles/PMC7884145/

51. Sone JY, Hobson N, Srinath A, Romanos SG, Li Y, Carrión-Penagos J, Shkoukani A, Stadnik A, Piedad K, Lightle R, Moore T, DeBiasse D, Bi D, Shenkar R, Carroll T, Ji Y, Girard R, Awad IA. Perfusion and Permeability MRI Predicts Future Cavernous Angioma Hemorrhage and Growth. *J Magn Reson Imaging* [Internet]. 2022 [cited 2023 Nov 22];55:1440. Available from: /pmc/articles/PMC8942875/

52. Cardoso C, Arnould M, De Luca C, Otten C, Abdelilah-Seyfried S, Heredia A, Leutenegger AL, Schwaninger M, Tournier-Lasserve E, Boulday G. Novel Chronic Mouse Model of Cerebral Cavernous Malformations. *Stroke* [Internet]. 2020 [cited 2021 Feb 11];51:1272–1278. Available from: https://pubmed.ncbi.nlm.nih.gov/31992178/

53. Detter MR, Shenkar R, Benavides CR, Neilson CA, Moore T, Lightle R, Hobson N, Shen L, Cao Y, Girard R, Zhang D, Griffin E, Gallione CJ, Awad IA, Marchuk DA. Novel Murine Models of Cerebral Cavernous Malformations. *Angiogenesis* [Internet]. 2020 [cited 2021 Feb 11];23:651–666. Available from: https://pubmed.ncbi.nlm.nih.gov/32710309/

54. DiStefano P V., Glading AJ. VEGF signalling enhances lesion burden in KRIT1 deficient mice. *J Cell Mol Med* [Internet]. 2020 [cited 2022 May 5];24:632–639. Available from: https://onlinelibrary.wiley.com/doi/full/10.1111/jcmm.14773

55. Mleynek TM, Chan AC, Redd M, Gibson CC, Davis CT, Shi DS, Chen T, Carter KL, Ling J, Blanco R, Gerhardt H, Whitehead K, Li DY. Lack of CCM1 induces hypersprouting and impairs response to flow. *Hum Mol Genet* [Internet]. 2014 [cited 2021 Feb 12];23:6223–6234. Available from: https://academic.oup.com/hmg/article/23/23/6223/2900816

56. Gibson CC, Zhu W, Davis CT, Bowman-Kirigin JA, Chan AC, Ling J, Walker AE, Goitre L, Monache SD, Retta SF, Shiu YTE, Grossmann AH, Thomas KR, Donato AJ, Lesniewski LA, Whitehead KJ, Li DY. Strategy for identifying repurposed drugs for the treatment of cerebral cavernous malformation. *Circulation* [Internet]. 2015 [cited 2023 Nov 22];131:289–299. Available from: https://pubmed.ncbi.nlm.nih.gov/25486933/

57. Claxton S, Kostourou V, Jadeja S, Chambon P, Hodivala-Dilke K, Fruttiger M. Efficient, inducible Cre-recombinase activation in vascular endothelium. *Genesis* [Internet]. 2008 [cited 2023 Nov 22];46:74–80. Available from: https://pubmed.ncbi.nlm.nih.gov/18257043/

58. Mugler JP. Optimized three-dimensional fast-spin-echo MRI. *J Magn Reson Imaging* [Internet]. 2014 [cited 2022 Mar 20];39:745–767. Available from: https://onlinelibrary.wiley.com/doi/full/10.1002/jmri.24542

59. Mugler JP, Bao S, Mulkern R V., Guttmann CRG, Robertson RL, Jolesz FA, Brookeman JR. Optimized single-slab three-dimensional spin-echo MR imaging of the brain. *Radiology* [Internet]. 2000 [cited 2023 Nov 22];216:891–899. Available from: https://pubmed.ncbi.nlm.nih.gov/10966728/

60. Liang L, Korogi Y, Sugahara T, Shigematsu Y, Okuda T, Ikushima I, Takahashi M. Detection of Intracranial Hemorrhage with Susceptibility-Weighted MR Sequences. *AJNR Am J Neuroradiol*. 1999;20:1527–1534.

61. Wang KY, Idowu OR, Lin DDM. Radiology and imaging for cavernous malformations. *Handb Clin Neurol*. 2017;143:249–266.

62. Labauge P, Laberge S, Brunereau L, Levy C, Tournier-Lasserve E. Hereditary cerebral

cavernous angiomas: clinical and genetic features in 57 French families. *Lancet*. 1998;352:1892–1897.

63. Rigamonti D, Hadley MN, Drayer BP, Johnson PC, Hoenig-Rigamonti K, Knight JT, Spetzler RF. Cerebral Cavernous Malformations. *http://dx.doi.org/101056/NEJM198808113190605* [Internet]. 2010 [cited 2022 Oct 5];170:59. Available from: https://www.nejm.org/doi/full/10.1056/NEJM198808113190605

64. Greenberg SM, Vernooij MW, Cordonnier C, Viswanathan A, Al-Shahi Salman R, Warach S, Launer LJ, Van Buchem MA, Breteler MM. Cerebral Microbleeds: A Field Guide to their Detection and Interpretation. *Lancet Neurol* [Internet]. 2009 [cited 2022 Mar 22];8:165. Available from: /pmc/articles/PMC3414436/

65. Hudnall R, Chen EX, Opperman PJ, Kelly S, Cramer JA, Surdell DL. A series of 14 representative presentations of cerebral cavernous malformations. *Interdiscip Neurosurg*. 2021;26:101298.

66. Tofts PS, Kermode AG. Measurement of the blood-brain barrier permeability and leakage space using dynamic MR imaging. 1. Fundamental concepts. *Magn Reson Med* [Internet]. 1991 [cited 2022 Apr 6];17:357–367. Available from: https://onlinelibrary.wiley.com/doi/full/10.1002/mrm.1910170208

67. Hylton N. Dynamic contrast-enhanced magnetic resonance imaging as an imaging biomarker. *J Clin Oncol*. 2006;24:3293–3298.

68. Labauge P, Denier C, Bergametti F, Tournier-Lasserve E. Genetics of cavernous angiomas. *Lancet Neurol*. 2007;6:237–244.

69. Morrison L, Akers A;, Adam MP, Mirzaa GM, Pagon RA. Cerebral Cavernous Malformation, Familial. 2003;1993–2022.

70. Pozzati E, Acciarri N, Tognetti F, Marliani F, Giangaspero F. Growth, Subsequent Bleeding, and De Novo Appearance of Cerebral Cavernous Angiomas. *Neurosurgery* [Internet]. 1996;38. Available from: https://journals.lww.com/neurosurgery/Fulltext/1996/04000/Growth,_Subsequent_Bleeding,_and_De_Novo.6.aspx

71. Shenkar R, Venkatasubramanian PN, Wyrwicz AM, Zhao JC, Shi C, Akers A, Marchuk DA, Awad IA. ADVANCED MAGNETIC RESONANCE IMAGING OF CEREBRAL CAVERNOUS MALFORMATIONSPART II. IMAGING OF LESIONS IN MURINE MODELS. *Neurosurgery* [Internet]. 2008 [cited 2022 Mar 16];63:790–798. Available from: https://academic.oup.com/neurosurgery/article/63/4/790/2558370

72. Lopez-Ramirez MA, Lai CC, Soliman SI, Hale P, Pham A, Estrada EJ, McCurdy S, Girard R, Verma R, Moore T, Lightle R, Hobson N, Shenkar R, Poulsen O, Haddad GG, Daneman R, Gongol B, Sun H, Lagarrigue F, Awad IA, Ginsberg MH. Astrocytes propel neurovascular dysfunction during cerebral cavernous malformation lesion formation. *J Clin Invest* [Internet]. 2021 [cited 2023 Nov 22];131. Available from: https://doi.org/10.1172/JCI139570DS1

73. Fram EK, Herfkens RJ, Johnson GA, Glover GH, Karis JP, Shimakawa A, Perkins TG, Pelc NJ. Rapid calculation of T1 using variable flip angle gradient refocused imaging. *Magn Reson Imaging* [Internet]. 1987 [cited 2023 Nov 22];5:201–208. Available from:

https://pubmed.ncbi.nlm.nih.gov/3626789/

74. Tanriover G, Sozen B, Seker A, Kilic T, Gunel M, Demir N. Ultrastructural analysis of vascular features in cerebral cavernous malformations. *Clin Neurol Neurosurg* [Internet]. 2013 [cited 2023 Jan 18];115:438–444. Available from: https://pubmed.ncbi.nlm.nih.gov/22776801/

75. Wei S, Li Y, Polster SP, Shen L, Weber CR, Awad IA. Cerebral Cavernous Malformation Proteins in Barrier Maintenance and Regulation. *Int J Mol Sci 2020, Vol 21, Page 675* [Internet]. 2020 [cited 2023 Jan 18];21:675. Available from: https://www.mdpi.com/1422-0067/21/2/675/htm

76. Zabramski JM, Wascher TM, Spetzler RF, Johnson B, Golfinos J, Drayer BP, Brown B, Rigamonti D, Brown G. The natural history of familial cavernous malformations: results of an ongoing study. *J Neurosurg* [Internet]. 1994 [cited 2022 Jul 29];80:422–432. Available from: https://thejns.org/view/journals/j-neurosurg/80/3/article-p422.xml

77. Girard R, Zeineddine HA, Koskimäki J, Fam MD, Cao Y, Shi C, Moore T, Lightle R, Stadnik A, Chaudagar K, Polster S, Shenkar R, Duggan R, Leclerc D, Whitehead KJ, Li DY, Awad IA. Plasma Biomarkers of Inflammation and Angiogenesis Predict Cerebral Cavernous Malformation Symptomatic Hemorrhage or Lesional Growth. *Circ Res* [Internet]. 2018 [cited 2022 Jan 20];122:1716. Available from: /pmc/articles/PMC5993629/

78. White E, Broad M, Myhre S, Serafini MR, Chestnut A, Browning M, Heishman D, Knupp J, Andreae T, Chao JC. 2022 State of the Field Report. *Focus Ultrasound Found* [Internet]. 2022 [cited 2023 Jan 18];Available from: www.fusfoundation.org

79. Fisher DG, Price RJ. Recent Advances in the Use of Focused Ultrasound for Magnetic Resonance Image-Guided Therapeutic Nanoparticle Delivery to the Central Nervous System. *Front Pharmacol* [Internet]. 2019 [cited 2023 Jan 18];10. Available from: https://pubmed.ncbi.nlm.nih.gov/31798453/

80. Timbie KF, Mead BP, Price RJ. Drug and gene delivery across the blood-brain barrier with focused ultrasound. *J Control Release* [Internet]. 2015;219:61–75. Available from: https://doi.org/10.1016/j.jconrel.2015.08.059

81. Park SH, Baik K, Jeon S, Chang WS, Ye BS, Chang JW. Extensive frontal focused ultrasound mediated blood–brain barrier opening for the treatment of Alzheimer's disease: a proof-of-concept study. *Transl Neurodegener*. 2021;10.

82. Schaeffer V, Lavenir I, Ozcelik S, Tolnay M, Winkler DT, Goedert M. Stimulation of autophagy reduces neurodegeneration in a mouse model of human tauopathy. *Brain*. 2012;135:2169–2177.

83. Lee Y, Choi Y, Park EJ, Kwon S, Kim H, Lee JY, Lee DS. Improvement of glymphatic–lymphatic drainage of beta-amyloid by focused ultrasound in Alzheimer's disease model. *Sci Rep*. 2020;10.

84. Leinenga G, Koh WK, Götz J. Scanning ultrasound in the absence of blood-brain barrier opening is not sufficient to clear β-amyloid plaques in the APP23 mouse model of Alzheimer's disease. *Brain Res Bull*. 2019;153:8–14.

85. Chernaya O, Zhurikhina A, Hladyshau S, Pilcher W, Young KM, Ortner J, Andra V,

Sulchek TA, Tsygankov D. Biomechanics of Endothelial Tubule Formation Differentially Modulated by Cerebral Cavernous Malformation Proteins. *iScience* [Internet]. 2018 [cited 2023 Nov 2];9:347. Available from: /pmc/articles/PMC6240601/

86. Stockton RA, Shenkar R, Awad IA, Ginsberg MH. Cerebral cavernous malformations proteins inhibit Rho kinase to stabilize vascular integrity. *J Exp Med* [Internet]. 2010 [cited 2023 Nov 3];207:881–896. Available from: www.jem.org/cgi/doi/10.1084/jem.20091258

87. Novell A, Kamimura HAS, Cafarelli A, Gerstenmayer M, Flament J, Valette J, Agou P, Conti A, Selingue E, Aron Badin R, Hantraye P, Larrat B. A new safety index based on intrapulse monitoring of ultra-harmonic cavitation during ultrasound-induced blood-brain barrier opening procedures. *Sci Rep* [Internet]. 2020 [cited 2023 Nov 2];10. Available from: /pmc/articles/PMC7308405/

88. Haqshenas SR, Saffari N. Multi-resolution analysis of passive cavitation detector signals. *J Phys Conf Ser* [Internet]. 2015 [cited 2023 Nov 2];581:012004. Available from: https://iopscience.iop.org/article/10.1088/1742-6596/581/1/012004

89. Chien CY, Xu L, Pacia CP, Yue Y, Chen H. Blood–brain barrier opening in a large animal model using closed-loop microbubble cavitation-based feedback control of focused ultrasound sonication. *Sci Reports 2022 121* [Internet]. 2022 [cited 2023 Nov 2];12:1–9. Available from: https://www.nature.com/articles/s41598-022-20568-y

90. O'Reilly MA, Hynynen K. Blood-Brain Barrier: Real-time Feedback-controlled Focused Ultrasound Disruption by Using an Acoustic Emissions–based Controller. *https://doi.org/101148/radiol11111417* [Internet]. 2012 [cited 2023 Nov 3];263:96–106. Available from: https://pubs.rsna.org/doi/10.1148/radiol.11111417

91. Abrahao A, Meng Y, Llinas M, Huang Y, Hamani C, Mainprize T, Aubert I, Heyn C, Black SE, Hynynen K, Lipsman N, Zinman L. First-in-human trial of blood–brain barrier opening in amyotrophic lateral sclerosis using MR-guided focused ultrasound. *Nat Commun 2019 101* [Internet]. 2019 [cited 2023 Nov 3];10:1–9. Available from: https://www.nature.com/articles/s41467-019-12426-9

92. Mehta RI, Carpenter JS, Mehta RI, Haut MW, Ranjan M, Najib U, Lockman P, Wang P, D'Haese PF, Rezai AR. Blood-brain barrier opening with MRI-guided focused ultrasound elicits meningeal venous permeability in humans with early Alzheimer disease. *Radiology* [Internet]. 2021 [cited 2023 Nov 3];298:654–662. Available from: https://pubs.rsna.org/doi/10.1148/radiol.2021200643

93. Fisher DG, Sharifi KA, Zeynep Ulutas E, Kumar JS, Kalani MYS, Wilson Miller G, Price RJ, Tvrdik P. Magnetic Resonance Imaging of Mouse Cerebral Cavernomas Reveal Differential Lesion Progression and Variable Permeability to Gadolinium. *Arterioscler Thromb Vasc Biol* [Internet]. 2023 [cited 2023 Nov 3];43:958–970. Available from: https://www.ahajournals.org/doi/abs/10.1161/ATVBAHA.122.318938

94. Moultrie F, Horne MA, Josephson CB, Hall JM, Counsell CE, Bhattacharya JJ, Papanastassiou V, Sellar RJ, Warlow CP, Murray GD, Al-Shahi Salman R. Outcome after surgical or conservative management of cerebral cavernous malformations. *Neurology* [Internet]. 2014 [cited 2023 Nov 2];83:582. Available from: /pmc/articles/PMC4141991/

95. Rauschenbach L, Santos AN, Dinger TF, Darkwah Oppong M, Li Y, Tippelt S, Dohna-Schwake C, Schmidt B, Jabbarli R, Wrede KH, Sure U, Dammann P. Functional outcome

after pediatric cerebral cavernous malformation surgery. *Sci Rep* [Internet]. 2023 [cited 2023 Nov 2];13. Available from: /pmc/articles/PMC9911771/

96. Heemskerk JWM, Kuijpers MJE, Globisch MA, Onyeogaziri C, Smith RO, Arce M, Magnusson PU. Dysregulated Hemostasis and Immunothrombosis in Cerebral Cavernous Malformations. 2022 [cited 2023 Jan 18];Available from: https://doi.org/10.3390/ijms232012575

97. Tung Y-S, Vlachos F, Feshitan JA, Borden MA, Konofagou EE. The mechanism of interaction between focused ultrasound and microbubbles in blood-brain barrier opening in mice. *J Acoust Soc Am* [Internet]. 2011 [cited 2023 Jan 18];130:3059. Available from: /pmc/articles/PMC3248062/

98. Choi JJ, Feshitan JA, Baseri B, Wang S, Tung YS, Borden MA, Konofagou EE. Microbubble-Size Dependence of Focused Ultrasound-Induced Blood–Brain Barrier Opening in Mice In Vivo. *IEEE Trans Biomed Eng* [Internet]. 2010 [cited 2023 Jan 18];57:145. Available from: /pmc/articles/PMC3968777/

99. Tsai CH, Zhang JW, Liao YY, Liu HL. Real-time monitoring of focused ultrasound blood-brain barrier opening via subharmonic acoustic emission detection: implementation of confocal dual-frequency piezoelectric transducers. *Phys Med Biol* [Internet]. 2016 [cited 2023 Nov 3];61:2926. Available from: https://iopscience.iop.org/article/10.1088/0031-9155/61/7/2926

100. Mathew AS, Gorick CM, Price RJ. Single-cell mapping of focused ultrasound-transfected brain. *Gene Ther*. 2021;

101. Rödel CJ, Otten C, Donat S, Lourenço M, Fischer D, Kuropka B, Paolini A, Freund C, Abdelilah-Seyfried S. Blood Flow Suppresses Vascular Anomalies in a Zebrafish Model of Cerebral Cavernous Malformations. *Circ Res* [Internet]. 2019 [cited 2023 Jan 18];125:e43–e54. Available from: https://www.ahajournals.org/doi/abs/10.1161/CIRCRESAHA.119.315076

102. Burke CW, Suk JS, Kim AJ, Hsiang YHJ, Klibanov AL, Hanes J, Price RJ. Markedly enhanced skeletal muscle transfection achieved by the ultrasound-targeted delivery of non-viral gene nanocarriers with microbubbles. *J Control Release* [Internet]. 2012 [cited 2023 Jan 18];162:414–421. Available from: https://pubmed.ncbi.nlm.nih.gov/22800583/

103. Amin-Hanjani S, Ogilvy CS, Ojemann RG, Crowell RM. Risks of surgical management for cavernous malformations of the nervous system. *Neurosurgery* [Internet]. 1998 [cited 2023 Nov 28];42:1220–1228. Available from: https://pubmed.ncbi.nlm.nih.gov/9632179/

104. Hong T, Xiao X, Ren J, Cui B, Zong Y, Zou J, Kou Z, Jiang N, Meng G, Zeng G, Shan Y, Wu H, Chen Z, Liang J, Xiao X, Tang J, Wei Y, Ye M, Sun L, Li G, Hu P, Hui R, Zhang H, Wang Y. Somatic MAP3K3 and PIK3CA mutations in sporadic cerebral and spinal cord cavernous malformations. *Brain* [Internet]. 2021 [cited 2023 Nov 30];144:2648–2658. Available from: https://dx.doi.org/10.1093/brain/awab117

105. Zhou Z, Tang AT, Wong WY, Bamezai S, Goddard LM, Shenkar R, Zhou S, Yang J, Wright AC, Foley M, Arthur JSC, Whitehead KJ, Awad IA, Li DY, Zheng X, Kahn ML. Cerebral cavernous malformations arise from endothelial gain of MEKK3–KLF2/4 signalling. *Nat 2016 5327597* [Internet]. 2016 [cited 2023 Nov 30];532:122–126. Available from: https://www.nature.com/articles/nature17178

106. Polster SP, Stadnik A, Akers AL, Cao Y, Christoforidis GA, Fam MD, Flemming KD, Girard R, Hobson N, Koenig JI, Koskimäki J, Lane K, Liao JK, Lee C, Lyne SB, McBee N, Morrison L, Piedad K, Shenkar R, Sorrentino M, Thompson RE, Whitehead KJ, Zeineddine HA, Hanley DF, Awad IA. Atorvastatin Treatment of Cavernous Angiomas with Symptomatic Hemorrhage Exploratory Proof of Concept (AT CASH EPOC) Trial. *Clin Neurosurg* [Internet]. 2019 [cited 2023 Nov 30];85:843–853. Available from: https://journals.lww.com/neurosurgery/fulltext/2019/12000/atorvastatin_treatment_of_cavernous_angiomas_with.14.aspx

107. Hong CC, Tang AT, Detter MR, Choi JP, Wang R, Yang X, Guerrero AA, Wittig CF, Hobson N, Girard R, Lightle R, Moore T, Shenkar R, Polster SP, Goddard LM, Ren AA, Leu NA, Sterling S, Yang J, Li L, Chen M, Mericko-Ishizuka P, Dow LE, Watanabe H, Schwaninger M, Min W, Marchuk DA, Zheng X, Awad IA, Kahn ML. Cerebral cavernous malformations are driven by ADAMTS5 proteolysis of versican. *J Exp Med* [Internet]. 2020 [cited 2023 Nov 30];217. Available from: https://doi.org/10.1084/jem.20200140

108. Tang AT, Choi JP, Kotzin JJ, Yang Y, Hong CC, Hobson N, Girard R, Zeineddine HA, Lightle R, Moore T, Cao Y, Shenkar R, Chen M, Mericko P, Yang J, Li L, Tanes C, Kobuley D, Võsa U, Whitehead KJ, Li DY, Franke L, Hart B, Schwaninger M, Henao-Mejia J, Morrison L, Kim H, Awad IA, Zheng X, Kahn ML. Endothelial TLR4 and the microbiome drive cerebral cavernous malformations. *Nat 2017 5457654* [Internet]. 2017 [cited 2023 Nov 30];545:305–310. Available from: https://www.nature.com/articles/nature22075

109. Li W, Shenkar R, Detter MR, Moore T, Benavides C, Lightle R, Girard R, Hobson N, Cao Y, Li Y, Griffin E, Gallione C, Zabramski JM, Ginsberg MH, Marchuk DA, Awad IA. Propranolol inhibits cavernous vascular malformations by β1 adrenergic receptor antagonism in animal models. *J Clin Invest* [Internet]. 2021 [cited 2023 Nov 30];131. Available from: https://doi.org/10.1172/

110. Shi C, Shenkar R, Zeineddine HA, Girard R, Fam MD, Austin C, Moore T, Lightle R, Zhang L, Wu M, Cao Y, Gunel M, Louvi A, Rorrer A, Gallione C, Marchuk DA, Awad IA. B-Cell Depletion Reduces the Maturation of Cerebral Cavernous Malformations in Murine Models. *J Neuroimmune Pharmacol* [Internet]. 2016 [cited 2023 Nov 30];11:369–377. Available from: https://link.springer.com/article/10.1007/s11481-016-9670-0

111. Gibson CC, Zhu W, Davis CT, Bowman-Kirigin JA, Chan AC, Ling J, Walker AE, Goitre L, Monache SD, Retta SF, Shiu YTE, Grossmann AH, Thomas KR, Donato AJ, Lesniewski LA, Whitehead KJ, Li DY. Strategy for identifying repurposed drugs for the treatment of cerebral cavernous malformation. *Circulation* [Internet]. 2015 [cited 2023 Nov 30];131:289–299. Available from: https://www.ahajournals.org/doi/abs/10.1161/CIRCULATIONAHA.114.010403

112. Shenkar R, Peiper A, Pardo H, Moore T, Lightle R, Girard R, Hobson N, Polster SP, Koskimäki J, Zhang D, Lyne SB, Cao Y, Chaudagar K, Saadat L, Gallione C, Pytel P, Liao JK, Marchuk D, Awad IA. Rho kinase inhibition blunts lesion development and hemorrhage in murine models of aggressive Pdcd10/Ccm3 disease. *Stroke* [Internet]. 2019 [cited 2023 Nov 30];50:738–744. Available from: https://www.ahajournals.org/doi/abs/10.1161/STROKEAHA.118.024058

113. McKerracher L, Shenkar R, Abbinanti M, Cao Y, Peiper A, Liao JK, Lightle R, Moore T, Hobson N, Gallione C, Ruschel J, Koskimäki J, Girard R, Rosen K, Marchuk DA, Awad

IA. A Brain-Targeted Orally Available ROCK2 Inhibitor Benefits Mild and Aggressive Cavernous Angioma Disease. *Transl Stroke Res* [Internet]. 2020 [cited 2023 Nov 30];11:365–376. Available from: https://link.springer.com/article/10.1007/s12975-019-00725-8

114. Shenkar R, Shi C, Austin C, Moore T, Lightle R, Cao Y, Zhang L, Wu M, Zeineddine HA, Girard R, Mcdonald DA, Rorrer A, Gallione C, Pytel P, Liao JK, Marchuk DA, Awad IA. RhoA kinase inhibition with fasudil versus simvastatin in murine models of cerebral cavernous malformations. *Stroke* [Internet]. 2017 [cited 2023 Nov 30];48:187–194. Available from: https://www.ahajournals.org/doi/abs/10.1161/strokeaha.116.015013

115. Lopez-Ramirez MA, Pham A, Girard R, Wyseure T, Hale P, Yamashita A, Koskimäki J, Polster S, Saadat L, Romero IA, Esmon CT, Lagarrigue F, Awad IA, Mosnier LO, Ginsberg MH. Cerebral cavernous malformations form an anticoagulant vascular domain in humans and mice. *Blood* [Internet]. 2019 [cited 2023 Nov 30];133:193–204. Available from: https://dx.doi.org/10.1182/blood-2018-06-856062

116. Shang X, Wang P, Liu Y, Zhang Z, Xue Y. Mechanism of low-frequency ultrasound in opening blood-tumor barrier by tight junction. *J Mol Neurosci* [Internet]. 2011 [cited 2023 Nov 30];43:364–369. Available from: https://link.springer.com/article/10.1007/s12031-010-9451-9

117. Sheikov N, McDannold N, Jolesz F, Zhang YZ, Tam K, Hynynen K. Brain arterioles show more active vesicular transport of blood-borne tracer molecules than capillaries and venules after focused ultrasound-evoked opening of the blood-brain barrier. *Ultrasound Med Biol*. 2006;32:1399–1409.

118. Fisher DG, Sharifi KA, Shah IM, Gorick CM, Breza VR, Debski AC, Hoch MR, Cruz T, Samuels JD, Lukens JR, Miller GW, Tvrdik P, Price RJ. Focused Ultrasound Blood-Brain Barrier Opening Arrests the Growth and Formation of Cerebral Cavernous Malformations. *in prep*.

119. Plummer NW, Gallione CJ, Srinivasan S, Zawistowski JS, Louis DN, Marchuk DA. Loss of p53 Sensitizes Mice with a Mutation in Ccm1 (KRIT1) to Development of Cerebral Vascular Malformations. *Am J Pathol* [Internet]. 2004 [cited 2022 Mar 16];165:1509–1518. Available from: http://ajp.amjpathol.org/article/S0002944010634098/fulltext

120. Marty B, Larrat B, Van Landeghem M, Robic C, Robert P, Port M, Le Bihan D, Pernot M, Tanter M, Lethimonnier F, Mériaux S. Dynamic study of blood-brain barrier closure after its disruption using ultrasound: A quantitative analysis. *J Cereb Blood Flow Metab* [Internet]. 2012 [cited 2023 Nov 30];32:1948–1958. Available from: https://journals.sagepub.com/doi/10.1038/jcbfm.2012.100

121. Murakami K, Endo T, Tominaga T. An analysis of flow dynamics in cerebral cavernous malformation and orbital cavernous angioma using indocyanine green videoangiography. *Acta Neurochir (Wien)* [Internet]. 2012 [cited 2023 Nov 30];154:1169–1175. Available from: https://link.springer.com/article/10.1007/s00701-012-1354-9

122. Gonzalez LF, Lekovic GP, Eschbacher J, Coons S, Porter RW, Spetzler RF. Are cavernous sinus hemangiomas and cavernous malformations different entities? *Neurosurg Focus* [Internet]. 2006 [cited 2023 Nov 30];21:1–5. Available from: https://thejns.org/focus/view/journals/neurosurg-focus/21/1/foc.2006.21.1.7.xml

123. Curley CT, Mead BP, Negron K, Kim N, Garrison WJ, Wilson Miller G, Kingsmore KM, Andrew Thim E, Song J, Munson JM, Klibanov AL, Suk JS, Hanes J, Price RJ. Augmentation of brain tumor interstitial flow via focused ultrasound promotes brain-penetrating nanoparticle dispersion and transfection. *Sci Adv* [Internet]. 2020 [cited 2023 Nov 30];6. Available from: https://www.science.org/doi/10.1126/sciadv.aay1344

124. Arvanitis CD, Askoxylakis V, Guo Y, Datta M, Kloepper J, Ferraro GB, Bernabeu MO, Fukumura D, McDannold N, Jain RK. Mechanisms of enhanced drug delivery in brain metastases with focused ultrasound-induced blood–tumor barrier disruption. *Proc Natl Acad Sci U S A* [Internet]. 2018 [cited 2023 Nov 30];115:E8717–E8726. Available from: https://www.pnas.org/doi/abs/10.1073/pnas.1807105115

125. McMahon D, O'Reilly MA, Hynynen K. Therapeutic Agent Delivery Across the Blood–Brain Barrier Using Focused Ultrasound. *https://doi.org/101146/annurev-bioeng-062117-121238* [Internet]. 2021 [cited 2023 Nov 30];23:89–113. Available from: https://www.annualreviews.org/doi/abs/10.1146/annurev-bioeng-062117-121238

126. Labriji W, Clauzel J, Mestas JL, Lafond M, Lafon C, Salabert AS, Hirschler L, Warnking JM, Barbier EL, Loubinoux I, Desmoulin F. Evidence of cerebral hypoperfusion consecutive to ultrasound-mediated blood-brain barrier opening in rats. *Magn Reson Med* [Internet]. 2023 [cited 2023 Nov 30];89:2281–2294. Available from: https://onlinelibrary.wiley.com/doi/full/10.1002/mrm.29596

127. Lee Y, Choi Y, Park EJ, Kwon S, Kim H, Lee JY, Lee DS. Improvement of glymphatic–lymphatic drainage of beta-amyloid by focused ultrasound in Alzheimer's disease model. *Sci Rep* [Internet]. 2020 [cited 2023 Nov 30];10:16144. Available from: /pmc/articles/PMC7527457/

128. Meng Y, Abrahao A, Heyn CC, Bethune AJ, Huang Y, Pople CB, Aubert I, Hamani C, Zinman L, Hynynen K, Black SE, Lipsman N. Glymphatics Visualization after Focused Ultrasound-Induced Blood–Brain Barrier Opening in Humans. *Ann Neurol* [Internet]. 2019 [cited 2020 Jul 5];86:975–980. Available from: https://onlinelibrary.wiley.com/doi/abs/10.1002/ana.25604

129. Han M, Seo H, Choi H, Lee EH, Park J. Localized Modification of Water Molecule Transport After Focused Ultrasound-Induced Blood–Brain Barrier Disruption in Rat Brain. *Front Neurosci* [Internet]. 2021 [cited 2023 Nov 30];15. Available from: /pmc/articles/PMC8358078/

130. Aryal M, Fischer K, Gentile C, Gitto S, Zhang YZ, McDannold N. Effects on P-Glycoprotein Expression after Blood-Brain Barrier Disruption Using Focused Ultrasound and Microbubbles. *PLoS One* [Internet]. 2017 [cited 2023 Nov 30];12:e0166061. Available from: https://journals.plos.org/plosone/article?id=10.1371/journal.pone.0166061

131. Cho HS, Lee HY, Han M, Choi JR, Ahn S, Lee T, Chang Y, Park J. Localized Down-regulation of P-glycoprotein by Focused Ultrasound and Microbubbles induced Blood-Brain Barrier Disruption in Rat Brain. *Sci Reports 2016 61* [Internet]. 2016 [cited 2023 Nov 30];6:1–10. Available from: https://www.nature.com/articles/srep31201

132. Kuroedov D, Cunha B, Pamplona J, Castillo M, Ramalho J. Cerebral cavernous malformations: Typical and atypical imaging characteristics. *J Neuroimaging* [Internet]. 2023 [cited 2023 Nov 26];33:202–217. Available from: https://onlinelibrary.wiley.com/doi/full/10.1111/jon.13072

133. Golden MJ, Morrison LA, Kim H, Hart BL. Increased Number of White Matter Lesions in Patients with Familial Cerebral Cavernous Malformations. *AJNR Am J Neuroradiol* [Internet]. 2015 [cited 2023 Nov 26];36:899. Available from: /pmc/articles/PMC4433814/

134. Ni H, Feng Z, Guan Y, Jia X, Chen W, Jiang T, Zhong Q, Yuan J, Ren M, Li X, Gong H, Luo Q, Li A. DeepMapi: a Fully Automatic Registration Method for Mesoscopic Optical Brain Images Using Convolutional Neural Networks. *Neuroinformatics* [Internet]. 2021 [cited 2023 Nov 26];19:267–284. Available from: https://link.springer.com/article/10.1007/s12021-020-09483-7

135. Ni H, Tan C, Feng Z, Chen S, Zhang Z, Li W, Guan Y, Gong H, Luo Q, Li A. A Robust Image Registration Interface for Large Volume Brain Atlas. *Sci Reports 2020 101* [Internet]. 2020 [cited 2023 Nov 26];10:1–16. Available from: https://www.nature.com/articles/s41598-020-59042-y

136. van Timmeren JE, Cester D, Tanadini-Lang S, Alkadhi H, Baessler B. Radiomics in medical imaging—"how-to" guide and critical reflection. *Insights Imaging* [Internet]. 2020 [cited 2023 Nov 26];11:1–16. Available from: https://insightsimaging.springeropen.com/articles/10.1186/s13244-020-00887-2

137. Mayerhoefer ME, Materka A, Langs G, Häggström I, Szczypiński P, Gibbs P, Cook G. Introduction to Radiomics. *J Nucl Med* [Internet]. 2020 [cited 2023 Nov 28];61:488–495. Available from: https://jnm.snmjournals.org/content/61/4/488

138. Denier C, Labauge P, Bergametti F, Marchelli F, Riant F, Arnoult M, Maciazek J, Vicaut E, Brunereau L, Tournier-Lasserve E. Genotype–phenotype correlations in cerebral cavernous malformations patients. *Ann Neurol* [Internet]. 2006 [cited 2023 Nov 28];60:550–556. Available from: https://onlinelibrary.wiley.com/doi/full/10.1002/ana.20947

139. Riant F, Bergametti F, Fournier HD, Chapon F, Michalak-Provost S, Cecillon M, Lejeune P, Hosseini H, Choe C, Orth M, Bernreuther C, Boulday G, Denier C, Labauge P, Tournier-Lasserve E. CCM3 Mutations Are Associated with Early-Onset Cerebral Hemorrhage and Multiple Meningiomas. *Mol Syndromol* [Internet]. 2013 [cited 2023 Nov 28];4:165–172. Available from: https://dx.doi.org/10.1159/000350042

140. Shenkar R, Shi C, Rebeiz T, Stockton RA, McDonald DA, Mikati AG, Zhang L, Austin C, Akers AL, Gallione CJ, Rorrer A, Gunel M, Min W, De Souza JM, Lee C, Marchuk DA, Awad IA. Exceptional aggressiveness of cerebral cavernous malformation disease associated with PDCD10 mutations. *Genet Med*. 2015;17:188–196.

141. Fauth C, Rostasy K, Rath M, Gizewski E, Lederer AG, Sure U, Zschocke J, Felbor U. Highly variable intrafamilial manifestations of a CCM3 mutation ranging from acute childhood cerebral haemorrhage to late-onset meningiomas. *Clin Neurol Neurosurg* [Internet]. 2015 [cited 2023 Nov 28];128:41–43. Available from: http://dx.doi.org/10.1016/j.clineuro.2014.10.023

142. Poorthuis M, Samarasekera N, Kontoh K, Stuart I, Cope B, Kitchen N, Al-Shahi Salman R. Comparative studies of the diagnosis and treatment of cerebral cavernous malformations in adults: systematic review. *Acta Neurochir (Wien)* [Internet]. 2013 [cited 2023 Nov 28];155:643–649. Available from: https://pubmed.ncbi.nlm.nih.gov/23371401/

143. Gross BA, Batjer HH, Awad IA, Bendok BR, Du R. Brainstem cavernous malformations: 1390 surgical cases from the literature. *World Neurosurg* [Internet]. 2013 [cited 2023 Nov

28];80:89–93. Available from: https://pubmed.ncbi.nlm.nih.gov/22484766/

144. Englander ZK, Wei HJ, Pouliopoulos AN, Bendau E, Upadhyayula P, Jan CI, Spinazzi EF, Yoh N, Tazhibi M, McQuillan NM, Wang TJC, Bruce JN, Canoll P, Feldstein NA, Zacharoulis S, Konofagou EE, Wu CC. Focused ultrasound mediated blood–brain barrier opening is safe and feasible in a murine pontine glioma model. *Sci Reports 2021 111* [Internet]. 2021 [cited 2023 Nov 28];11:1–10. Available from: https://www.nature.com/articles/s41598-021-85180-y

145. Ye D, Luan J, Pang H, Yang Y, Nazeri A, Rubin JB, Chen H. Characterization of focused ultrasound-mediated brainstem delivery of intranasally administered agents. *J Control Release* [Internet]. 2020 [cited 2023 Nov 28];328:276. Available from: /pmc/articles/PMC7749082/

146. Alli S, Figueiredo CA, Golbourn B, Sabha N, Wu MY, Bondoc A, Luck A, Coluccia D, Maslink C, Smith C, Wurdak H, Hynynen K, O'Reilly M, Rutka JT. Brainstem Blood Brain Barrier Disruption using Focused Ultrasound: A Demonstration of Feasibility and Enhanced Doxorubicin Delivery. *J Control Release* [Internet]. 2018 [cited 2023 Nov 28];281:29. Available from: /pmc/articles/PMC6026028/

147. Weber-Adrian D, Thévenot E, O'Reilly MA, Oakden W, Akens MK, Ellens N, Markham-Coultes K, Burgess A, Finkelstein J, Yee AJM, Whyne CM, Foust KD, Kaspar BK, Stanisz GJ, Chopra R, Hynynen K, Aubert I. Gene delivery to the spinal cord using MRI-guided focused ultrasound. *Gene Ther* [Internet]. 2015 [cited 2023 Nov 28];22:568. Available from: /pmc/articles/PMC4490035/

148. Kong X, Luo S, Wu JR, Wu S, De Cecco CN, Schoepf UJ, Spandorfer AJ, Wang CY, Tian Y, Chen HJ, Lu GM, Yang GF, Zhang LJ. 18F-DPA-714 PET Imaging for Detecting Neuroinflammation in Rats with Chronic Hepatic Encephalopathy. *Theranostics* [Internet]. 2016 [cited 2023 Nov 28];6:1220. Available from: /pmc/articles/PMC4893647/

149. Lavisse S, Guillermier M, Hérard A-S, Petit F, Delahaye M, Camp N Van, Haim L Ben, Lebon V, Remy P, Dollé F, Delzescaux T, Bonvento G, Hantraye P, Escartin C. Neurobiology of Disease Reactive Astrocytes Overexpress TSPO and Are Detected by TSPO Positron Emission Tomography Imaging. 2012 [cited 2023 Nov 28];Available from: http://www.brainvisa.info

150. Israel I, Ohsiek A, Al-Momani E, Albert-Weissenberger C, Stetter C, Mencl S, Buck AK, Kleinschnitz C, Samnick S, Sirén AL. Combined [18F]DPA-714 micro-positron emission tomography and autoradiography imaging of microglia activation after closed head injury in mice. *J Neuroinflammation* [Internet]. 2016 [cited 2023 Nov 28];13:1–13. Available from: https://jneuroinflammation.biomedcentral.com/articles/10.1186/s12974-016-0604-9

151. Wu C, Yue X, Lang L, Kiesewetter DO, Li F, Zhu Z, Niu G, Chen X. Longitudinal PET Imaging of Muscular Inflammation Using 18F-DPA-714 and 18F-Alfatide II and Differentiation with Tumors. *Theranostics* [Internet]. 2014 [cited 2023 Nov 28];4:546. Available from: /pmc/articles/PMC3966057/

152. McDannold NJ, Vykhodtseva NI, Hynynen K. Microbubble contrast agent with focused ultrasound to create brain lesions at low power levels: MR imaging and histologic study in rabbits. *Radiology* [Internet]. 2006 [cited 2023 Nov 28];241:95–106. Available from: https://pubmed.ncbi.nlm.nih.gov/16990673/

153. Samiotaki G, Konofagou EE. Dependence of the Reversibility of Focused-Ultrasound-Induced Blood–Brain Barrier Opening on Pressure and Pulse Length In Vivo. *IEEE Trans Ultrason Ferroelectr Freq Control* [Internet]. 2013 [cited 2023 Nov 28];60:2257. Available from: /pmc/articles/PMC3968797/

154. Lopez-Ramirez MA, Fonseca G, Zeineddine HA, Girard R, Moore T, Pham A, Cao Y, Shenkar R, de Kreuk BJ, Lagarrigue F, Lawler J, Glass CK, Awad IA, Ginsberg MH. Thrombospondin1 (TSP1) replacement prevents cerebral cavernous malformations. *J Exp Med* [Internet]. 2017 [cited 2022 Jan 20];214:3331–3346. Available from: https://pubmed.ncbi.nlm.nih.gov/28970240/

155. Wu B, Warnock G, Zaiss M, Lin C, Chen M, Zhou Z, Mu L, Nanz D, Tuura R, Delso G. An overview of CEST MRI for non-MR physicists. *EJNMMI Phys* [Internet]. 2016 [cited 2023 Nov 28];3. Available from: /pmc/articles/PMC4999387/

156. Han Z, Liu G. CEST MRI trackable nanoparticle drug delivery systems. *Biomed Mater* [Internet]. 2021 [cited 2023 Nov 28];16. Available from: https://pubmed.ncbi.nlm.nih.gov/33470986/

157. Huang J, Chen Z, Park SW, Lai JHC, Chan KWY. Molecular Imaging of Brain Tumors and Drug Delivery Using CEST MRI: Promises and Challenges. *Pharmaceutics* [Internet]. 2022 [cited 2023 Nov 28];14. Available from: https://pubmed.ncbi.nlm.nih.gov/35214183/

158. Lu X, Ma Y, Chang EY, He Q, Searleman A, von Drygalski A, Du J. Simultaneous Quantitative Susceptibility Mapping (QSM) and R2* for High Iron Concentration Quantification with Three-Dimensional Ultrashort Echo Time (UTE) Sequences – an Echo Dependence Study. *Magn Reson Med* [Internet]. 2018 [cited 2023 Nov 28];79:2315. Available from: /pmc/articles/PMC5811338/

159. Deh K, Zaman M, Vedvyas Y, Liu Z, Gillen KMC, O' Malley P, Bedretdinova D, Nguyen T, Lee R, Spincemaille P, Kim J, Wang Y, Jin MM. Validation of MRI quantitative susceptibility mapping of superparamagnetic iron oxide nanoparticles for hyperthermia applications in live subjects. *Sci Reports 2020 101* [Internet]. 2020 [cited 2023 Nov 28];10:1–11. Available from: https://www.nature.com/articles/s41598-020-58219-9